Heterogeneous Catalysis with supported Nanoparticles – Particle Size Effects and Metal-Support Interactions

Dissertation

zur Erlangung des Doktorgrades der Naturwissenschaften

-Dr. rer. nat. –

des Fachbereichs 2 (Biologie/Chemie)

der Universität Bremen

vorgelegt von:

Sarah Neumann

Geboren in Verden (Aller)

Bremen, 24.10.2019

Die hier vorliegende Arbeit wurde im Zeitraum von Februar 2016 bis Oktober 2019 unter Betreuung von Herrn Dr. Sebastian Kunz in der Arbeitsgruppe von Herrn Prof. Dr. Marcus Bäumer am Institut für Angewandte und Physikalische Chemie (IAPC) der Universität Bremen angefertigt.

1. Gutachter: PD Dr. Sebastian Kunz
2. Gutachter: Prof. Dr. Marcus Bäumer

Tag des Kolloquiums: 13.12.2019

Versicherung an Eides Statt

Ich, Sarah Neumann (Weserstraße 3, 28832 Achim, Mart.-Nr.: 2466427) versichere an Eides Statt durch meine Unterschrift, dass ich die vorliegende Arbeit selbständig und ohne fremde Hilfe angefertigt und alle Stellen, die ich wörtlich dem Sinne nach aus Veröffentlichungen entnommen habe, als solche kenntlich gemacht habe, mich aus keiner anderen als der angegebenen Literatur oder sonstiger Hilfsmittel bedient habe.

Ich versichere an Eides Statt, dass ich die vorgenannten Angaben nach bestem Wissen und Gewissen gemacht habe und dass die Angaben der Wahrheit entsprechen und ich nichts verschwiegen habe.

Die Strafbarkeit einer falschen eidesstattlichen Versicherung ist mir bekannt, namentlich die Strafandrohung gemäß § 156 StGB bis zu drei Jahren Freiheitsstrafe oder Gelbstrafe bei vorsätzlicher Begehung der Tat bzw. gemäß § 161 Abs. 1 StGB bis zu einem Jahr Freiheitsstrafe oder Geldstrafe bei fahrlässiger Begehung.

(Sarah Neumann)

Bremen, 24.10.2019

Danksagung

Prof. Dr. Marcus Bäumer möchte ich zuerst danken für die Bereitstellung des Themas und die Unterstützung bei der Anfertigung der Publikationen.

PD Dr. Sebastian Kunz danke ich für die hervorragende Betreuung, die Unterstützung bei der Anfertigung der Publikationen, die ständige wissenschaftliche Diskussionsbereitschaft und natürlich für die tolle Zusammenarbeit. Danke, dass ich so viel von dir lernen konnte.

Cornelia Rybarsch-Steinke danke für die unzähligen AAS Messungen und die Unterstützung in der ganzen Zeit. **Martin Novak** möchte ich für die Hilfe bei technischen Problemen und für den Aufbau der Katalyse-Anlage danken.

PD Dr. Volkmar Zielasek danke ich für die Einführung in die TEM Messungen und **Dr. Karsten Thiel** für die ständige Hilfsbereitschaft bei allen möglichen Problem und Fragen mit dem TEM.

Vielen Dank an **Dr. Holger Borchert**, **Dr. Joanna Kolny-Olesiak**, **Prof. Dr. Jürgen Parisi** und **Alexandra Erdt** von der Universität Oldenburg für die gute Zusammenarbeit und die vielen Diskussionen bei den Projekttreffen.

Dr. Imke Schrader und **Dr. Anastasia Lackmann** danke ich die tolle Zusammenarbeit und die schöne gemeinsame Zeit am IAPC. Aber vor allem für die Freundschaft, die daraus entstanden ist.

Weiterhin möchte ich der gesamten Arbeitsgruppe am IAPC danken, insbesondere **Jan Ilsemann**, **David Steinebrunner**, **Daniel Loof, Simona Keil** und **Johanna Schröder** für die nette Arbeitsatmosphäre und den fachlichen Austausch.

Natürlich möchte ich auch meinem Ehemann **Pedro** und meinen **Eltern** danken für die seelische Unterstützung während dieser Zeit und dafür, dass ihr immer für mich da wart.

List of Publications

This thesis is based on the following papers:

I. S. Neumann, J. Schröder, F. Bizzotto, M. Arenz, A. Dworzak, M. Oezaslan, M. Bäumer, S. Kunz "Halide-Induced Leaching of Pt Nanoparticles – Manipulation of Particle Size by Controlled Ostwald Ripening" *ChemNanoMat*, **2019**, 5, 462-471

II. S. Neumann, T. Gutmann, G. Buntkowsky, S. Paul, G. Thiele, H. Sievers, M. Bäumer, S. Kunz "Insights into the reaction mechanism and particle size effects of CO oxidation over supported Pt nanoparticle catalysts" *Journal of Catalysis*, **2019**, 377, 662-672

III. S. Neumann, H.H. Doebler, S. Keil, A. Erdt, H. Borchert, J. Kolny-Olesiak, J. Parisi, M. Bäumer, S. Kunz "Effects of Particle size on Strong Metal Support Interactions using colloidal „surfactant-free" Pt nanoparticles on Fe_3O_4" *submitted*

Additional papers related to the content of the present work:

IV. Schrader, J. Warneke, S. Neumann, S.Grotheer, A. Abildgaard Swane, J.J.K. Kirkensgaard, M. Arenz, S. Kunz "Surface Chemistry of "Unprotected" Nanoparticles: A Spectroscopic Investigation on Colloidal Particles" *The Journal of Physical Chemistry C*, **2015**, 119, 17655-17661

V. S. Neumann, S. Grotheer, J. Tielke, I. Schrader, J. Quinson, A. Zana, M. Oezaslan, M. Arenz, S. Kunz „Nanoparticles in a Box: A Concept to Isolate, Store and Re-Use Colloidal Surfactant-Free Precious Metal Nanoparticles" *Journal of Materials Chemistry A,* **2017**, 5, 6140-6145

VI. J. Quinson, M. Inaba, S. Neumann, A.A. Swane, J. Bucher, S.B. Simonsen, L.T. Kuhn, J.J.K. Kirkensgaard, K.M. Jensen, M. Oezaslan, S. Kunz, M. Arenz "Investigating Particle Size Effects in Catalysis by Applying a Size-Controlled and Surfactant-Free Synthesis of Colloidal Nanoparticles in Alkaline Ethylene Glycol: Case Study of the Oxygen Reduction Reaction on Pt" *ACS Catalysis*, **2018**, 8, 7, 6627-6635

VII. J. Quinson, S. Neumann, T. Wannmacher, L. Kacenauskaite, M. Inaba, J. Bucher, F. Bizzotto, S. Simonsen, L.T. Kuhn, D. Bujak, A. Zana, M. Arenz, S. Kunz "Colloids for Catalysts: A Concept for the Preparation of Superior Catalysts of Industrial Relevance" *Angewandte Chemie*, **2018**, 130, 12518-12521.

VIII. V. Klimavicius, S. Neumann, S. Kunz, T. Gutmann, G. Buntkowsky “Room Temperature CO Oxidation Catalysed by Supported Pt Nanoparticles Revealed by Solid-State NMR and DNP Spectroscopy” *Catalysis Science & Technology*, **2019**, 3743-3752

A complete list of publication is located in the attachment.

Statement regarding my contribution to the publications:

The here presented papers are based on the collaboration with researchers from different universities.

Publication I: I performed the experimental work in collaboration with Johanna Schröder and the data evaluation. Furthermore, I was responsible for writing the manuscript. The EXAFS measurements were planed and performed by Matthias Arenz and Mehtap Oezaslan.

Publication II: I was responsible for sample preparation, performance of the catalytic experiments, calculation of the kinetic data, and writing of the manuscript. The solid state NMR data were performed at the TU Darmstadt by Torsten Gutmann and the chemisorption data were measured by Micromeritics.

Publication III: I performed the catalyst preparation of the monometallic Pt catalysts, the catalytic and kinetic experiments, and I was responsible for writing of the manuscript. The performance and evaluation of the XPS measurements were performed by Simona Keil. The synthesis and characterization of the bimetallic NPs were performed at the University of Oldenburg by Alexandra Erdt.

A further more detailed declaration on the contribution to the multi-author publications (I-III) is located in the attachment.

Publication IV: My part in this publication was the sample preparation and the performance of the IR spectroscopy, the scientific discussion, and proof reading of the manuscript.

Publication V: I was responsible for the NP synthesis, the performance of the catalytic experiments, and TEM measurements. Furthermore, I was involved in the preparation of the manuscript.

Publication VI: The contribution to this publication is related to the scientific discussion and the proof reading of the manuscript.

Publication VII: My contribution to the publication was the synthesis and characterization with TEM of the colloidal NPs and performance of the catalytic investigations in the liquid phase. Furthermore, I contributed to the preparation of the manuscript.

Publication VIII: I was responsible for the preparation of the supported colloidal NPs, the characterization with DRIFT spectroscopy, and the proof reading of the manuscript.

Deutsche Zusammenfassung

Primäre Ziele für eine nachhaltigere Chemie sind die Einsparung von Energie und Ressourcen sowie die Vermeidung giftiger und umweltschädlicher Abfälle. Die Schlüsseltechnologie um dieses zu erreichen ist Katalyse. Für industrielle Anwendungen sind hauptsächlich heterogene Katalysatoren geeignet, da diese Art von Katalysator es ermöglicht kontinuierliche Prozesse zu realisieren. Hierfür eignen sich hauptsächlich geträgerte Edelmetall Nanopartikel, da diese aufgrund ihrer großen Oberfläche eine hohe katalytische Aktivität aufweisen. Es ist weiterhin erstrebenswert die Struktur des Katalysators zu optimieren um Struktur-Aktivitäts-Selektivitäts Zusammenhänge zu verstehen und damit Prozesse effizienter zu gestalten. Normalerweise werden geträgerte Nanopartikel Katalysatoren durch Imprägnierung hergestellt. Hierzu wird ein poröses Metalloxid mit einer Lösung aus einem Edelmetallsalz versetzt und das Lösungsmittel durch Verdunstung entfernt. Die Nanopartikel werden anschließend auf dem Trägermaterial durch Kalzinieren und Reduktion gebildet. Für systematische Studien zur Optimierung der Partikelgröße und Einflusses des Trägermaterials ist diese Herstellungsmethode nicht geeignet, da meistens Partikel mit einer großen Partikelgrößenverteilung gebildet werden und zusätzlich das Trägermaterial die Bildung der Nanopartikel stark beeinflusst. Deshalb werden für akademische Studien kolloidale Herstellungsmethoden bevorzugt, die zu stabilen Nanopartikel Dispersion mit enger Größenverteilung führen. Allerdings sind normalerweise Liganden oder Polymere notwendig um kolloidale Nanopartikel zu stabilisieren und um die Größe und Form der Partikel zu beeinflussen. Die organischen Moleküle müssen vor der Katalyse entfernt werden, da sonst aktive Zentren blockiert werden. In dieser Arbeit wurde eine Syntheseroute zur Bildung von Platin Nanopartikeln in basischem Ethylenglykol verwendet. Studien haben gezeigt, dass diese Partikel frei von organischen Molekülen sind und nur durch CO und OH^- stabilisiert werden. Diese „surfactant-freien“ Nanopartikel können in einem Folgeschritt auf verschiedene Trägermaterialien aufgebracht werden (z.B. Al_2O_3, Fe_3O_4, TiO_2).

Zuerst wurde die Stabilität dieser kolloidalen NPs untersucht und es konnte gezeigt werden, dass die Anwesenheit von Halogeniden zum Auflösen der Partikel führt, wobei vor allem in bromidhaltigen Pt Nanopartikel Dispersionen signifikante Mengen an Pt Ionen detektiert wurden. Oftmals führt die Bildung gelöster Ionen zu einer Vergrößerung der Partikelgröße durch Ostwald Reifung, welches auch hier gezeigt wurde. Um die Ostwald Reifung zu beschleunigen wurde die Reaktionszeit während der Nanopartikelbildung in basischem Ethylenglykol variiert und die Verwendung von bromidhaltigen Precursoren führte zu einem schnelleren Partikelwachstum verglichen zu chloridhaltigen Precursoren. Auf Basis dieser Erkenntnisse und dem Wissen über die Oberflächen Chemie der

Partikel, wurde ein Konzept entwickelt um die Partikelgröße der „surfactant-freier“ Nanopartikel in einem Größenbereich von 1 – 4 nm mit enger Partikelgrößenverteilung zu kontrollieren.

Die anschließend geträgerten Nanopartikel wurden dann als heterogene Modellkatalysatoren in der Oxidation von Kohlenmonoxid eingesetzt, da die Partikelgrößenabhängigkeit dieser Reaktion kontrovers diskutiert wird. Der Partikelgrößen Bereich zwischen 1 – 4 nm ist besonders relevant, da sich das Verhältnis von hochkoordinierten und niedrigkoordinierten Oberflächenatomen in diesem Größenbereich signifikant unterscheidet. Es wurde gezeigt, dass die Aktivität stark von der Partikelgröße abhängt und sich der Reaktionsmechanismus mit zunehmender Größe und Reaktionstemperatur ändert. Allgemein findet die Reaktion auf Pt Nanopartikeln auf inerten Träger (Al_2O_3) durch einen Langmuir-Hinshelwood Mechanismus statt, bei dem beide Reaktionspartner auf der Pt-Oberfläche adsorbiert sind. Allerdings adsorbiert O_2 bevorzugt dissoziativ auf Terrassenatomen und reagiert mit CO* zu CO_2*. Auch die Boudouard Reaktion zwischen zwei benachbarten CO* Molekülen zu C* und CO_2* wurde hauptsächlich auf Terrassenatomen nachgewiesen. Auf kleinen Partikeln, die hauptsächlich aus Ecken und Kanten bestehen, adsorbiert O_2 molekular und reagiert anschließend mit CO* zu CO_2* und O*.

Wenn diese Partikel auf reduzierbaren Trägern aufgebracht werden, läuft ein anderer Mechanismus ab, der aufgrund der Bildung von starken Metall-Substrat-Wechselwirkungen (*strong metal support interaction*, SMSI) bevorzugt wird. Der SMSI Effekt führt zur Bildung von aktiven Zentren an der Schnittstelle zwischen Träger und Partikel, an denen auf Pt adsorbiertes CO mit Gittersauerstoff vom Träger zu CO_2 reagiert (Mars van Krevelen Mechanismus). Mit zunehmender Partikelgröße nimmt die Pt Oberfläche stark zu, sodass auf großen Partikeln der Langmuir-Hinshelwood Mechanismus dominiert. Nachdem die Katalysatoren bei 200°C reduziert wurden, konnte der SMSI Effekt verstärkt werden, da ein FeO Film die Partikel teilweise bedeckte und somit die Aktivität verringert wurde. Ein ähnlicher Effekt auf der Nanoebene kann auch auf bimetallischen Fe-Pt NP beobachtet werden, der durch Oberflächen Segregation und in-situ Bildung von Eisenoxid hervorgerufen wird.

In dieser Arbeit wurde gezeigt, dass der Reaktionsmechanismus und die Aktivität von der katalytische Umsetzung von CO mit O_2 zu CO_2 sowohl durch die Partikelgröße als auch die Ausbildung von Metall-Substrat-Wechselwirkungen und die Verwendung von bimetallischen Partikeln stark beeinflussbar ist. Durch Änderung der Katalysatoreigenschaften ändern sich nicht nur die Aktivität, sondern auch die Reaktionsmechanismen. Insbesondere zeigen die Ergebnisse wie ein Katalysator hinsichtlich Partikelgröße und Träger beschaffen sein muss, um unter CO reichen Reaktionsbedingungen und Temperaturen um ca. 200°C maximale Aktivitäten zu erreichen.

Abstract

The improvement of environmental sustainability and awareness, the conversation of energy and resources, and the substantial reduction of large amount partially toxic waste in the chemical industry are the main topics for green chemistry. One issue is the use of catalysts in chemical reactions. For industrial scale productions especially heterogeneous catalysts are highly desired, since they allow the realisation of continuous processes. Often supported precious metal nanoparticles (NPs) are used as heterogeneous catalysts as they exhibit a high surface, which leads to high catalytic performance. The understanding of the structure-activity-selectivity relations of a supported metal NP catalyst allows improving catalytic processes. The common preparation strategy of supported NP catalysts is the impregnation of the support material with a solution of the precious metal salt followed by calcination and reduction. However, normally NPs with wide particle size distributions are obtained, which complicates systematic studies in catalytic application regarding the particle size and support effects. In this work a colloidal synthesis strategy to prepare Pt NPs is used, which enables the formation of NPs dispersion, without the need of strong binding surfactants. Normally, surfactants are used in colloidal NP synthesis to prevent the NPs from agglomeration. These organic molecules have to be removed before the catalysis, since they block active surface sites of the catalyst. The formation of Pt NPs was performed in alkaline ethylene glycol (EG) at 150°C and these NPs were found to be only stabilized by CO and OH^-. These "surfactant-free" NPs can be deposited in a subsequent step onto different support materials (e.g. Al_2O_3, Fe_3O_4, TiO_2).

First, the stability of the "surfactant-free" Pt NPs was investigated and it was found that the presence of chloride and bromide lead to particle dissolution, whereby especially the presence of bromide enhanced the formation of leached Pt species. A possible subsequent step of leaching is Ostwald ripening, which lead to particle growth and it was found that with increasing exposure time to halides the particle size indeed increased. In order to accelerate the Ostwald ripening the reaction of NPs in reducing atmosphere was enhanced and the particle size increased with increasing reaction time. The use of the bromide containing precursor showed a faster particle growth due to the enhanced dissolution of NPs in presence of bromide. A synthesis concept was developed based on Ostwald ripening and the knowledge about the surface chemistry of these NPs, which allowed controlling the particle size between 1 – 4 nm.

These heterogeneous catalysts were applied in CO oxidation, since the structure sensitivity of CO oxidation is controversially discussed. The particle size between 1 – 4 nm is in the range where the ratio of low to high coordinated surface atoms varies mostly and therefore these model catalysts are suitable to shed light into possible particle size effects in CO oxidation. Indeed, the kinetic investigation demonstrates that the activity depends on the particle size and the reaction mechanism

changes with increasing reaction temperature as well as with increasing particle size. CO oxidation with Pt NPs on Al_2O_3 proceeds via a Langmuir Hinshelwood mechanism with competitive adsorbed CO* and O_2*. However, it was found that on terrace atoms dissociative O_2 adsorption and reaction of CO* and O* to CO_2* and a Boudouard reaction (2 CO* → C* and CO_2*) are preferred, whereas molecular O_2 adsorption and reaction of CO* and O_2* to CO_2* and O* proceed on small particles, which high ratios of low coordinated edge and corner atoms.

Another reaction mechanism was found for Pt NPs supported on reducible Fe_3O_4, which was related due to the formation of strong metal support interactions (SMSI). The active sites on these catalysts were found to be the interface between the NP and the support and the reaction takes place with lattice oxygen from the iron oxide and adsorbed CO on Pt (Mars van Krevelen mechanism). However, with increasing particle size the contribution of the Mars van Krevelen mechanism decreased and a Langmuir Hinshelwood mechanism is favoured on the Pt surface. After reductive pre-treatment the SMSI effect is enhanced due to partial encapsulation of the NPs with a FeO layer, which decreased the active Pt surface. This effect is not only related to occur between NPs and support material, but it was found that a similar behaviour on the nanoscale was observed in bimetallic Fe-Pt NPs due to surface segregation and in-situ formation of iron oxide.

The here presented work demonstrates that the reaction mechanism and the catalytic performance of CO oxidation can be tune by changing the particle size, the support material and the use of bimetallic NPs. The change of the catalyst properties does not merely influence the activity, but also changes of the reaction mechanism are observed. In particular, these results demonstrate how the particle size and support of the catalyst should be obtained in order to achieve maximal activities under CO rich conditions and a reaction temperature of ~ 200°C.

Contents

List of Abbreviations

AAS	Atomic Absorption Spectroscopy
ATR-IR	Attenuated Total Reflection Infrared
DFT	Density Functional Theory
DRIFTS	Diffuse Reflectance Infrared Fourier Transform Spectroscopy
EDX	Energy Dispersive X-ray Spectroscopy
EG	Ethylene Glycol
EXAFS	Extended X-ray Absorption Fine Structure
HOMO	Highest Occupied Molecular Orbital
LUMO	Lowest Unoccupied Molecular Orbital
MARI	Most Abundant Reaction Intermediate
NMR	Nuclear Magnetic Resonance
NP	Nanoparticle
PVP	Polyvinylpyrrolidone
sccm	standard cubic centimeters per minute
SMSI	Strong Metal-Support Interactions
STEM	Scanning Transmission Electron Microscopy
TEM	Transmission Electron Microscopy
TOF	Turnover Frequency
TON	Turnover Number
UHV	Ultra-High Vacuum
XANES	X-ray Absorption Near-Edge Structure
XAS	X-ray Absorption Spectroscopy
XPS	X-ray Photoelectron Spectroscopy

1. Introduction

The key for a sustainable utilization of resources and energy in the chemical industry is the use of catalysts.[1-3] A catalyst lowers the activation barrier of a chemical reaction by opening alternative reaction pathways without changing the thermodynamics of the reaction (see Figure 1).[4-5] As a result, the reaction proceeds at lower reaction temperature, leading to reduced demands of energy.[6] A further advantage of catalytic reactions is the possibility to improve the selectivity of the reaction by optimizing the surface structure or the surface composition of the catalyst.[7-8] The importance of further investigations in catalysis research was appreciated with the Nobel price 2001 for William S. Knowles, Ryori Noyori and K. Barry Sharpless[9], 2005 for Yves Chauvin, Robert H. Grubbs and Richard R. Schrock[10], 2007 for Gerhard Ertl[11] and 2010 for Richard F. Heck, Ei-ichi Negishi and Akira Suzuki.[12] The improvement of catalytic activity and selectivity, stability under reaction conditions, recyclability of the catalyst, and the understanding of catalytic mechanisms is still a major challenge that can only be addressed by fundamental research.

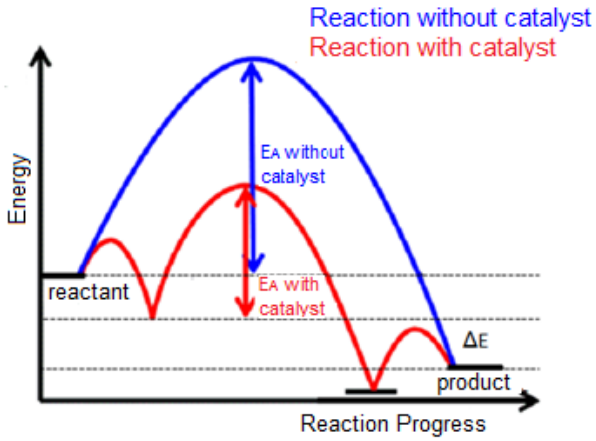

Figure 1: Energy diagram of an exothermic reaction with (red) and without (blue) catalyst. The catalyst allows another reaction pathway with lower activation energy (E_A).

Catalysts are classified in two main groups: Homogenous and heterogeneous catalysts. In homogenous catalysis the catalyst is dissolved in the liquid reaction medium and consists of a transition metal atom, which is coordinated by organic ligands.[13-14] These catalysts are characterized by high activities and selectivities.[15-16] Using chiral organic ligands even high enantioselectivities (>99%) can be obtained.[17-19] However, the mayor disadvantage of this kind of catalyst is the contamination of the product with partly toxic metals or ligand traces. The separation of the catalyst from the reaction media requires an addition step, which consumes energy and further resources and generates large amount of potentially toxic waste.[20] Recycling of the catalysts is therefore a great challenge and the realisation of continuous processes is challenging.

In heterogeneous catalysis the catalyst and the reactant exist in different physical states. The reactants are gases or liquids and the reaction proceeds at the surface of a solid catalyst (often precious metal surfaces).[21-22] In terms of process engineering, heterogeneous catalysts exhibit significant advantages mainly due to their application in continuous processes. The easy handling of the heterogeneous catalysts and the possible recyclability of the catalysts explains that up to 80% of all industrial processes use at least on heterogeneously catalysed step.[23]

The research in the field of nanotechnology leads to new materials, which find application in medicine, semiconductor technology, sensors, and especially in catalysis.[24-26] The size of such nanomaterial is in the range of 1 – 100 nm and the properties of these materials differ significantly from bulk material due to the change of the surface to volume ratio with decreasing size. The properties of nanomaterials are determined especially by surface atoms, which exhibit different electronic properties than bulk material, owing to the presence of low coordinated atoms.[26] Consequently, the size of the nanomaterial can strongly influence the properties of the material (e.g. binding energies of reactants, optical properties).[27-28]

Often precious metal nanoparticles (NPs) are used as heterogeneous catalysts, which require that the NPs are dispersed on support materials such as porous metal oxides with high specific surface areas (Al_2O_3, SiO_2, MgO etc.) or on carbon materials.[29-32] The use of supported NP catalysts has two main advantages: On the one hand a NP has a high number of catalytically active surface atoms in comparison to the bulk material and on the other hand the dispersion of the NPs on the support material reduces the amount of expensive precious metal, which are often used as catalysts. The catalytic performance of the NPs is determined by geometric and electronic properties of the surface atoms and the particle size and surface coordination is known to influence the catalytic performance.[33] A prominent example for the practical use of supported NPs on porous support materials as catalysts is the automotive catalyst. An automotive converter consists of a honeycomb structure with walls, which are covered with porous alumina. The alumina is impregnated with NPs of precious metals (Pt, Pd, Rh) and other metals (Ce). Pt and/or Pd catalyse the oxidation of hydrocarbons and carbon monoxide and Rh serves as reduction catalyst of NO_x. Ce_2O_3 is used as oxygen storage.[34]

In this work a synthesis rout for so-called “surfactant-free” Pt NP is introduced, which allows to tune the particle size in a range of 1 – 4 nm, which represents the particle size regime where the ratio of low and high coordinated surface atoms varies mostly. The presence of halides from the metal precursor during the preparation procedure was used to induce Ostwald ripening to increase the NP size. In the next step these NPs (1 – 4 nm particle size) were supported onto inert Al_2O_3 to prepare

model catalysts, which were used in CO oxidation. Structure sensitivity and particle size effects are controversially discussed in literature for CO oxidation. In this work changes in activity and reaction mechanism are presented that depend strongly on the particle size. A further possibility to influence the catalytic performance is the use of different support materials. The here presented preparation strategy allows the separation of NP formation and supporting. Hence, differences in activity and kinetic performance can be related directly to metal support interactions and particle size effects. In this work, the NPs were supported onto Fe_3O_4, which is a reducible support material and strong metal support interactions (SMSI) were found to occur between Pt and the iron oxide.

2. Nanoparticles

NPs can be prepared by two different approaches: “top-down” and “bottom-up”.[35] The concept of “top-down” is based on the crushing of bulk material by mechanical, chemical, or electrochemical methods. This synthesis strategy leads to large particles with a wide particle size distribution (see Figure 2a).[36] However, this approach is not suitable for systematic studies in catalytic research, since the wide particle size distribution of the NPs makes it difficult to obtain reproducible results in reactions which depend on the particle size and/or shape. Therefore, NPs for catalytic investigations are usually prepared by the “bottom-up” approach. NPs are synthesized in wet-chemical processes such as precipitation reactions, hydrothermal synthesis or sol-gel processes by reduction of metal precursors (see Figure 2b).[37-39] In this work the focus is on colloidal NPs. The advantage of this synthesis strategy is the ability to receive NPs with narrow size distribution and the control over particle size.[33]

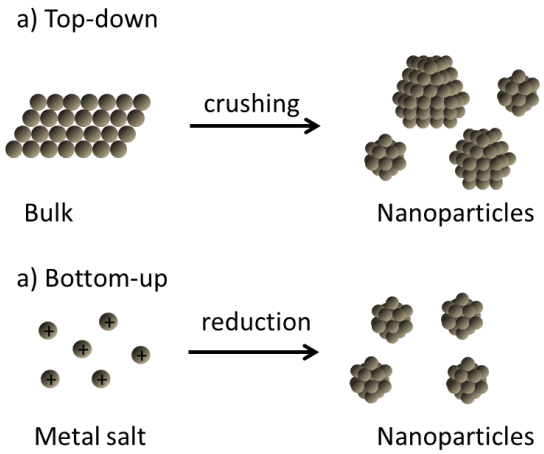

Figure 2: Synthesis principle of nanoparticles. (a) Shows the “top-down” approach by crushing bulk material to obtain nanoparticles and (b) represents the “bottom-up” approach by reduction of solved metal precursor salts.

2.1 Nucleation principles and growth of colloidal metal nanoparticles

The preparation of metal NPs with colloidal preparation methods is based on the use of metal salts, which are reduced with reducing agents (e.g. sodium borohydride, ascorbic acid or alcohols).[40-42] The reduction of the salt to metal atoms leads to the formation of metal clusters in the solution. This process is called nucleation. A distinction is made between homogeneous and heterogeneous nucleation. In homogeneous nucleation the formation of nuclei proceeds due to supersaturation and is therefore spontaneous. The free energy of a spherical cluster with the radius r, the surface energy γ, and the free energy of the bulk material ΔG_V is given by following rate equation (1):[43]

$$\Delta G = -\frac{4}{3}\pi r^3 \Delta G_V + 4r^2\pi\gamma \quad (1)$$

The first negative term implies that the formation of clusters is energetically favoured over a supersaturated solution and the positive term of equation (1) demonstrates the energetically unfavored formation of clusters due to the increase of the surface energy. As a result, the negative and the positive term of the free energy lead to a maximum energy at a certain cluster radius (critical radius r_c) (see Figure 3). For clusters with a radius $r < r_c$ dissolution is energetically favoured and for larger clusters with $r > r_c$ particle growth is preferred.[44]

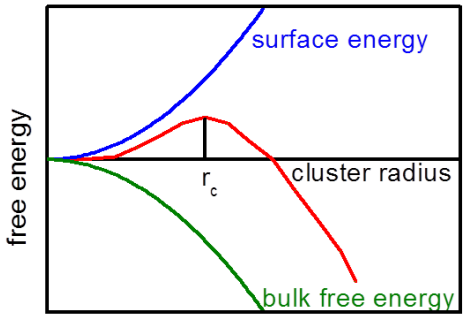

Figure 3: Nucleation theory. Dependence of the free energy of a cluster on the cluster radius r.

Depending on equation (1) the critical radius r_c is defined as following (2):

$$r_c = \frac{2\gamma}{\Delta G_V} \quad (2)$$

The integration of the critical radius in equation (1) yields the expression for the free energy ΔG_c at the maximum (3):

$$\Delta G_C = \frac{16\pi\gamma^3}{\Delta G_v{}^2} \quad (3)$$

The energy barrier of the particle growth is the activation energy. Hence, the Arrhenius equation can be used to express the nucleation rate J (4).

$$J(T, \Delta G_c) = Ae^{-\frac{\Delta G_C}{kT}} \quad (4)$$

In heterogeneous nucleation the nucleation occurs at preferential sites of the cluster surface. Such preferential sites can be for example phase boundaries or impurities, where the surface energy is lowered making nucleation energetically favoured at such sites. In the field of colloidal NP synthesis homogeneous as well as heterogeneous nucleation occurs in parallel.[43]

2.1.1 LaMer model

A model for nucleation and growth mechanisms was introduced 1950 from LaMer for the research on sulfur hydrosols.[45] The concept was transferred to the formation of colloidal NPs due to reduction of metal precursor salts and consists of three phases.[43, 46] In the first phase the metal salt is reduced and the formation of metal atoms (monomers) increases with reaction time. At a certain time, the concentration of the monomers reaches a critical supersaturation level (C_s), where nucleation theoretically can proceed. In the second phase the concentration of the monomer further increases and reaches the critical concentration and the activation barrier for self-nucleation can be overcome. In the third phase the concentration of the monomers decreases due to the nucleation below the critical concentration leading to the end of the nucleation phase (see Figure 4). The growth of the nuclei proceeds by diffusions of monomers to the particle surface.[43-44]

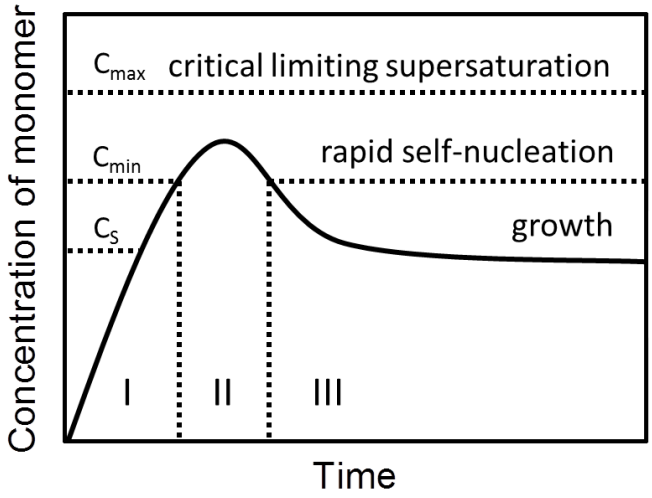

Figure 4: LaMer model. Principle of NP nucleation and particle growth

However, the LaMer model describes only the thermodynamic process of NP formation in colloidal preparation strategies, but the model is not able to predict particle size distributions or specifies the process of NP growth.[43]

2.1.2 Growth processes of colloidal nanoparticles

The growth of NPs proceeds after nucleation and is determined by i) the diffusion of the monomers to the NP surface and by ii) the surface reaction. The diffusion of the monomer to the particle surface can be described by Fick´s first law (5):[44]

$$J = 4\pi x^2 D \frac{dc}{dx} \tag{5}$$

With J defined as the total flux of the monomers, D as diffusion coefficient, c as the concentration of the monomer and x is the distance to the centre of the NP (see Figure 5).

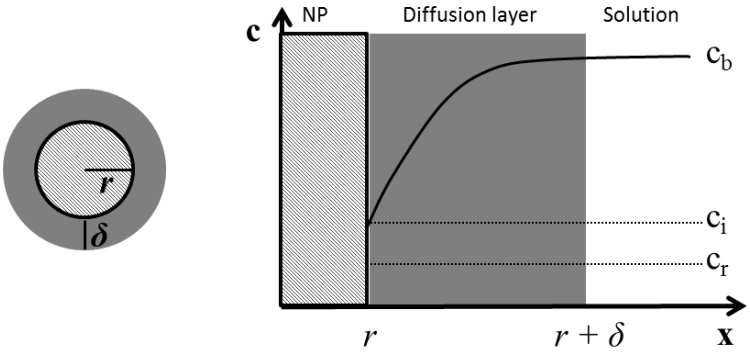

Figure 5: Schematic illustration of the diffusion model.

For a spherical particle equation (5) can be rewritten as (6):

$$J = \frac{4\pi Dr(r+\delta)}{\delta}(c_b - c_i) \tag{6}$$

δ represents the distance from the NP surface to the monomers in the solution, c_b is the concentration of the monomers in the solution, and c_i is the concentration of the monomer at the interface between the NP and the solution (see Figure 5). However, for NPs the particle radius is smaller than the diffusion layer ($r \ll \delta$). Hence, the diffusion of the monomers to the particle can be expressed by following equation (7):[44]

$$J = 4\pi Dr(c_b - c_i) \tag{7}$$

After the diffusion process, the surface reaction of the monomer at the NP surface proceeds and following equation is obtained, which describes the surface reaction (8):

$$J = 4\pi r^2 k(c_i - c_r) \tag{8}$$

With c_r as the particle density and k is the rate constant for particle growth.

There are two limiting factors, which can influence the particle growth: On the one hand the particle growth can be determined by the diffusion rate and following rate equation is obtained (9):

$$\frac{dr}{dt} = \frac{Dv}{r}(c_b - c_r) \tag{9}$$

Hence, the surface reaction proceeds fast and the rate of the particle growth depends only on the diffusion rate of the monomers to the particle surface.

On the other hand the surface reaction can be the limiting factor and rate equation (10) is obtained:

$$\frac{dr}{dt} = k_v(c_b - c_r) \tag{10}$$

Monomers are present at the particle surface due to the high diffusion rate and therefore the particle growth rate depends only on the rate of the surface reaction.

The here discussed particle growth mechanisms are not able to explain, why the colloid preparation method leads to dispersions with uniform particles. In the case for particle growth by diffusion a model was developed by Reiss[47], which assumes that diffusional growth depends only on the monomer flux and predicts that in the presence of larger particles the smaller particles grow faster due to their higher surface energy. This leads to a narrowing of the size distribution. However, the model of Reiss neglects other more complex growth mechanism such as Ostwald ripening or particle aggregation.[43]

The inclusion of the Gibbs Thomson relation (11) takes into account that the stability against dissolution of the NP depends on the particle size.[44]

$$C_r = C_b e^{\frac{2\gamma v}{r k_B T}} \tag{11}$$

When the concentration of the monomers in the solution is almost consumed, further particle growth via Ostwald ripening is possible.[48] The Gibbs Thomson relation (equation 11) predicts that small particles exhibit a higher surface energy and hence the small particles dissolve and the monomers attach at larger particles with lower surface energy. As a result, the larger particles grow at the expense of small particles. Other growth mechanisms are for example coalescence of individual particles[49] or intraparticle growth.[50]

2.2 Stability of colloidal nanoparticles

The stability of colloidal NPs in dispersion is one of the most important aspects in the research field of nanomaterials. Due to the presence of attractive forces (van der Waals, electrostatic and magnetic forces) NPs in colloidal dispersion are not stable and tend to agglomerate. A theory was developed by Derjaguin, Landau, Verwey and Overbeek, known as DLVO theory, which is still accepted to describe the physics of colloidal stability.[51-52] The theory is based on two combined forces, which occur in colloidal dispersions: (i) attractive van der Waals interactions and (ii) repulsive electrostatic

interactions. To describe the interaction energy of the pair potential $W(r)$ of two molecules at a distance r, the Lennard-Jones potential is used (12).[43]

$$W(D) = -\frac{C}{r^6} + \frac{B}{r^{12}} \tag{12}$$

The constant C represents the attractive van der Waals forces and the constant B is the repulsive Born repulsion. In the following the attractive van der Waals interactions and the repulsive electrostatic interactions are discussed.

2.2.1 Van der Waals interactions

The attractive van der Waals interaction energy $W_a(D)$ between two particle with the distance D is the sum of all intermolecular forces. For simplification the assumption was made that the particles have the same size and that the particles are in close proximity, which leads to following equation (13). With ρ as electron density and A as the Hamaker constant:[43]

$$W_a(D) = -\frac{\pi^2 \rho_1 \rho_2 C d}{12D} = -\frac{AR}{12D} \tag{13}$$

Equation (13) indicates that the van der Waals force is proportional to the particle size R and reciprocal proportional to the distance D of two NPs.

2.2.2 Electrostatic interactions

The preparation of a stable colloidal NP dispersion requires the presence of repulsive interaction to overcome the attractive van der Waals interaction, which would lead to agglomeration. In liquid media, ions surround the particles forming an electric double layer, which protects the NPs from aggregation. The thickness of the electric double layer is named Debye length λ (κ^{-1}) and can be described using simple electrostatics. The surface potential ψ of the electric double layer can be explained with following equation (14):[43]

$$\psi(x) = \psi_0(x) e^{-\kappa x} \tag{14}$$

In order to consider the colloidal stability in NP dispersion, the interaction of at least two spherical particles with the radius R and the surface to surface distance D have to be taken into account. The Derjaguin approximation enables the determination of the potential repulsion force of two spherical particles (15).

$$W_R(D) = 2\pi\varepsilon\varepsilon_0 R \psi_\delta^2 e^{-\kappa D} \tag{15}$$

ε_o is the permittivity of vacuum and ε the dielectric constant.

The DLVO theory combines the above describes forces in a colloidal NP dispersion by addition of the attractive and the repulsive forces (16).

$$W_{total}(D) = -\frac{AR}{12D} + 2\pi\varepsilon\varepsilon_0 R\psi_\delta^2 e^{-\kappa D} \quad (16)$$

Equation (16) shows that the stability of a colloidal dispersion depends on i) the concentration of the ion and the ion type (ε, κ), ii) the surface potential ψ, and iii) the particle radius R. Decreasing the distance between the particles leads to an increase of the attractive van der Waals interactions and hence agglomeration of the particles proceeds.[43]

Besides the above discussed electronic stabilization by the formation of an electronic double layer on the metal surface[37, 43], steric stabilization is another concept to improve the stability of the colloidal NP dispersions. The binding of organic molecules (ligands or polymers) at the particle surface leads to a protection layer around the particles, which prevents the aggregation of single particle by steric shielding.[53-55] The combination of electronic and steric combination can be achieved with ionic surfactants, which consists of a polar head group that forms an electrical double layer and a lipophilic chain for steric repulsion.[56-57] A further possibility to stabilise colloidal NPs is the encapsulation of the NPs within dendrimers or micelles.[58-59]

3. Heterogeneous catalysis

The properties that characterize a catalyst are:[3]

i) Activity
ii) Selectivity
iii) Stability

The **activity** of a catalytic reaction is related to the amount of converted reactant with time to the mass of the catalyst. However, in heterogeneous catalysis only surface atoms can be catalytically active and hence the reaction rate should be referred to the number of surface atoms. The reaction rates in heterogeneous catalysis are defined therefore as turnover frequencies (TOF) (17):[60-61]

$$TOF = \frac{dc_{product}}{c_{catalyst}dt} \tag{17}$$

In case of heterogeneous catalysts based on NPs the number of surface atoms is estimated from the particle size, which can be determined from transmission electron microscopy (TEM) measurements. Another possibility are chemisorption measurements, where the catalyst is exposed to strong binding molecules (CO or H_2), which chemisorb on the catalyst surface.[62] Hence, the number of active surface sites can be determined under reaction conditions. The dispersion (ratio of surface atoms) can be estimated by following equation (18).

$$D = \frac{n_{surface\ atoms}}{n_{total\ number\ of\ atoms}} \tag{18}$$

The **selectivity** S of a catalytic reaction is given as the ratio of the reaction rate of the product and the reaction rate of reactant conversion (19):[3]

$$S = \frac{n_{product}}{n_{converted\ reactant}} \tag{19}$$

In order to describe the **stability** of a catalyst the dimensionless turnover number (TON) was defined as the amount of product formed under defined reaction conditions related to the number of active sites of catalyst (20):

$$TON = \frac{n_{Product}}{n_{catalyst}} \tag{20}$$

Often a decreasing activity over time is observed, which could be related to agglomeration of NPs, carbon accumulation on the catalyst surface or poisoning by impurities in the gas stream (e.g. sulfur).[63-65]

3.1 Reaction mechanisms in heterogeneous catalysis

In heterogeneous catalysis the reaction proceeds at the catalyst surface, which requires the transfer of reactants to the active reaction sites. In order to describe the relevant microscopic steps of a catalytic reaction on a porous catalyst, the following reaction steps have to be taken into account (see Figure 6):[3]

i) Diffusion of the reactants to catalyst
ii) Diffusion of the reactants into the pores (pore diffusion)
iii) Adsorption of the reactants at the active sites
iv) Reaction at the active site
v) Desorption of the product from the active site
vi) Diffusion of the products out of the pores
vii) Diffusion of the products from the catalyst into the gas phase or solvent

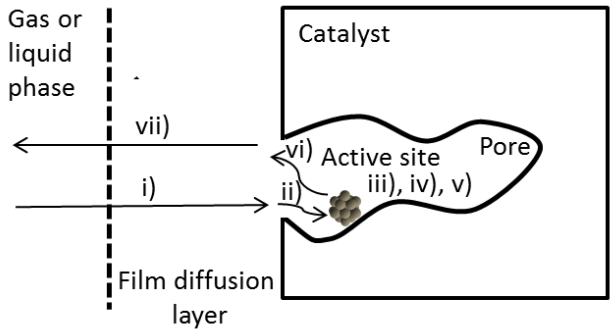

Figure 6: Steps of a heterogeneously catalysed gas phase or liquid phase reaction with a porous catalyst.

Considering mass transfer and the chemical reaction at the surface (steps i-vii) to influence the catalytic performance, the term macrokinetics is used.[3, 66] However, in this work the focus is on the determination of the kinetic of the chemical reaction at the surface of the catalyst (steps iii-v), which means that in microkinetic studies mass transfer limitation has to be excluded and the reaction rate depends only on intrinsic catalytic activity of the active sites.[67] Microkinetic analysis offers the opportunity to determine kinetic parameters (e.g. effective rate constants, reaction orders, and apparent activation energies) of the catalytic reaction and reaction mechanisms can be postulated.[3, 68] The knowledge about the reaction mechanism and the sequence of elementary steps of the

catalysed reaction allows improving the catalyst (e.g. particle size, composition, surface structure) for optimisation of the catalytic performance.

For microkinetic analysis the adsorption of the reactants on the catalyst surface is of fundamental importance and on homogenous solid catalyst surface the adsorption of A can be expressed with the Langmuir isotherm (21):[69]

$$\theta_A = \frac{K_A[A]}{1 + K_A[A]} \tag{21}$$

Θ_A represents the coverage of the surface, $[A]$ is the concentration of the A and K_A is the equilibrium constant. In this work a bimolecular gas phase reaction is discussed to proceed on precious metal NPs (A + B → C). In general, there are two reaction mechanisms, which may describe the catalytic reaction of two reactants on the surface of a heterogeneous catalyst (Langmuir Hinshelwood mechanism and Eley Rideal mechanism). The differences of these mechanisms are discussed in the following and a further special reaction mechanism is introduced (Mars van Krevelen mechanism).

3.1.1 Langmuir Hinshelwood mechanism

The Langmuir Hinshelwood mechanism describes the adsorption of both reactants on separate free adsorption sites and the reaction occurs on the catalyst surface. Afterwards, the product desorbs from the surface (see Figure 7).[3, 69]

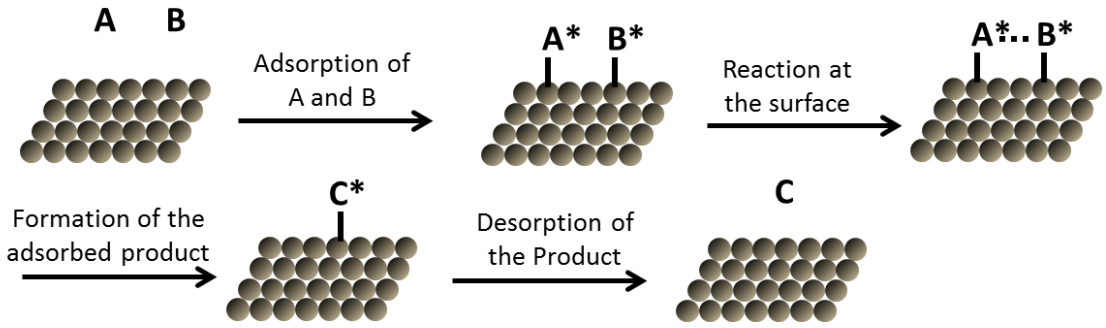

Figure 7: Reaction scheme of a Langmuir Hinshelwood of two adsorbed reactants A and B to the product C.

Assuming the surface reaction as the rate determing step, the following rate equation can be obtained for the Langmuir Hinshelwood mechanism (22):[3]

$$r = \frac{kK_A[A]K_B[B]}{(1 + K_A[A] + K_B[B])^2} \tag{22}$$

The assumption that both reactants are weakly adsorbed on the surface (K_A and $K_B << 1$) equation (22) simplifies to (23):

$$r = kK_A K_B [A][B] \tag{23}$$

And reaction orders of 1 for both reactants are expected. In contrast, weak adsorption of A ($K_A << 1$) and the strong adsorption of B ($K_B >> 1$) lead to the following rate equation (24):

$$r = \frac{kK_A[A]}{K_B[B]} \tag{24}$$

And reaction orders of 1 for A and -1 for B are expected.

3.1.2 Eley-Rideal mechanism

The Eley-Rideal mechanism describes the reaction of one reactant being adsorbed on the catalysts surface with a reactant from the gas or liquid phase. The reaction leads to an adsorbed product, which desorbs in the final step (see Figure 8).[3, 69]

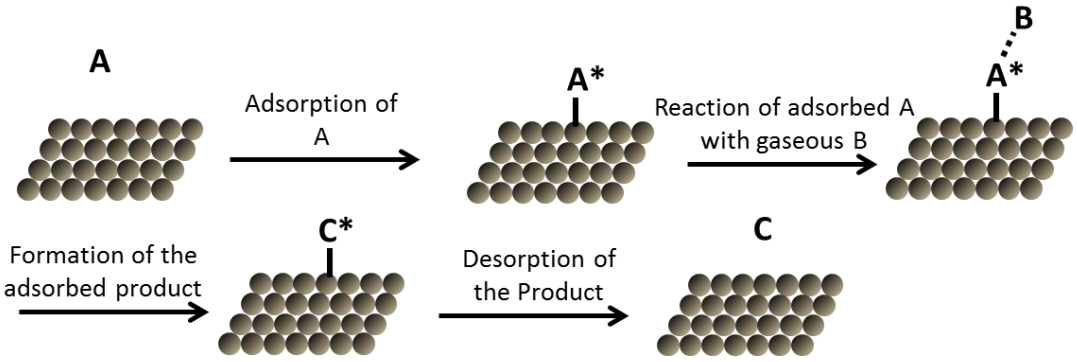

Figure 8: Reaction scheme of an Eley Rideal mechanism with adsorbed A and gaseous B to the product C.

The following rate expression is obtained for an Eley-Rideal mechanism (25):[3]

$$r = k\frac{K_A[A]}{(1 + K_A[A])}[B] \tag{25}$$

With a constant concentration of B, the rate follows the Langmuir isotherm of A. The kinetic properties of a heterogeneously catalysed reaction differ strongly whether the reaction proceeds via a Langmuir-Hinshelwood mechanism or an Eley-Rideal mechanism.

3.1.3 Mars van Krevelen mechanism

A third reaction mechanism observed for supported catalysts on reducible metal oxides is the Mars van Krevelen mechanism. One reactant A adsorbs on the metal surface and in the next step the reactant is oxidized with lattice oxygen from the support material. The formed product desorbs from the metal surface and the reduced support material is regenerated by gaseous oxygen (see Figure 9).[70]

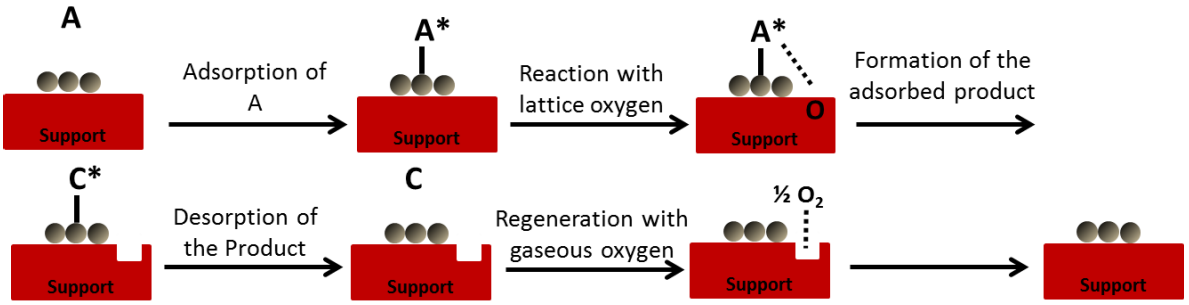

Figure 9: Reaction scheme of a Mars van Krevelen mechanism with adsorbed A and lattice oxygen.

4. Supported nanoparticles as heterogeneous catalysts

As discussed above, catalytic reactions on heterogeneous metal surfaces proceed after the adsorption of at least one reactant at the catalyst surface.[3] The interaction of gas molecules with transition metal surfaces was described by Hammer and Nørskov using the d-band model.[71] The ability of a bond formation of a metal atom with the adsorbate is determined by the position of the d-band center with respect to the Fermi energy. A shift to higher levels leads to the formation of a higher concentration of empty anti-bonding states and hence the binding energy of the adsorbate is enhanced. On transition metal surfaces it is known that low coordinates surface sites (edge and kinks) exhibit higher d-band centres.[72-73] As a consequence, gaseous adsorbates bind stronger at low coordinated surface sites compared to atoms in a close packed surface structure. On small NPs (≤ 5 nm) the ratio of low coordinated surface atoms (edge and corner atoms) and high coordinated terrace atoms depend strongly on the particle size.[74-75] Assuming a cubo-octahedral shape of the particles, which was predicted as the energetic minimum for NPs[76-77], the ratio of low coordinated sites is significantly higher on small NPs, whereas the ratio of terrace atoms increases strongly with increasing particles size (see Figure 10).[78]

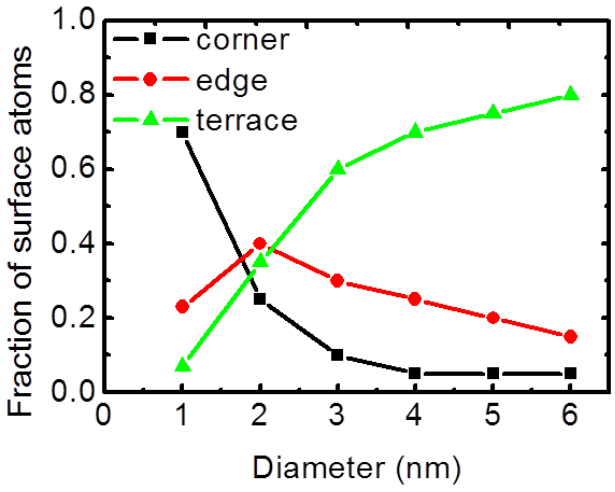

Figure 10: The percentage ratio of low coordinated surface atoms (edge and corner atoms) and high coordinated terrace atoms assuming a cubo-octahedral shape of the NPs. [78]

Hence, the catalytic performance of supported NPs catalysts is expected to depend on the particle morphology (particle size and shape) due to changing binding energies at different surface sites. Furthermore, the distribution of the NPs on the support and the interactions of the NPs with the support material are known to influence the properties of the catalyst.[79] Therefore, the preparation method of the supported NPs catalysts may influence the catalytic performance. In the following, different preparation strategies are introduced.

4.1 Preparation of supported nanoparticles

4.1.1 Conventional preparation methods

The common preparation of supported NPs is the incipient wetness impregnation or the wet impregnation method (see Figure 11).[80-82] In incipient wetness impregnation the metal precursor is dissolved in an aqueous or organic solution and the pore volume of the support material is determined. An equal volume of the precursor solution compared to the pore volume is added to the support material and the capillary forces cause the solution to diffuse into the pores. Afterwards, the catalyst is dried to remove the solvent. The formation of NPs occurs due to calcination and/or reduction of the catalyst (see Figure 11). The principle of wet impregnation is similar with the difference that a higher volume of precursor solution than the pore volume is added.

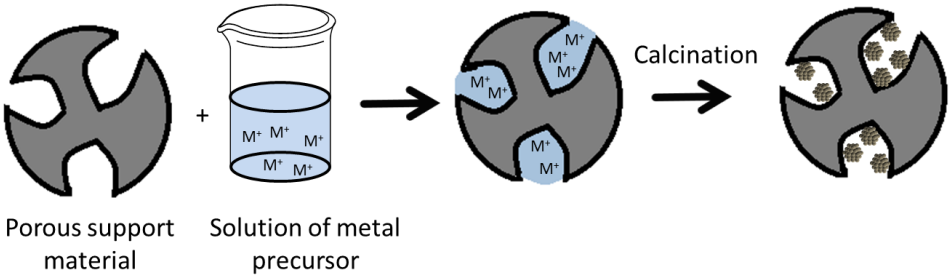

Figure 11: Conventional preparation method of support NP catalysts (here incipient wetness impregnation). A metal precursor is added to the porous support material and NPs are formed during calcination and evaporation of the solvent.

Despite the simplicity of conventional preparation methods, the synthesis strategy bears disadvantages for systematic research or the design of model catalysts. The support material influences the formation of the NPs. Thus, particle size, shape, and composition (in case of bimetallic NPs) cannot be controlled independently from the support material, which complicates systematic studies of catalytic properties induced by e.g. particle size or support effects.[33, 83] A further disadvantage is a maximal metal loading of the catalyst, which is related to the limited solubility of the metal precursor.

4.1.2 Colloidal preparation methods

To overcome the disadvantages of conventional preparation methods for the preparation of model catalyst, colloidal NP dispersions with defined particle size, shape, and composition can be applied.[84-85] In the first step the NP dispersion is synthesized by the reduction of the metal precursor (see Chapter 2.1). In a second step the formed NPs can be deposited onto any given support material (metal oxides or carbon).[86-88] The advantage of this preparation procedure is the separation of the particle formation and the deposition step, which allows the preparation of defined NPs (particle size

and shape) on different support materials. The NP size during the deposition step is not influenced and different metal loadings are feasible.

As discussed in chapter 2.2, colloidal NPs tend to minimize their free surface energy, which leads to agglomeration.[43-44] To prevent the NPs from coalescence, organic molecule such as polymers (e.g. PVP) or large organic molecules (e.g. oleylamine) are added to the reaction mixture that bind to the NP surface.[89-91] The ligand is present during the NP formation, which has consequences for the properties of the NP (size, shape etc.).[92] Furthermore, the organic molecules remain at the particle surface after deposition and are known to block catalytic active surface atoms[89] or enable alternative reaction pathways by ligand-reactant interactions.[93-95] Therefore, the organic molecules have to be removed prior to catalytic applications, which require an addition step with further energy and resource expense. One option for removal of organic molecules on supported NPs is a thermal treatment.[96-97] However, at high temperatures the mobility of the NPs on the support material increases and NP tend to agglomerate, which decreases the catalytic surface (see Figure 12a). Another option is the use of ozone at room temperature, but it has been shown that the organic molecules are not completely removed by ozone and catalytic performance of a catalyst is not reproducible (see Figure 12b).[98-99]

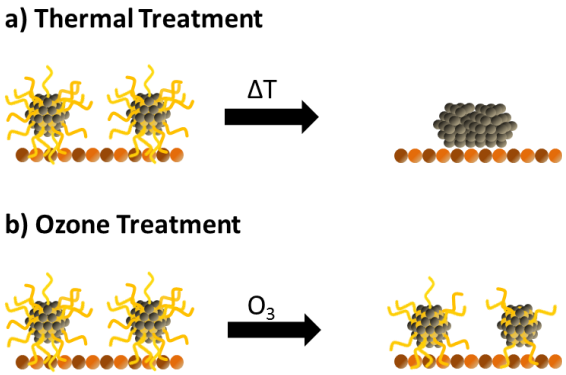

Figure 12: Removal of organic surfactant of colloidal NPs after deposition on support material. (a) Thermal treatment leads to agglomeration of the NPs. (b) Ozone treatment leads to incomplete ligand removal.

In the following, a synthesis approach of colloidal NPs is introduced, which enables the preparation of stable precious metal NPs (Pt, Ru, Rh) in the absence of protective agents such as surfactants, polymers, or organic ligands.[100]

4.2 Colloidal "surfactant-free" Platinum nanoparticles

In the year 2000 the "alkaline polyol approach" for precious metal NPs (Pt, Ru, Rh, Ir) was established by Wang et al.[100] The formation of the NPs proceeds in alkaline ethylene glycol (EG), which acts on the one hand as reducing agent and on the other hand stabilizes the NPs without the need of

polymers (e.g. PVP) or large organic molecules (e.g. oleylamine). First, these NPs were named "unprotected" due to the absence of strong binding organic molecules on the particle surface.[100-101] However, surfaces free of adsorbates are not stable under ambient conditions and can only be generated in ultra-high vacuum (UHV).[102] It was stated that the particles may be stabilized by the solvent (EG), oxidation products of EG (e.g. glycolate, acetate etc.) and/or anions (e.g. OH^-), which are adsorbed on the surface. A detailed study of the surface chemistry of these "unprotected" Pt NPs by NMR spectroscopy clearly revealed that no surface-bound C-H containing species are present at the surface.[101] Hence, organic molecules such as EG or oxidation products are not bound to the surface of these colloidal NPs. Further experiments using ATR infrared spectroscopy revealed that these NPs are covered with CO[101], which is consistent with the fact that Pt is known to catalyse the oxidation of alcohols to CO.[103-104] However, the adsorption frequency of CO on the as-prepared Pt NPs matches with the singleton frequency of Pt NPs, indicating that CO is diluted with another adsorbed species. A full monolayer of CO causes dipole-dipole coupling of adjacent CO, which leads to a significant blue shift of the adsorption band.[90, 105] The need of alkaline conditions during the NP synthesis suggests that OH^- in addition to CO is adsorbed on the particle surface to prevent the NP from sintering.[101] The NPs can hence not be considered as "unprotected". Hereinafter, the NPs are called "surfactant-free" NPs to prevent misunderstandings.

The established synthesis route for "surfactant-free" Pt NP with H_2PtCl_6 as precursor and 0.25 M NaOH in EG leads to small NPs (1.2 nm ± 0.2 nm) with a narrow size distribution.[100] For the use of these colloidal NPs in heterogeneous catalysis the NPs have to be deposited onto a support material, which requires additional preparation steps. First, the NPs have to be isolated from the solvent. EG is a high boiling solvent (198°C), which complicates evaporation. Hence, the NPs can be isolated by lowering the pH value of the dispersion with 1 M HCl. The NPs precipitate and can be separated from the reaction media by centrifugation.[106] Due to the acidic conditions the OH^- on the particle surface is neutralised and the particles are merely protected by CO.[107] In the next step, these particles can be re-dispersed in low boiling polar solvents (e.g. acetone, cyclohexanone).[107-108] The addition of the support material and removal of the solvent leads to supported NPs, which can be used directly in heterogeneous catalysis (see Figure 13).[94, 107] Another option is the change of the CO covered to OH^- covered NPs due to phase transfer of NPs in cyclohexanone to an aqueous alkaline solution. The OH^- covered NPs can be isolated as solid powders, stored, afterward be redispersed in organic solvents, and for instance be deposited onto support material without loss of catalytic performance.[107] The potential of supported "surfactant-free" Pt NPs in liquid phase hydrogenation and in electro catalytic application (oxygen reduction reaction) was demonstrated recently.[94, 107, 109]

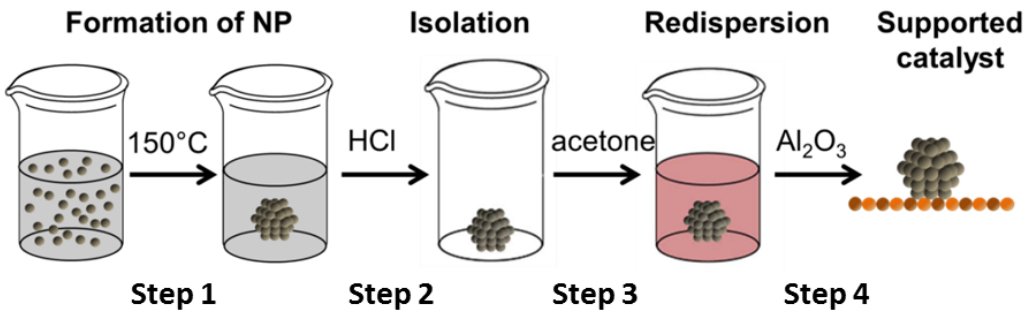

Figure 13: Preparation procedure of heterogeneous catalyst using "surfactant-free" Pt NPs. The formation of Pt NPs proceeds in alkaline EG at 150°C due to reduction of H_2PtCl_6 (step 1). The NPs are isolated by lowering the pH value, which leads to precipitation of the NPs. To remove residual EG, the NPs are washed once with HCl (step 2). Then the isolated NPs are re-dispersed in organic medium (e.g. acetone, EG, cyclohexanone, step 3). The addition of the support material (e.g. Al_2O_3) and removal of the solvent leads to supported NPs as model catalysts in heterogeneous catalysis (step 4). (Reprinted with the permission of Wiley, ChemNanoMat, 2019, 5, 4, 462-471)

4.2.1 Size control of "surfactant-free" Platinum nanoparticles

For systematic studies in heterogeneous catalysis it is essential to prepare model catalysts of different particle sizes to explore e.g. structure sensitivities. The common strategy to control the size of colloidal NPs is the addition of PVP to the EG, which leads to Pt NPs with a size range of 1 – 7 nm.[110] However, as discussed in chapter 4.1.2 PVP binds at the NP surface and has to be removed before catalysis. In the case of "surfactant-free" Pt NPs several approaches have been discussed for size control. In the work of Wang et al. it was shown that the size of the NPs can be increased from 1 nm to around 4 nm by adding water to the reaction mixture.[100] However, this procedure leads to significant losses of NPs due to particle sintering and the resulting dispersions exhibit very limited stability. In fact, the losses are so high that the recipe cannot be used for the preparation of supported catalyst. Therefore, other strategies were discussed based on the understanding of the surface chemistry of "surfactant-free" Pt NP.

As shown in chapter 4.2, the "surfactant-free" Pt NPs are supposed to be protected by CO and OH^-.[101] It was found that the presence of OH^- is essential to obtain stable NP dispersions and it was discussed that the pH value of the precursor solution influences the particle formation and thus the particle size.[100-101, 109, 111-112] However, the pH scale is defined for aqueous media and cannot be applied to EG solutions. Hence, the OH^- concentration of the precursor solution in EG was varied and it was found that with decreasing OH^- concentration the particle size increased.[94, 101, 109] Taking into account that the OH^- concentration of the reaction mixture decreases during reaction (proton formation during reduction of H_2PtCl_6 and neutralization with OH^-) a minimal starting OH^- concentration was found, which leads to stable dispersions. Solutions with lower OH^- concentrations lead to unstable dispersions with agglomerated NPs, which indicates that the presence of OH^- after

NP formation is important to stabilize the NPs. In a detailed study about the OH^- concentration in Pt NPs dispersions, it was found that not the absolute OH^- concentration determines the particle size, but the molar ratio of OH^-/Pt. For high OH^-/Pt ratios small particles are formed, whereas low OH^-/Pt ratios led to larger particles of up to 5 nm.[109]

5. Aim of the work

The aim of this project was to explore the influence of particle size and the interaction between precious metal NPs (Pt in this case) and the support material on the catalytic performance. The established synthesis approach of “surfactant-free” Pt NPs, which allows the independent control of the material properties (NP and support), was used to prepare supported NP catalysts.

The first aim was to study the stability of these colloidal NP in presence of halides. Halides are present during the preparation procedure (H_2PtCl_6 is used as precursor and HCl for the isolation step, see Figure 13), which may influence the colloidal stability (leaching and Ostwald ripening) as well as the catalytic performance (chloride may act as a catalyst poison).

The catalytic performance of supported NP catalyst depends strongly on the NP properties (e.g. size) and therefore an essential challenge was to develop a reproducible synthesis method to control the size of the “surfactant-free” Pt NPs with narrow size distribution in the range < 5 nm, where the ratio of low and high coordinated surface atoms varies mostly. These NPs were supported onto different support materials (inert support material and reducible support materials) in order to systematically study the influence of particle size effects and metal-support interaction with CO oxidation as a model reaction.

6. Stability of “surfactant-free” Platinum nanoparticles

(Relevant paper I)

The potential of “surfactant-free” Pt NP as heterogeneous catalysts was demonstrated in liquid phase hydrogenation reactions and in electro catalytic oxygen reduction reaction.[94, 107, 109] However, knowledge about the stability of these catalysts is still scarce. Known degradation pathways of heterogeneous NP catalysts are:

i) **Sintering:** At high reaction temperature the mobility of the NPs increases and NPs tend to agglomerate to decrease their surface energy.[113-114] The formation of agglomerates leads to a lowering surface area, which as a result leads to a decreased catalytic activity (see Figure 14).[115]

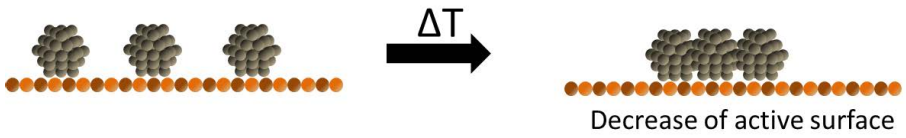

Figure 14: Sintering of NPs at high temperature.

ii) **Desorption:** In liquid media the NP can desorb from the support material into the reaction medium, which leads to a loss of precious metal on the catalyst and the reaction medium becomes contaminated with metal traces (see Figure 15).[116]

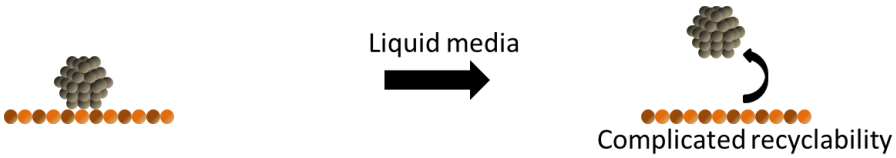

Figure 15: Desorption of NPs from the support material in liquid media.

iii) **Leaching:** Halides are known to cause dissolution of the NPs (leaching) and soluble atomic species are generated (see Figure 16).[117]

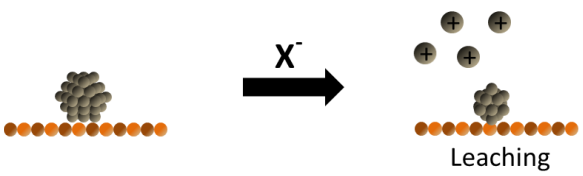

Figure 16: Leaching of NPs in presence of halides (X¯).

iv) **Ostwald ripening:** A possible subsequent step after leaching of NPs is Ostwald ripening, which leads to growth of larger particles at the expense of small particles (see Figure 17).[118-120]

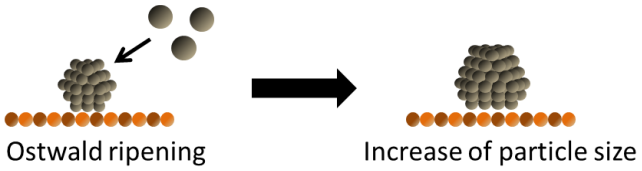

Figure 17: Ostwald ripening after leaching of NPs

The latter degradation pathways (leaching and Ostwald ripening) were especially discussed to proceed in electrochemical applications. Chloride and a certain potential was identified as the driving force for leaching.[121-122] Furthermore, chloride is known to act as a catalyst poison that binds strongly to the surface of the particles and blocks active sites.[123-124] However, the presence of chloride during catalyst preparation is difficult to avoid, since in most applications chloride containing precursors (e.g. H_2PtCl_6) are used, as they are chemically easy to produce and often the cheapest precious metal precursor. So far, little is known about the leaching of metal NPs in organic reaction media and under catalytic conditions.

6.1 Leaching of “surfactant-free” Platinum nanoparticles

Colloidal “surfactant-free” Pt NPs are an appropriate model system for systematic studies of leaching and Ostwald ripening of NPs due to following reasons:

i) “Surfactant-free” NPs are available as dispersions in the absence of a support material. The chemical nature and structure of the support material influences the stability of NPs. Furthermore, the leached soluble metal species or the halide could adsorb on the support material leading to a complex system for systematic investigations on leaching.

ii) These NPs are free of organic surfactants. Surfactants could interact with the halides or with the metal surface thus influencing the leaching process. “Surfactant-free” Pt NPs are only protected by CO and OH^-.[101, 107] CO is an adsorbate on precious metal surfaces in many catalytic processes.[125] It hence partially represents the chemical states of a precious metal surface under catalytic conditions.

iii) The influence of halides is relevant for the synthesis route. Usually chloride containing precursors (H_2PtCl_6) are used for the reduction to NPs and significant amounts of chloride (HCl) are added to the NPs dispersions for the isolation step (see Figure 13).[101, 107]

iv) The NPs can be transferred into different organic media, which allows studying the stability in different organic environments.

First, the influence of chloride on the stability of “surfactant-free” Pt NP dispersions was investigated. Therefore, the NPs were treated as shown in Figure 13 (steps 1-3). The as-prepared NPs in alkaline EG were precipitated with 1 M HCl and re-dispersed in pure EG without complete removal of HCl traces after rinsing of the NPs. In Figure 18 images of the solution after several days in the presence of HCl traces are shown.

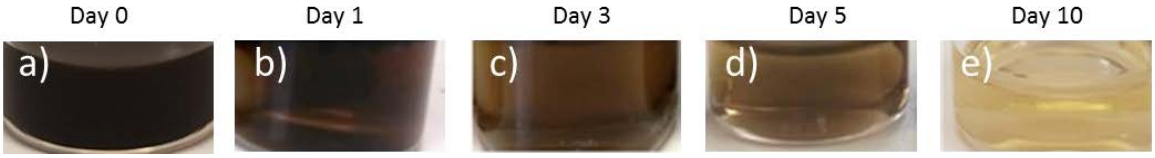

Figure 18: Optical properties of Pt NP dispersions in pure EG. Pt NPs were precipitated with 1 M HCl and re-dispersed in EG without complete removal of HCl traces. The stability of the dispersion was observed over 10 days. (Reprinted with the permission of Wiley, ChemNanoMat, 2019, 5, 4, 462-471)

The typical colour of Pt NP dispersions is dark brown[107, 126], which was observed for freshly re-dispersed Pt NP in pure EG after precipitation and rinsing with 1 M HCl (see Figure 18a). The presence of HCl traces led to a colour change with increasing exposure time from dark brown to light brown within 5 days (see Figure 18a-d). After 10 days an entirely yellow solution was obtained (see Figure 18e). It is known that Pt precursor salts such as platinum chlorides as dissolved species lead to a yellow solution.[127] The colour change in presence of HCl indicates that the NPs in the dispersion dissolve and soluble Pt species are generated. The same experiment was performed, after thorough removal of chloride traces after precipitation and rinsing (see Figure 19).

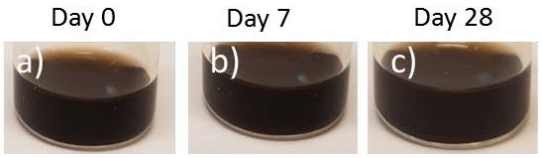

Figure 19: Optical properties of Pt NP dispersions in pure EG after thorough removal of HCl traces after precipitation. The stability of the dispersion was observed over 28 days.

The resulting dispersions do not alter their colour over more than 28 days (see Figure 19), which demonstrates that significant amounts of chloride are necessary for complete dissolution and formation of soluble Pt species. The stability of Pt NPs was investigated in other organic solvents (e.g. acetone) and it was found that leaching is accelerated in organic media with lower viscosity in

comparison to EG. The assumed leaching process in acetone was used for further characterization with X-ray adsorption spectroscopy (XAS) (see Figure 20).

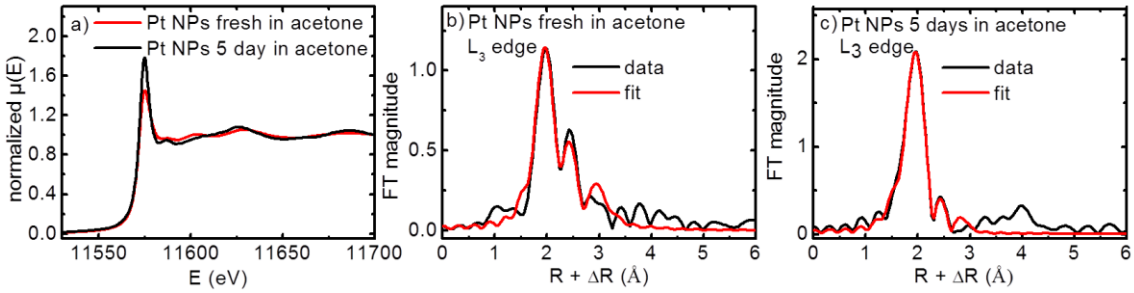

Figure 20: XANES spectra (Pt L_3-edge) for Pt NPs freshly re-dispersed in acetone (red) and after 5 days in acetone (black) (a) and Fourier-transform (FT) magnitudes of k^2-weighted EXAFS spectra (black) and the fits (red) at the Pt L_3-edge for freshly re-dispersed Pt NPs in acetone (b) and for Pt NPs stored 5 days in acetone (c). (Reprinted with the permission of Wiley, ChemNanoMat, 2019, 5, 4, 462-471)

X-ray absorption near edge structure spectra (XANES) demonstrate that a fresh sample of Pt NPs re-dispersed in acetone (after precipitation with HCl) shows mainly metallic character, whereas an aged sample of Pt NP in acetone in the presence of chloride anions reveals an increased amount of oxidized Pt species due to an increase in the white line intensity of the XANES spectra (see Figure 20a). In order to quantify the amount of metallic Pt^0 and soluble Pt species (Pt^{2+} and Pt^{4+}) a linear combination fitting analysis was performed with Pt foil and K_2PtCl_4 and K_2PtCl_6 as reference. The amount of metallic Pt^0 in a freshly prepared Pt NP dispersion in acetone decreased from 68 ± 2 wt% to 20 ± 7 wt% and the amount of soluble Pt species increased (33 ± 6 wt% for Pt^{2+} and 48 ± 2 wt% for Pt^{4+}) after storage for 5 days in acetone. From extended X-ray absorption fine structure (EXAFS) data the nature of the nearest neighbours of Pt were analysed (see Figure 20 b,c). A fresh prepared sample of Pt NP in acetone (in presence of chloride) showed that chloride binds to the surface of Pt NPs (partial coordination number of Pt-Cl of 1.4 ± 0.3). Whereas, the partial coordination number of Pt-Cl increased to 3.7 ± 0.4 for an aged sample, indicating that the colour change of the dispersion could be explained with metal leaching in presence of chloride.

In the next step the influence of oxygen in the leaching process was investigated. In C-C coupling reactions the oxidative addition of aryl halides was identified to cause leaching of NPs.[128-129] Therefore, leaching in the presence of halides and in an oxygen enriched atmosphere was investigated and the leaching process was accelerated. Within 2 days the colour of the NP dispersion changed to yellow, when a constant O_2 stream (5 mL/min) was added to the dispersion (see Figure 21a,b). Whereas without additional O_2 a colour change to yellow was observed after 10 days (compare Figure 18e and 21a,b).

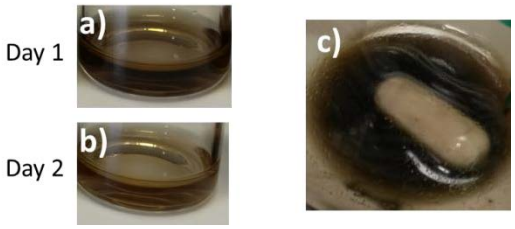

Figure 21: Optical properties of Pt NP dispersion in EG after precipitation with HCl and re-dispersion in EG. The NP dispersion were stored in presence of chloride in an O_2 enriched atmosphere for at least 2 days (a, b) and under inert gas atmosphere for 5 days (c). (Reprinted with the permission of Wiley, ChemNanoMat, 2019, 5, 4, 462-471)

Furthermore, the stability of the NP dispersion in the presence of halides was studies in the absence of oxygen (Ar atmosphere), where no colour change was observed (see Figure 21c). This leads to the conclusion that the leaching of Pt NPs proceeds by oxidative etching in the presence of halides and oxygen.

The leaching process was studied in the presence of different anions and the concentration of the leached soluble Pt species was determined with atomic absorption spectroscopy (AAS). For this purpose, Pt NP dispersions were prepared with different precious metal precursors and different acids were used for the precipitation step. Residual acid traces were removed thoroughly, which leads to optical stable dispersions for all investigated systems. Afterwards, the isolated NPs were re-dispersed in EG or alkaline EG. The concentration of the leached Pt ions was determined directly after precipitation (0 days) and after 7 and 21 day for the following Pt NP dispersions (see Table 1).

i) **H_2PtCl_6** was used as a chloride containing precursor and these particles were precipitated with HCl and oxalic acid (example of a halide free acid) and re-dispersed in pure EG and alkaline EG.

ii) **H_2PtBr_6** was used as a bromide containing precursor and these particles were precipitated with HBr and re-dispersed in EG.

iii) **$Pt(acac)_2$** as an example of a halide free Pt precursor was used and these particles were precipitated with HCl and oxalic acid and re-dispersed in EG. The latter represents a system, which is free of any halides.

Table 1: Concentration of soluble Pt species in the supernatant of dispersion prepared with H_2PtCl_6, H_2PtBr_6, and $Pt(acac)_2$ as precursor after exposure to chloride, bromide, and oxalate. The concentration of Pt ions was determined with AAS. (Reprinted with the permission of Wiley, ChemNanoMat, 2019, 5, 4, 462-471)

Precursor	**H_2PtCl_6*6 H_2O (i)**			**H_2PtBr_6*9 H_2O (ii)**	**$Pt(acac)_2$ (iii)**	
Acid Anion	Chloride	Oxalate	Chloride, Hydroxide	Bromide	Chloride	Oxalate
Day 0	0.16 %	0.07 %	0.16 %	6.90 %	9.94 %	9.88 %
Day 7	1.85 %	0.01 %	0.47 %	25.25 %	2.94 %	0.79 %
Day 21	0.16 %	0.03 %	0.44 %	45.35 %	1.99 %	1.92 %

In the presence of chloride only small amounts of soluble Pt ions in the supernatant were detected with AAS even after 21 day of exposure (see Table 1). In contrast, a purely bromide based system (H_2PtBr_6 as precursor and HBr for precipitation) showed a strongly increased concentration of Pt ions in the supernatant (see Table 1). After 21 days 45% of the total Pt amount in the dispersion was detected as Pt ions in the supernatant. The high Pt ion concentrations detected for supernatants with $Pt(acac)_2$ as precursor after the isolation (day 0) is related to a limited reducibility of $Pt(acac)_2$ under given reaction conditions (see Table 1). After 7 days and 21 days (Pt NPs with $Pt(acac)_2$ as precursor) exposure to chloride and oxalate only low concentrations of soluble Pt species were detected in the supernatant (see Table 1). However, the presence of soluble Pt ions indicates that leaching in presence of halides takes place.

Ostwald ripening is a possible subsequent step after leaching and leads to an increase of the particle size with time. Therefore, transmission electron microscopy (TEM) analysis was performed of Pt NPs (H_2PtCl_6 and H_2PtBr_6), which were exposed to chloride, oxalate, OH^- and bromide. Furthermore, the halide free Pt precursor ($Pt(acac)_2$) was used and precipitated with oxalic acid (completely free of halides) and HCl as a benchmark experiment.

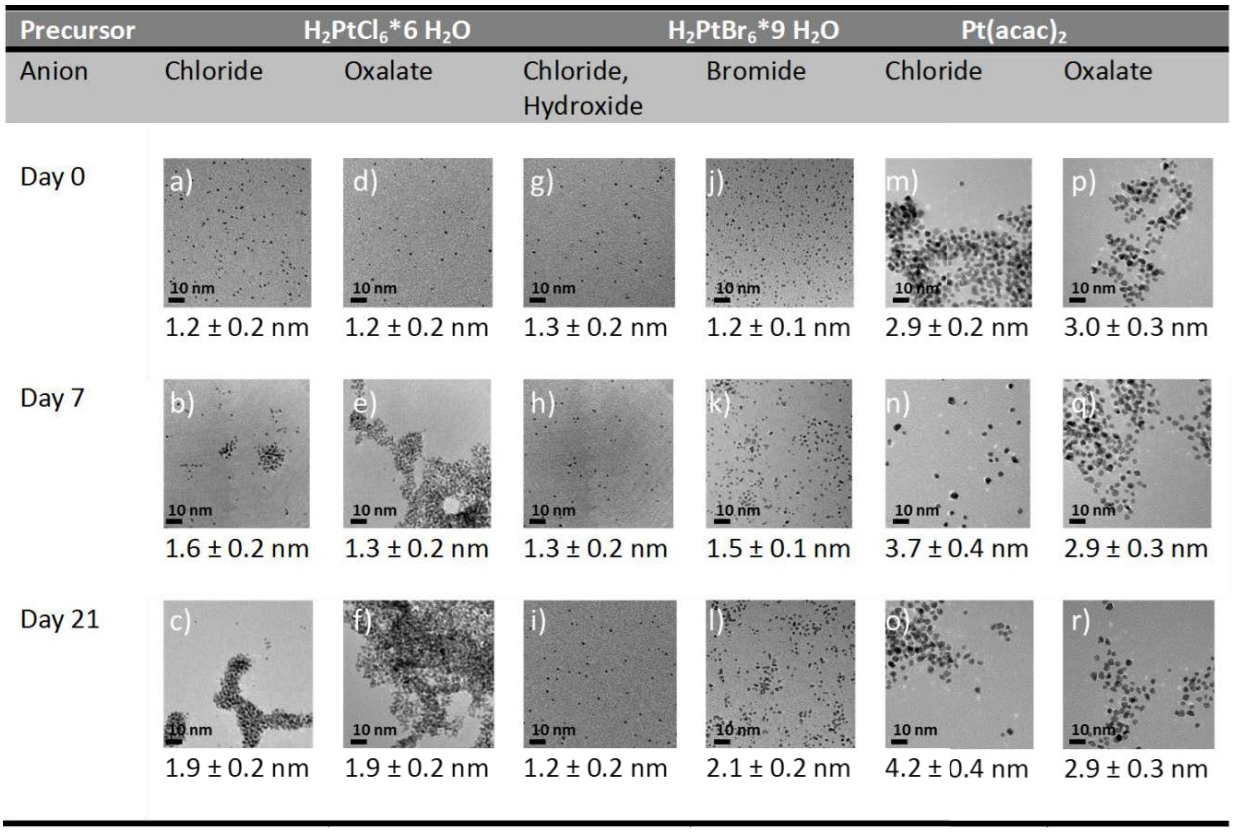

Figure 22: Particle size analysis of Pt NPs prepared with H_2PtCl_6, H_2PtBr_6 and $Pt(acac)_2$ as precursor salts by counting at least 200 particles. The NPs were exposed to 1 M chloride, 1 M oxalate, 0.5 M hydroxide, and 1 M bromide and the particle size was determined after 0, 7, and 21 days. (Reprinted with the permission of Wiley, ChemNanoMat, 2019, 5, 4, 462-471)

The synthesis of Pt NPs with H_2PtCl_6 and H_2PtBr_6 leads to a mean particle diameter of 1.2 nm ± 0.2 nm, whereas $Pt(acac)_2$ as precursor leads to particles with 3.0 nm ± 0.3 nm. With increasing exposure time to HCl and HBr the size of the NPs increases significantly (see Figure 22 a-c, j-l), indicating that halides promote Ostwald ripening. Interestingly, precipitation of Pt NPs (H_2PtCl_6 as precursor) with oxalic acids shows an increase of the particle size, demonstrating that even chloride traces from the precursor initiate Ostwald ripening (see Figure 22 d-f). In the presence of OH^- no increase of the particle size could be observed (see Figure 22 g-i). As discussed in chapter 4.2 the presence of OH^- as a protecting species during the synthesis of Pt NP is essential for colloidal stability.[101, 107, 109] The binding of OH^- at the NP surface electrostatically protects the NP from the negatively charged halides and Ostwald ripening is inhibited (see Figure 23).

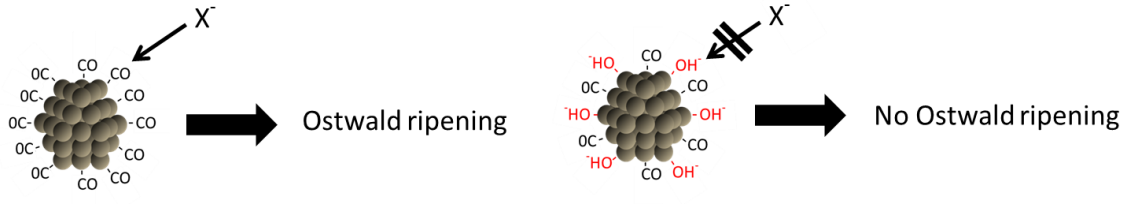

Figure 23: Influence of the alkaline medium on Ostwald ripening of Pt NPs.

To demonstrate that the halide induce Ostwald ripening the particle size of a halide free synthesis with $Pt(acac)_2$ as precursor and oxalic acid for precipitation was analysed and no differences of the particle size could be observed (see Figure 22 p-r). As a control experiment the same particles were precipitated with HCl and a significant increase of the particle size could be observed (see Figure 22 m-o). The results clearly show that the presence of halides induces Ostwald ripening.

6.2 Ostwald ripening for particle size control

(Relevant paper I)

In the next step the knowledge of leaching and subsequent growth (Ostwald ripening) was explored as controlled way to vary the size of “surfactant-free” Pt NP. It was shown that halide traces from the precursor are sufficient to induce Ostwald ripening (see Figure 22 d-f). To accelerate Ostwald ripening a reducing atmosphere was used and therefore the reaction time in alkaline EG at 150°C was varied. The development of the particle size during the synthesis with H_2PtCl_6, H_2PtBr_6 and $Pt(acac)_2$ is shown in Figure 24.

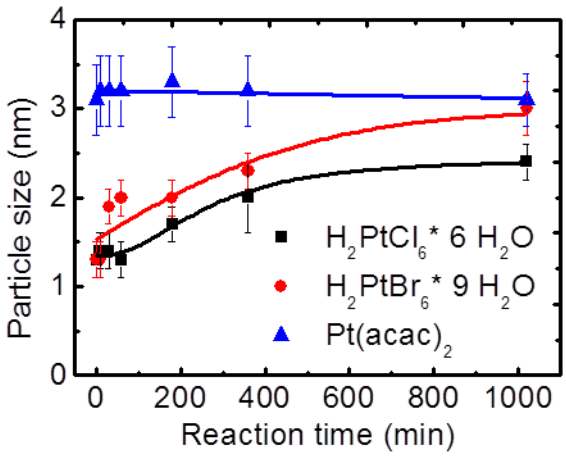

Figure 24: Effect of the reaction time on the resulting particle size of Pt NPs during the synthesis in alkaline EG at 150°C. The synthesis was performed with H_2PtCl_6 (black), H_2PtBr_6 (red) and $Pt(acac)_2$ (blue) as precursor for 17 h. The trend lines serve as a guide to the eye and have no physical meaning. (Reprinted with the permission of Wiley, ChemNanoMat, 2019, 5, 4, 462-471)

The synthesis with H_2PtBr_6 leads to a faster particle growth compared to the particle formation with H_2PtCl_6 (see Figure 16). This is in accordance with the fact that in presence of bromide significantly more soluble Pt ions are formed than in the presence of chloride. The reducing atmosphere during the synthesis enhances the reduction of the leached Pt species and the growth of the NPs is favoured. No particle growth was observed for $Pt(acac)_2$ as precursor, demonstrating that halides are essential for Ostwald ripening (see Figure 24).

The here introduced concept for a precise size control of “surfactant-free” Pt NPs by targeted Ostwald ripening in the presence of chloride and bromide leads to a size range of 1 to 4 nm using H_2PtCl_6 (1 nm), H_2PtBr_6 (2 nm) and $Pt(acac)_2$ (3 nm and 4 nm) as precursor. Pt NPs with 4 nm particle size are obtained during Ostwald ripening at room temperature using $Pt(acac)_2$ as precursor and the presence of chloride. However, the particle growth via Ostwald ripening needs at least 21 days to receive a particle size of 4 nm (see Chapter 6.1, Figure 22 o). Therefore, small amounts of chloride were added during the formation of Pt NPs with $Pt(acac)_2$ as precursor in alkaline EG in order to accelerate Ostwald ripening in a reducing atmosphere. However, the presence of chloride during the NP formation with $Pt(acac)_2$ as precursor leads to agglomeration of the NPs. To overcome these disadvantages the known concepts for size control of “surfactant-free” Pt NPs (see chapter 4.1) were combined with the new findings in terms of leaching and Ostwald ripening by variation of:

i) the OH^- concentration during the synthesis[101, 109]

ii) the applied metal precursor

iii) the reaction time and halide during synthesis to induce leaching and Ostwald ripening

NP dispersion could be prepared with narrow size distribution in a size range of 1 – 4 nm (see Figure 25). A further particle size increase was not feasible using “surfactant-free” preparation methods. A further extension of the reaction time in alkaline EG led to particles, which contained significant amounts of organic residues on the particle surface and are hence no more “surfactant-free”. Another option was the decreasing OH^- concentration in the reaction medium using $Pt(acac)_2$ as a precursor. However, the yield of Pt NPs with low OH^- concentrations was too low for the preparation of supported model catalysts.

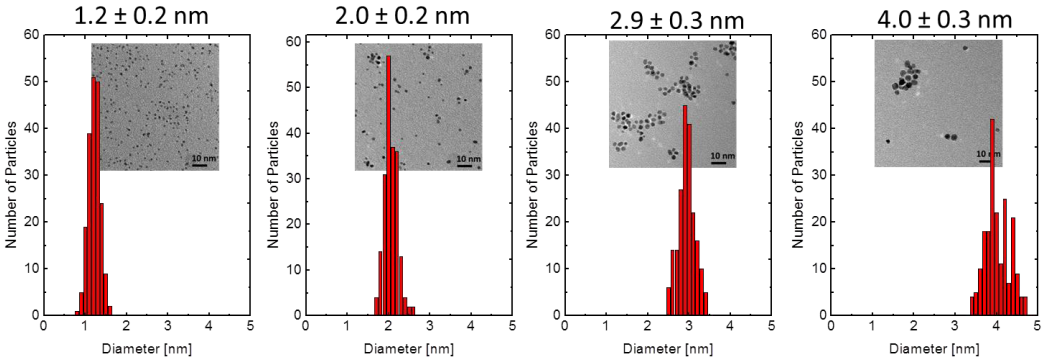

Figure 25: Particle size distributions and TEM images of colloidal “surfactant-free” Pt NPs with a size range of 1 – 4 nm. (Reprinted with the permission of Elsevier, Journal of Catalysis, 2019, 377, 662-672)

The aim was to explore the stability of “surfactant-free” Pt NPs and it was found that halides traces from the used metal precursor and from the isolation procedure induce dissolution of the NPs. The formed soluble Pt species lead to NP growth. The Ostwald ripening in presence of halides was further used to control the size of “surfactant-free” Pt NPs, which was a further aim of this work and Pt NPs dispersions in a size range of 1 – 4 nm were obtained.

6.3 Characterization of Platinum nanoparticles supported on Al_2O_3

(Relevant paper I, II)

The colloidal “surfactant-free” Pt NPs (1 – 4 nm) were all prepared in alkaline EG and the resulting dispersions were stable over several months without visible NP aggregation. These NPs can be used directly to prepare supported NP catalyst for heterogeneous catalytic applications. All NPs dispersion (1 – 4 nm) could be precipitated by lowering the pH value with 1 M HCl and rinsed with acid to remove residual EG traces. The isolated NPs can be re-dispersed in low boiling solvents (acetone used in this case) and addition of any given support material leads to heterogeneous catalyst without the need of further pre-treatment before catalysis (see Figure 13, step 4).

6.3.1 TEM images

For further characterization these NPs were supported onto γ-Al_2O_3. TEM measurements were performed for the supported Pt NPs on Al_2O_3 before catalysis and after heat treatment and exposure to reducing conditions (5% H_2 at 200°C) (see Figure 26).

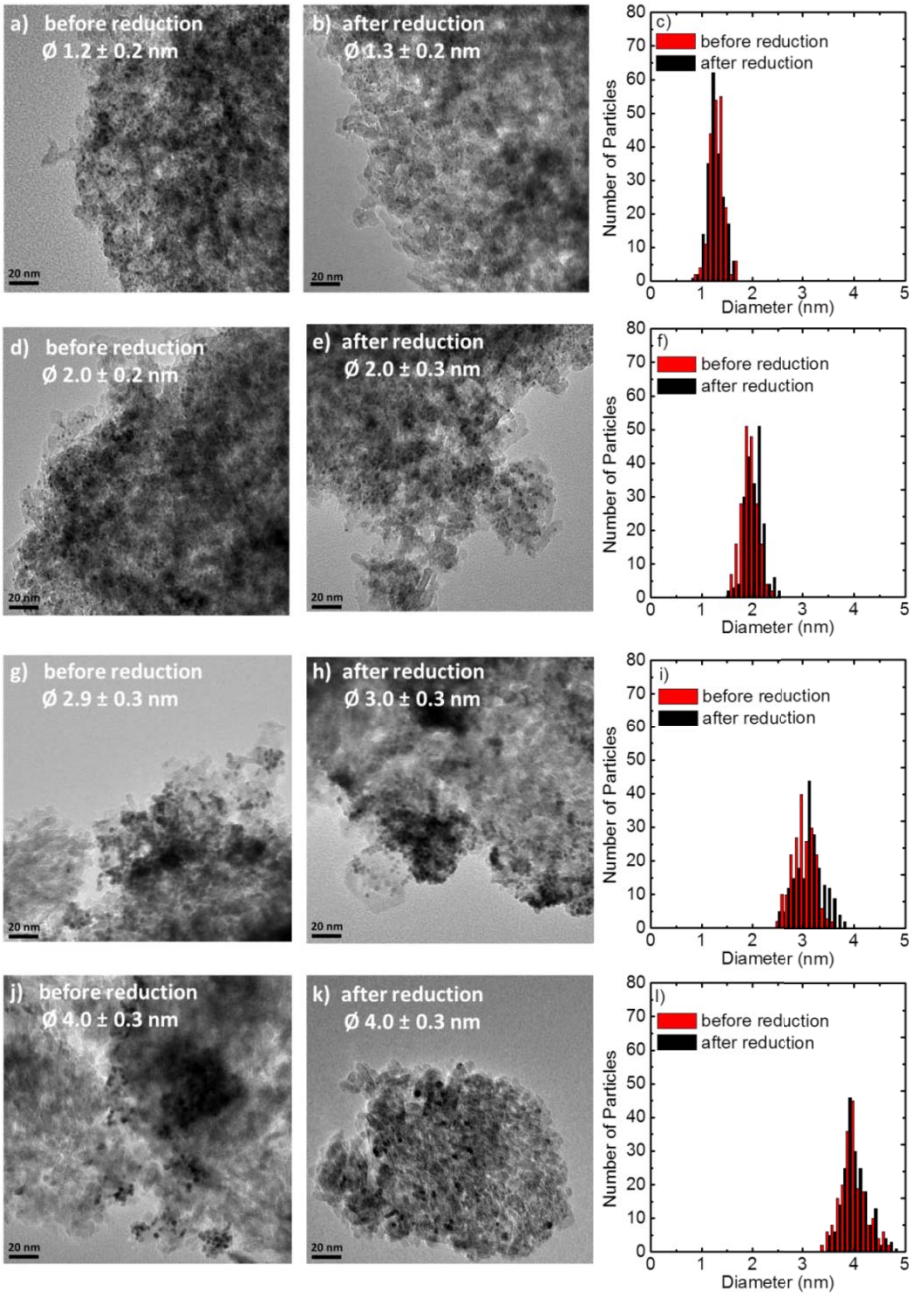

Figure 26: TEM images of supported “surfactant-free“ Pt NPs on Al_2O_3 before (a, d, g, j) catalysis and after heat treatment with 5% H_2 for 2 h at 200°C (b, e, h, k) and the corresponding particle size distributions (c, f, i, l). (Reprinted with the permission of Elsevier, Journal of Catalysis, 2019, 377, 662-672)

The TEM images clearly indicate that the particle size does not change after the supporting step. Furthermore exposure to 200°C does not alter the particle size and no agglomeration was observed (see Figure 26).

6.3.2 Solid state ^{13}C NMR

In order to exclude significant amounts of organic residues from the preparation procedure on the surface of supported Pt NPs catalysts with particle sizes of 1 – 4 nm, the catalysts were investigated with ^{13}C solid state NMR. The Pt NPs on Al_2O_3 were exposed to ^{13}CO and a pronounced NMR signal was found at 162 ppm, which was identified as carbonate species formed on Al_2O_3 (see Figure 27 a).[130] The absence of further signals indicates that no significant amounts of carbon containing species are present on the Pt surface. In order to demonstrate the suitability of solid state NMR for the characterization of supported Pt NPs, a sample was prepared, which contained oxidation products of EG on the catalyst surface due to an enhanced reaction time in alkaline EG. A NMR signal at 64 ppm is clearly visible (see Figure 27 b). The chemical shift of 60 ppm is known for organic molecules at Pt surfaces. Consequently, the catalyst surfaces prepared from “surfactant-free” Pt NPs are free of significant amounts of organic residues and can hence be used as heterogeneous catalyst without the need of ligand removal before catalytic studies.

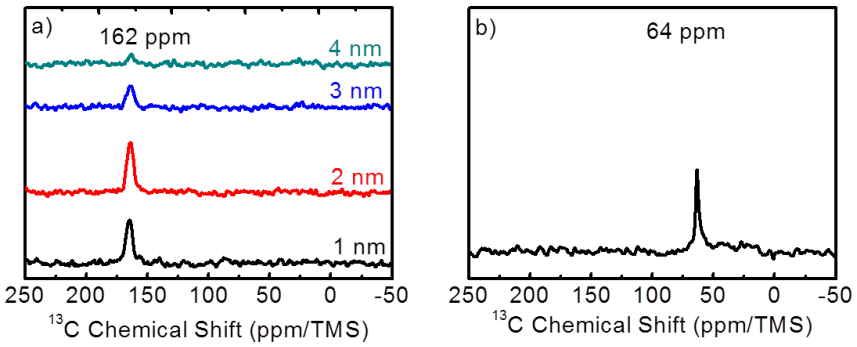

Figure 27: Solid state ^{13}C NMR spectra of „surfactant-free“ Pt NPs on Al_2O_3 (1 – 4 nm particle size, a) after exposure to ^{13}CO and a reference spectrum with organic molecules at the particle surface (b). (Reprinted with the permission of Elsevier, Journal of Catalysis, 2019, 377, 662-672)

6.3.3 Influence of halide traces

The preparation procedure of colloidal “surfactant-free” Pt in alkaline EG requires the use of chloride or bromide containing precious metal precursors in order to obtain small NPs. Furthermore, HCl traces are present from NP isolation and rinsing. Chloride is known to influence the catalytic performance in electrochemical applications and it was discussed that chloride may act as a catalyst poison in heterogeneous catalysis.[121-124] Therefore, the here prepared catalysts were investigated in STEM modus and EDX spectra were recorded. During the EDX measurements no chloride or bromide

was found on the catalysts, when they were washed intensively with acetone after NP deposition. Additionally, the absence of halides on the catalysts surface was demonstrated by investigation of the catalytic properties of Pt NPs with the same particle size, but with different halides during the NP formation. Therefore, small Pt NPs (1 nm and 2 nm) were prepared either with a chloride or a bromide containing precursor and the activities of colloidal prepared Pt NPs with 3 nm were compared with an industrial catalyst (provided by Clariant) with an average particle size of 3 nm ± 1 nm. As a model reaction the oxidation of CO was used (see Table 2).

Table 2: Catalytic activity from steady state measurements with supported Pt NPs with 1 nm, 2 nm, 3 nm particles size with different preparation procedures in absence and presence of halides. CO oxidation was used as a model reaction at 200°C and partial pressures of 6.8 kPa for O_2 and 0.39 kPa CO.

Particle size	Used precursor	Steady state Activity ($mol_{CO2}/mol_{Surface\ Atom}s$)
1 nm	H_2PtCl_6	0.22
1 nm	H_2PtBr_6	0.21
2 nm	H_2PtCl_6	0.47
2 nm	H_2PtBr_6	0.46
3 nm	$Pt(acac)_2$	0.20
3 nm	Industial	0.22

Comparing the activities of Pt NPs with 1 nm and 2 nm particles size with different preparation procedures (chloride or bromide containing precursors) indicates that the activity is not influenced by either chloride or bromide. Furthermore, colloidal Pt NPs with 3 nm particle size and an industrial catalyst with similar particle size exhibits similar activities (see Table 2). The difference of the activities depends therefore only on the particles size, which is discussed in the following chapter and not to any artefact from the preparation procedure of the colloidal NPs.

The here presented preparation strategy of supported Pt NPs in a size range of 1 – 4 nm allows to prepare tailored model catalyst for heterogeneous catalysis reaction with the ability to change (see Figure 28)

i) the active metal component (in this work the focus is on Pt NPs, but the reaction procedure is similar for Ru and Ir NPs)
ii) the particle size (the here presented preparation strategy allows to tune the particle size with narrow size distribution in a range of 1 to 4 nm.)
iii) the influence of the support material (e.g. strong metal support interaction (SMSI) effects can be studied)
iv) the composition (in case of bimetallic NPs)

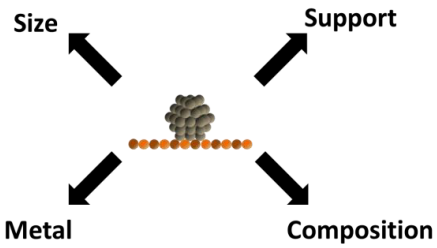

Figure 28: The here presented preparation procedure of “surfactant-free” Pt NPs allows varying the particle size, the metal, the composition, and the support material independently.

In the following, these heterogeneous catalysts were applied to study systematically the catalytic performance of CO oxidation depending on i) the particle size ii) the influence of metal support interactions and iii) bimetallic NPs.

7. Catalytic CO oxidation

Carbon monoxide is a toxic gas and the toxicity is related to the strong binding of CO to the iron atom of haemoglobin. The oxygen transport is hindered, which leads to an oxygen deficiency and suffocation.[131] CO is produced by incomplete combustion of hydrocarbons, for example when burning wood, coal, plastic, or by the combustion of fuel in car engines.[132-134] In order to minimize the CO emission, CO in the presence of oxygen is converted to the less harmful CO_2. However, the reaction of CO and O_2 requires activation and dissociation of O_2. Hence an efficient catalyst must be able to decrease the activation barrier for O_2 dissociation, release oxygen, and activate CO.[135]

A further important application for catalytic CO oxidation is the selective conversion of CO in hydrogen streams.[136-138] Hydrogen is an energy carrier that can be converted in fuel cells for energy generation. However, CO traces are known to strongly bind to active sites of the precious metal electrodes in the fuel cell. As a result, the active sites of the electrodes decrease by poisoning with CO and the efficiency of the fuel cell is lowered.[139] In order to avoid this deactivation, CO has to be removed from the gas stream by selective oxidation to CO_2, which does not strongly interfere with precious metal surfaces.

Besides its industrial importance, CO oxidation is often used as a model reaction in academic research due to the formation of CO_2 as the sole product and the seeming simplicity of the overall reaction ($2\ CO + O_2 \rightarrow 2\ CO_2$).[140] CO oxidation is effectively catalysed by late transition d-metals (Pt, Pd, Ru, Rh, Ir).[141-142] The focus at this work is CO oxidation on supported Pt NPs. CO oxidation on Pt has been extensively investigated in surface science studies under ultra-high vacuum (UHV) conditions and under catalytically relevant condition, but the mechanism and in particular particle size effects (structure sensitivity) are still controversially discussed.[125, 142-145]

Generally the mechanism for CO oxidation on Pt surfaces is described to occur via a Langmuir Hinshelwood mechanism (see Chapter 3.1.1) with competitive adsorption of CO and O_2 on the catalyst surface followed by O_2 dissociation.[146-148] These necessary adsorption steps are discussed in the following.

7.1 Adsorption of CO on Platinum

CO is known to chemisorb molecularly and strongly on Pt surfaces with the carbon atom bond to the surface. The strong interaction of Pt and CO can be explained by the Blyholder model (see Figure 29).[149]

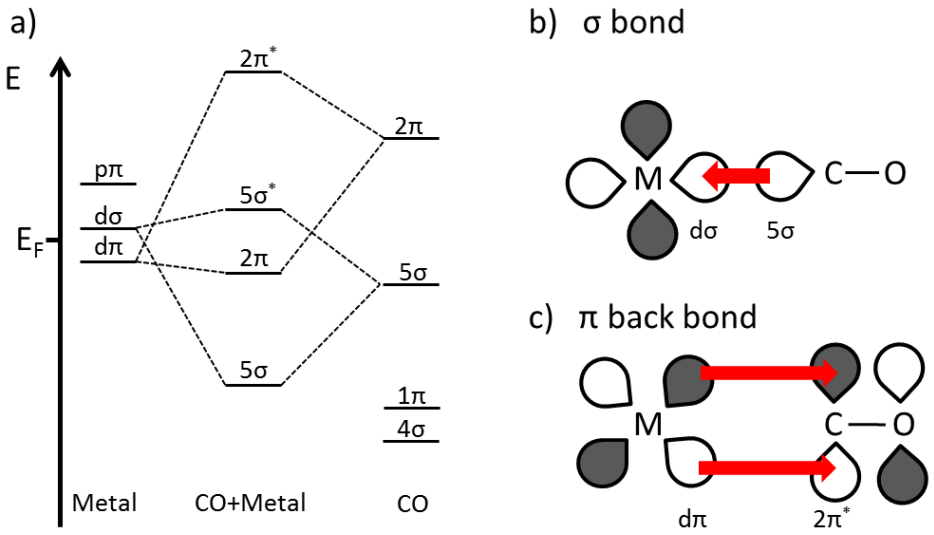

Figure 29: (a) MO scheme of the Blyholder model of the CO bond to a d-transition metal. (b) illustrates the σ bond of the 5σ orbital of the CO and the empty d-band of the metal. (c) demonstrates the π back bond of the filled d-band of the metal with the 2π orbital of the CO.*

The first bond, which describes the interaction of Pt and CO is the dative bond between the highest occupied molecular orbital (HOMO), 5σ orbital) and the empty d-band of the metal (see Figure 29b). The second bond is the π-back donation from the filled metal d-band to the lowest unoccupied molecular orbital (LUMO) of the CO molecule (2π* orbital) (see Figure 29c).[150] The strength of the CO bond to transition metal is mainly determined by the π-back donation that results in different CO adsorption energies on different adsorption sites. For low-coordinated surface sites (corner and edge atoms) the d-band centre of the metal shifts towards the Fermi level (E_F), which means that the π-back donation increases and the CO binds stronger at low coordinated surface sites.[151] A Pt surface, which is covered with a monolayer of CO, is catalytically inactive, since the strong adsorption of CO on Pt inhibits adsorption and dissociation of O_2. From surface science studies on Pt single crystals it was found that CO starts to desorb at 177°C from terrace atoms and at 277°C from low coordinated sites.[152] This explains that in order to proceed effectively temperatures of ≥170°C are needed for CO oxidation. In this temperature regime the reaction is limited by CO desorption from the catalyst surface, which means that CO is the most abundant reaction intermediate (MARI) and negative reaction orders for CO are observed in kinetic studies.[125, 142-143] With increasing reaction temperature the CO* coverage decreases and empty surface sites (*) replace CO* as the MARI. At high temperatures the Pt surface is essentially uncovered during the reaction, which results in a change of the kinetic regime and reaction rates are insensitive to CO partial pressure.[143]

7.2 Dissociation of oxygen on Platinum

The Langmuir Hinshelwood mechanism requires that besides CO also O_2 adsorbs on the Pt surface. From surface science studies with Pt surfaces it is known that O_2 adsorbs in a molecular state at temperatures < -123°C. Hence, under catalytically relevant conditions (T > -123°C) O_2 dissociates and an atomic overlayer is formed.[153] For stepped Pt surfaces it was found that low coordinated sites bind oxygen molecules stronger than terrace atoms and a higher dissociation rate of O_2 was observed on atoms with low coordination number.[154] However, under realistic reaction conditions O_2 adsorbs on surfaces with adsorbed CO. In order to describe the probability of adsorption of a molecule to the surface, the sticking coefficient was defined as the ratio of molecules being bound to the surface compared to the number of collisions of the adsorbate molecule with the surface.[155] The sticking coefficient of oxygen on a Pt(110) single crystal depends on the CO coverage. Imbihl and Ertl demonstrated that the surface structure changes from a 1 x 2 structure with a sticking coefficient of oxygen of S = 0.3 – 0.4 on a clean Pt surface and changed to a 1 x 1 structure with S = 0.5 – 0.6 on a CO covered surface.[156] Consequently, O_2 adsorption depends strongly on the reaction conditions and the catalyst surface and it was found that the changes of the surface structure leads to oscillations in the steady state rate during CO oxidation.[156-157]

7.3 Exclusion of heat and mass transfer limitations

(Relevant paper II)

The aim of this work was to determine the intrinsic kinetics of CO oxidation on supported Pt catalysts with different particle sizes. For this purpose, heat and mass transport limitations have to be excluded. Therefore, different tests were performed before conducting kinetic studies and in order to achieve differential operation conditions the conversion was keep below 10 % for all catalysis experiments.[68, 158]

CO oxidation is an exothermic reaction and the production of heat during the reaction might lead to a strong heating of the catalyst bed, which results in higher catalytic activities. In order to avoid heating up of the catalyst bed, the catalysts were diluted with inert support material and the required dilution ratio was determined. Therefore, the catalytic activity was determined for the undiluted catalyst and activities of different dilution ratios with Al_2O_3 as inert material were performed (see Figure 30).

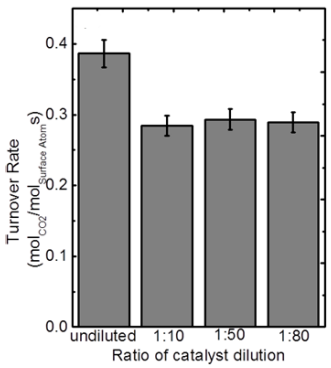

Figure 30: Test for the absence of heat transfer limitations. The TOF was determined of an undiluted catalyst and dilution ratios of 1:10, 1:50, and 1:80 (catalyst : Al_2O_3) were prepared and TOF values were determined. The amount of catalytic relevant Pt was constant in all experiments. (Reprinted with the permission of Elsevier, Journal of Catalysis, 2019, 377, 662-672)

The undiluted catalyst showed a significantly higher TOF than the diluted catalyst with a dilution ratio of 1:10. A further dilution (up to a ratio of 1:80) leads to no further decrease of the TOF, which indicates that a dilution of 1:10 is sufficient to exclude heat transfer limitations (see Figure 30). In this work a dilution ratio of 1:50 was chosen.

In heterogeneously catalysed gas phase reactions the transfer of the reactants to the catalyst has to be considered. In order to determine possible external transfer limitation the total gas flow was varied in a range of 100-200 sccm and the space velocity was calculated (see Figure 31).

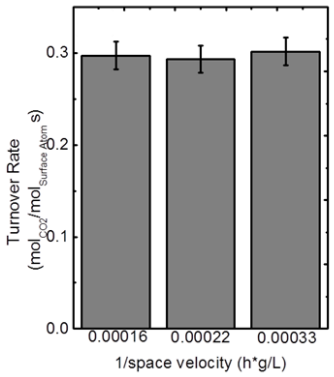

Figure 31: Test for external mass transfer limitations. The total gas flow was varied and the space velocity was calculated. The TOF was determined for different space velocities. (Reprinted with the permission of Elsevier, Journal of Catalysis, 2019, 377, 662-672)

For all space velocities identical TOF values were obtained, which indicates that the catalytic performance is not influenced by external mass transfer limitations (see Figure 31).

Finally, the reactants have to diffuse to the active sites in the porous catalyst and hence internal mass transfer limitations could influence the catalytic performance. Therefore, the Madon-Boudart

test was performed and catalysts with different metal loadings were prepared (0.25 wt%, 0.5 wt%, 1 wt% and 2 wt% Pt) (see Figure 32).[159] The total Pt amount was kept constant for all experiments.

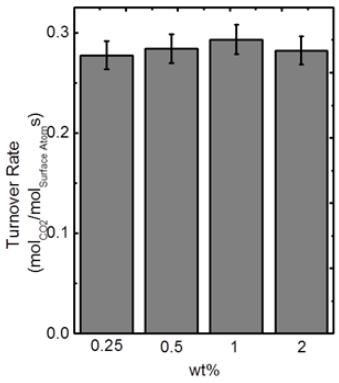

Figure 32: Test for internal mass transfer limitation. The metal loading was varied between 0.25 wt% and 2 wt%. The total Pt content in the experiments was kept constant and TOF values were determined. (Reprinted with the permission of Elsevier, Journal of Catalysis, 2019, 377, 662-672)

For all metal loadings similar TOF values were obtained, which indicates that no internal mass transport limitations were present under given reaction conditions (see Figure 32). In the following a loading of 1 wt% of Pt on Al_2O_3 was chosen.

The tests for heat and mass transfer limitations were all negative, which means that steady state kinetics of CO oxidation with supported Pt NPs can be studied. Furthermore, reaction mechanisms can be postulated and apparent activation energies can be determined.

7.4 Kinetics of CO oxidation depending on the particle size

(Relevant paper II)

Kinetic CO oxidation studies were performed using “surfactant-free” Pt NPs with 1 nm, 2 nm, 3 nm, and 4 nm particle size, which were supported on inert Al_2O_3. In order to determine the intrinsic activities for each particle size, the turnover frequency (TOF) was calculated normalized to the total number of surface atoms. The number of surface atoms was estimated from the average particle size determined from TEM images and assuming a spherical shape and a close-packed crystal structure as an approximation. For determination of kinetic parameters (reaction orders and effective rate constants) partial pressure dependencies for both reactants were performed. The reaction orders were determined fitting the partial pressure dependencies with a power law function and the exponent reflects the reaction order. Another possibility to obtain reaction orders is a double logarithmic plot of the TOF as a function of the partial pressure. However, both possibilities led to the same reaction orders. The activation energies were determined using Arrhenius plots. Therefore, the

reaction temperature was decreased by 10 K in 5 K steps and increased by 10 K in 5 K steps. The reaction rates were determined at different reaction temperatures and the ln(TOF) was plotted against 1/T. From the slope the apparent activation energies were determined. For the O_2 partial pressure dependencies the O_2 partial pressure was varied between 6.8 – 20.3 kPa and a constant CO partial pressure of 0.39 kPa and for the CO partial pressure dependencies the CO partial pressure was varied between 0.29 – 0.45 kPa CO and a constant O_2 partial pressure of 12.2 kPa was applied. The kinetics of CO oxidation depending on the particle size were investigated at three different reaction temperatures. The results are discussed in the following chapters.

7.4.1 CO oxidation at 170°C

CO oxidation was studied at 170°C and partial pressure dependencies are shown in Figure 33.

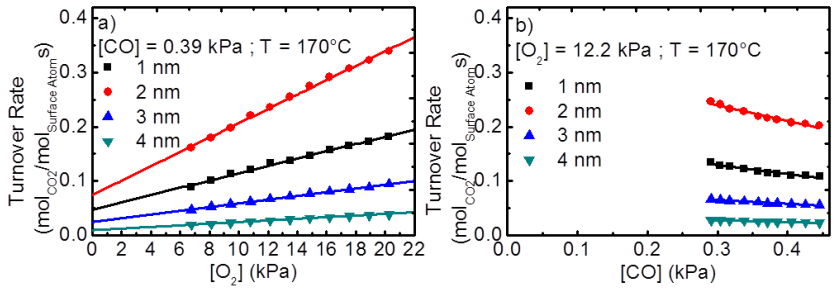

Figure 33: Partial pressure dependences for CO oxidation at 170°C for supported Pt NPs on Al_2O_3 with 1 nm (black), 2 nm (red), 3 nm (blue), and 4 nm (green) particle size. For O_2 partial pressure dependences the partial pressure of O_2 was varied between 6.8 and 20 kPa with a constant CO partial pressure of 0.39 kPa (a). For the CO partial pressure dependence the CO partial pressure was varied in a range of 0.29 to 0.45 kPa and a constant O_2 partial pressure of 12.2 kPa (b). (Reprinted with the permission of Elsevier, Journal of Catalysis, 2019, 377, 662-672)

For all particle sizes the TOF values are proportional to the partial pressure of O_2 and inversely proportional to the CO partial pressure (see Figure 33). Considering that all surface atoms are catalytically active, particles being 2 nm in size exhibit the highest catalytic activity, followed by particles with 1 nm mean particle diameter. Particles with 3 nm and 4 nm are significantly less active. The assumption that NPs under reaction conditions are in the energetically favoured shape (cubo-octahedral shape), particles with 2 nm exhibit a maximum of edge atoms (see chapter 4, Figure 10).[76-78, 160] From surface science studies it is known that O_2 preferentially adsorbs and dissociates on edge atoms.[154] Hence, the effective O_2 activation explains the high activity for particles with 2 nm size.

In the next step reaction orders and apparent activation energies were determined from the partial pressure dependences (see Table 3).

Table 3: Reaction orders for O_2 and CO determined from the partial pressure dependences and apparent activation energies obtained for Pt NPs (1 – 4 nm) at 170°C. (Reprinted and modified with the permission of Elsevier, Journal of Catalysis, 2019, 377, 662-672)

Particle size	Measured Reaction order O_2	Measured Reaction order CO	Apparent activation energy (kJ/mol)
1 nm	0.64 ± 0.05	-0.48 ± 0.05	64.7 ± 1.2
2 nm	0.68 ± 0.05	-0.47 ± 0.05	65.9 ± 1.1
3 nm	0.63 ± 0.05	-0.45 ± 0.05	64.2 ± 1.6
4 nm	0.64 ± 0.05	-0.45 ± 0.05	63.9 ± 2.7

For all particle sizes similar reaction orders for O_2 and CO and similar apparent activation energies were obtained, which indicates that the reaction proceeds in the same kinetic regime independent of the particle size (see Table 3). The negative reaction orders for CO demonstrate that the reaction proceeds via a Langmuir Hinshelwood mechanism with competitive CO and O_2 adsorption with CO as MARI.[125] A reaction mechanism is introduced, which is suitable to explain the observed reaction order for O_2 (see Figure 34).

$$\begin{aligned}
&CO + * \overset{K_{A1}}{\rightleftharpoons} CO^* && (A1)\\
&O_2 + 2^* \overset{K_{A2}}{\rightleftharpoons} 2\,O^* && (A2)\\
&CO^* + O^* \xrightarrow{k_{A3}} CO_2^* + * && (A3)\\
&CO_2^* \xrightarrow{k_{A4}} * + CO_2 && (A4)
\end{aligned}$$

Figure 34: Sequence of elementary steps of CO oxidation on Pt NPs with dissociative O_2 adsorption (mechanism A). (Reprinted with the permission of Elsevier, Journal of Catalysis, 2019, 377, 662-672)

CO chemisorbs on the Pt surface and the formation of CO* is assumed to be quasi-equilibrated (A1). Gaseous molecular O_2 chemisorbs dissociatively, which requires two adjacent free adsorption sites (A2). The rate determing step is the surface reaction of adsorbed CO* and O* to CO_2* (A3). CO_2* than desorbs in the last step (A4). A pseudo steady-state analysis of the sequence of elementary steps and the assumption that CO is the MARI ($K_{A1}[CO] \gg 1$) leads to following rate equation (26):

$$TOF_A = \frac{k_{A3}\sqrt{K_{A2}[O_2]}}{K_1[CO]} \qquad (26)$$

The expected reaction order for O_2 from equation (26) of 0.5 is in close agreement with the observed reaction order of 0.65 ± 0.05. However, equation (26) predicts a reaction order of -1 for CO, which is not in accordance with the observed reaction order of -0.45 ± 0.05. Therefore, another reaction pathway is expected to occur in parallel. In the presence of CO, Pt is known to accumulate carbon and two reaction mechanisms are possible to explain the formation of surface carbon C*.[161-162] The first mechanism is the Boudouard reaction of two adjacent adsorbed CO* to CO_2* and C* (B3).[162-163]

The C* then reacts with adsorbed O_2* to CO_2* (B4) (see Figure 35). The second reaction mechanism is the dissociation of adsorbed CO* to C* and O* and following C* can react with O_2* to CO_2*.[164] The plausibility of both reaction mechanisms was demonstrated with isotopic labelling experiments ($^{18}O_2$) and the latter reaction mechanism was excluded by fitting the partial CO partial pressure dependence with the rate equation of the Boudouard reaction and the rate equation of the CO dissociation.

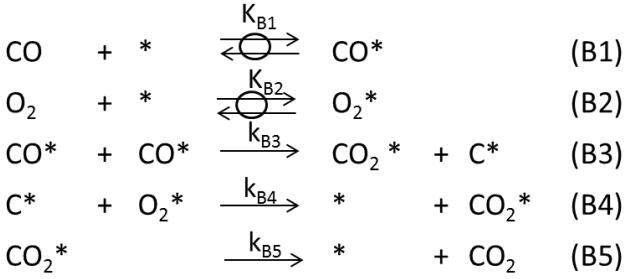

Figure 35: Sequence of elementary steps of CO oxidation on Pt NPs of the Boudouard reaction (mechanism B). (Reprinted with the permission of Elsevier, Journal of Catalysis, 2019, 377, 662-672)

Pseudo steady state analysis of the Boudouard reaction leads to following predicted rate equation (27):

$$TOF_B = \frac{2k_{B3}K_{B1}^2[CO]^2}{(1 + K_{B1}[CO])^2} \tag{27}$$

The measured partial pressure dependencies were fitted with the sum of the rate equation of the Langmuir Hinshelwood mechanism with dissociative O_2 adsorption and the Boudouard reaction and the data fits led to good correlation. Hence, the kinetics of CO oxidation at 170°C can be explained by the combination of mechanism A and B for all particle sizes. From the data fits the rate constants (k_{eff} and k_{B3}) and the contribution of the Boudouard reaction was calculated (see Table 4).

Table 4: Rate constants (k_{eff} and k_{B3}) and the percentage of the contribution of the Boudouard reaction for CO oxidation at 170°C. (Reprinted and modified with the permission of Elsevier, Journal of Catalysis, 2019, 377, 662-672)

Particle size	k_{eff} ($mol_{CO2}/mol_{surface\ Atom}s$)	k_{B3} ($mol_{CO2}/mol_{surface\ Atom}s$)	Ratio of the Boudouard reaction (%)
1 nm	0.0102 ± 0.0015	0.0015 ± 0.0002	2.3
2 nm	0.0165 ± 0.0025	0.0040 ± 0.0006	2.4
3 nm	0.0051 ± 0.0008	0.0031 ± 0.0005	9.2
4 nm	0.0018 ± 0.0003	0.0022 ± 0.0003	18.0

It was found that with increasing particle size the contribution of the Boudouard reaction increased, which leads to the assumption that the Boudouard reaction preferentially proceeds at terrace atoms.

7.4.2 CO oxidation at 200°C

In order to investigate possible changes of the kinetic regime with increasing reaction temperature the same catalysts (1 - 4 nm) were investigated in the same partial pressure regime, but at a reaction temperature of 200°C (see Figure 36).

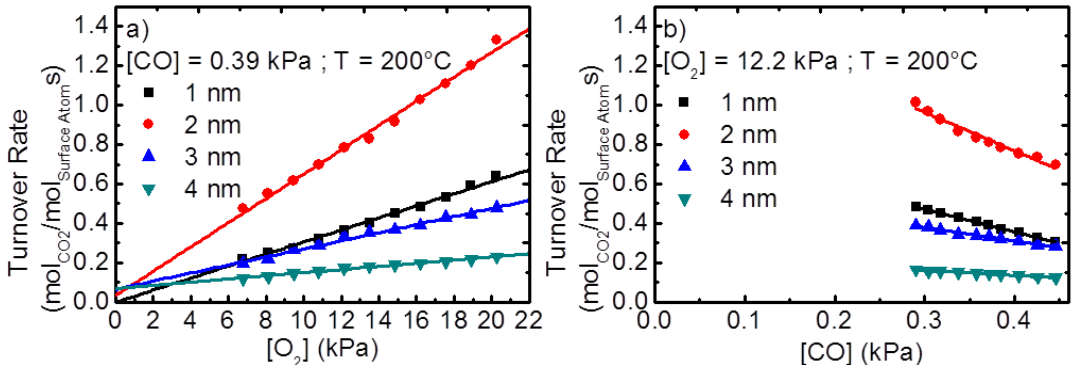

Figure 36: Partial pressure dependences for CO oxidation at 200°C for supported Pt NPs on Al_2O_3 with 1 nm (black), 2 nm (red), 3 nm (blue), and 4 nm (green) particle size. For O_2 partial pressure dependences the partial pressure of O_2 was varied between 6.8 and 20 kPa with a constant CO partial pressure of 0.39 kPa (a). For the CO partial pressure dependence the CO partial pressure was varied in a range of 0.29 to 0.45 kPa and a constant O_2 partial pressure of 12.2 kPa (b). (Reprinted with the permission of Elsevier, Journal of Catalysis, 2019, 377, 662-672)

At 200°C reaction temperature the same particle size dependence for the activity was observed as at 170°C. Again the 2 nm particles exhibit the highest activity and for larger particles (≥ 3 nm) lower TOF values were obtained (see Figure 36). In order to demonstrate possible changes of the kinetic regime the reaction orders and apparent activation energies were determined (see Table 5).

Table 5: Reaction orders for O_2 and CO determined from the partial pressure dependences and apparent activation energies obtained for Pt NPs (1 – 4 nm) at 200°C. (Reprinted and modified with the permission of Elsevier, Journal of Catalysis, 2019, 377, 662-672)

Particle size	Measured Reaction order O_2	Measured Reaction order CO	Apparent activation energy (kJ/mol)
1 nm	1.00 ± 0.05	-1.06 ± 0.05	100.3 ± 4.3
2 nm	0.92 ± 0.05	-0.83 ± 0.05	93.2 ± 1.5
3 nm	0.80 ± 0.05	-0.73 ± 0.05	71.4 ± 2.9
4 nm	0.61 ± 0.05	-0.63 ± 0.05	63.7 ± 2.7

Increasing the reaction temperature leads to a significant change of the reaction orders and apparent activation energies with increasing particle size, indicating that the kinetic regime changes with increasing temperature and furthermore depends on the particle size (see Table 5). The negative reaction orders for CO at 200°C indicate, that the surface is still covered with CO (CO is MARI). Interestingly, for Pt NPs with 1 nm particle size reaction orders of 1 for O_2 and -1 for CO were observed. Reaction orders of 1 for O_2 and -1 for CO are often discussed in the literature and the

following mechanism has been postulated for CO oxidation on Pt surfaces by Langmuir (see Figure 37).[125, 135, 165]

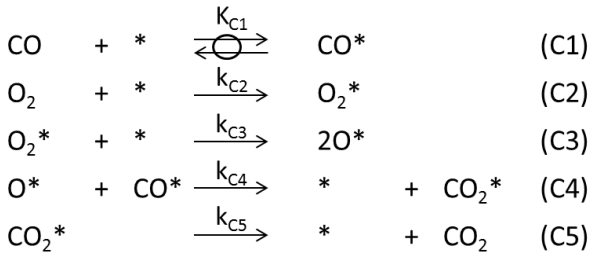

Figure 37: Sequence of elementary steps of CO oxidation on Pt postulated by Langmuir (mechanism C).[135] (Reprinted with the permission of Elsevier, Journal of Catalysis, 2019, 377, 662-672)

The adsorption of CO is assumed to by quasi-equilibrated (C1) and the rate determing step is the irreversible molecular adsorption of O_2 (C2). In a subsequent step the adsorbed O_2* interacts with a free adsorption sites, which leads to dissociation of O_2 (C3). CO_2* is formed by the surface reaction of O* and CO* (C4). Subsequently, CO_2* desorbs from the catalyst surface (C5). This sequence of elementary steps with the assumption that CO is MARI leads to following rate equation (28):

$$TOF_C = \frac{k_{C2}[O_2]}{K_{C1}[CO]} \tag{28}$$

Hence, the here introduced reaction mechanism predicts reaction orders of 1 for O_2 and -1 for CO as observed under the here applied reaction condition for Pt NPs with 1 nm particle size. However, the reaction mechanism predicts that the molecular adsorption of O_2 is the rate determining step, which seem unlikely due to the expectations that the subsequent steps (O_2 dissociation or reaction of O* and CO*) exhibit higher activation barriers. Therefore, another reaction mechanism was proposed by Allian et al. (see Figure 38).[125]

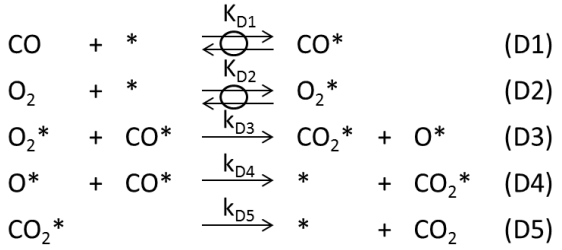

Figure 38: Sequence of elementary steps of CO oxidation on Pt postulated by Allian et al. (mechanism D).[125] (Reprinted with the permission of Elsevier, Journal of Catalysis, 2019, 377, 662-672)

Compared to mechanism C, mechanism D assumes quasi-equilibrated molecular adsorption of CO and O_2 (D1, D2) and the kinetically relevant step is expected to be the irreversible reaction of O_2*

with CO* to CO_2* and O* (D3). In a subsequent step, the formed O* reacts with another adsorbed CO* to CO_2* (D4), which desorbs from the surface (D5). This sequence of elementary steps with CO as MARI leads to following rate equation based on the steady state approximation (29):

$$TOF_D = \frac{2K_{D2}k_{D3}[O_2]}{K_{D1}[CO]} \tag{29}$$

Mechanism D as well as mechanism C predict both a reaction order of 1 for O_2 and -1 for CO. Hence, from kinetics studies mechanism C and D cannot be distinguished. Only the effective rate constants k_{eff} of mechanism C and D vary (mechanism C: $k_{eff} = \frac{k_{C2}}{K_{C1}}$ and mechanism D: $k_{eff} = \frac{2K_{D2}k_{D3}}{K_{D1}}$) and neither spectroscopy nor isotopic labelling experiments can distinguish between mechanism C or D.[125]

With increasing particle size the reaction order for O_2 decreases and the reaction order for CO increases (see Table 5). The shift of the reaction order of O_2 toward 0.5 with increasing particle size implies that dissociative O_2 adsorption (mechanism A) is preferred on large particles and the change of the CO reaction order indicates that the Boudouard reaction (mechanism B) proceeds as a side reaction. From effective rate constants (k_{eff}) the contribution of the Boudouard reaction (k_{B3}) was calculated and it was found that with increasing particle size the percentage of the Boudouard reactions increases (see Table 6). This leads to the assumption that dissociative O_2 adsorption and the Boudouard reaction proceed mainly when a high number of terrace atoms is present.

Table 6: Rate constants (k_{eff} and k_{B3}) and the percentage of the contribution of the Boudouard reaction for CO oxidation at 200°C. (Reprinted and modified with the permission of Elsevier, Journal of Catalysis, 2019, 377, 662-672)

Particle size	k_{eff} ($mol_{CO2}/mol_{surface\ Atom}s$)	k_{B3} ($mol_{CO2}/mol_{surface\ Atom}s$)	Ratio of the Boudouard reaction (%)
1 nm	0.0105 ± 0.0016	-	0.0
2 nm	0.0277 ± 0.0042	0.0017 ± 0.0003	0.5
3 nm	0.0164 ± 0.0025	0.0140 ± 0.0021	8.5
4 nm	0.0127 ± 0.0019	0.0120 ± 0.0018	14.0

The change of the reaction mechanism is further supported by the significant decrease of the activation energy with increasing particle size (see Table 5). From DFT calculations on Pt NPs and on single crystals it is known that the binding energy of CO increases and the activation barrier of the reaction with CO* and O_2* decreases with decreasing coordination number of Pt surface atoms.[125] Hence, the apparent activation energy is expected to increase when a high number of low coordinated surface atoms are present. This is in accordance with the decreasing activation energy with increasing particle size (see Table 5).

The results show that the reaction mechanism for CO oxidation changes with increasing particle size at 200°C. On particles with a high ratio of low coordinated surface atoms (1 nm and 2 nm) mainly mechanism C or D was identified, whereas with increasing number of terrace atoms the dissociative O_2 adsorption and the Boudouard reaction as a side reaction were discussed.

7.4.3 CO oxidation at higher temperature

CO oxidation with Pt NPs in a size range of 1 – 4 nm demonstrates that the reaction mechanism depends on the reaction temperature and on the particle size. Therefore, the reaction temperature was increased for particles > 1 nm. A reaction temperature of 210°C was used for Pt NPs with 2 nm size and for larger Pt NPs the temperature was further increased to 235°C for 3 nm and 250°C for 4 nm Pt NPs (see Figure 39).

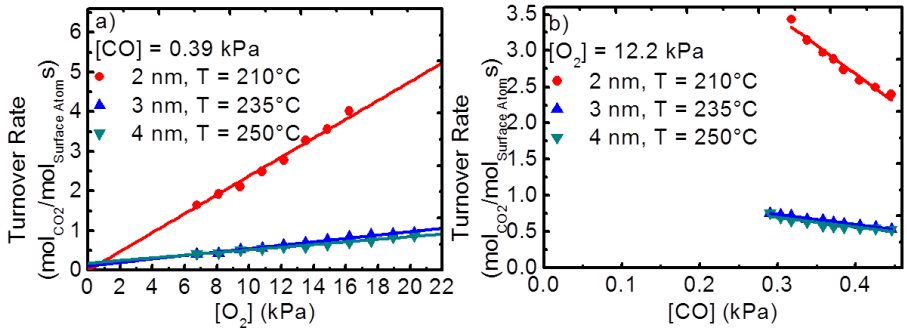

Figure 39: Partial pressure dependences for CO oxidation for supported Pt NPs on Al2O3 with a particle size of 2 nm (red) at 210°C, 3 nm (blue) at 235°C, and 4 nm (green) at 250°C. For O2 partial pressure dependences the partial pressure of O2 was varied between 6.8 and 20 kPa with a constant CO partial pressure of 0.39 kPa (a). For the CO partial pressure dependence the CO partial pressure was varied in a range of 0.29 to 0.45 kPa and a constant O2 partial pressure of 12.2 kPa (b). (Reprinted with the permission of Elsevier, Journal of Catalysis, 2019, 377, 662-672)

From the partial pressure dependences reaction orders for O_2 and CO and apparent activation energies were determined (see Table 7).

Table 7: Reaction orders for O_2 and CO determined from the partial pressure dependences and apparent activation energies obtained for Pt NPs with 2 nm at 210°C, 3 nm at 235°C, and 4 nm at 250°C. (Reprinted and modified with the permission of Elsevier, Journal of Catalysis, 2019, 377, 662-672)

Particle size	Temperature [°C]	Measured Reaction order O_2	Measured Reaction order CO	Apparent activation energy (kJ/mol)
2 nm	210	1.03 ± 0.05	-1.05 ± 0.05	103.6 ± 3.5
3 nm	235	0.84 ± 0.05	-0.78 ± 0.05	80.7 ± 2.8
4 nm	250	0.67 ± 0.05	-0.72 ± 0.05	80.2 ± 2.7

The reaction orders of 1 for O_2 and -1 for CO obtained for Pt NPs with 2 nm size at 210°C demonstrates that a quite minor increase of the reaction temperature by 10 K shifts the kinetics into

the kinetic regime that has been observed for Pt NPs with 1 nm size at 200°C (mechanism C or D). The similar activation energy of Pt NPs with 2 nm (compared to Pt NPs with 1 nm at 200°C) indicates that the adsorption energies and the reaction barriers are similar. Furthermore, a contribution of the Boudouard reaction is completely suppressed at 210°C (see Table 8), whereas at 200°C still a minor contribution of the Boudouard reaction was observed (see Table 6).

Table 8: Rate constants (k_{eff} and k_{B3}) and the percentage of the contribution of the Boudouard reaction for CO oxidation at 210°C for 2 nm, 235°C for 3 nm, and 250°C for 4 nm. (Reprinted and modified with the permission of Elsevier, Journal of Catalysis, 2019, 377, 662-672)

Particle size	k_{eff} ($mol_{CO2}/mol_{surface\ Atom}s$)	k_{B3} ($mol_{CO2}/mol_{surface\ Atom}s$)	Ratio of the Boudouard reaction (%)
2 nm	0.0760 ± 0.0114	-	0.0
3 nm	0.0300 ± 0.0046	0.0028 ± 0.0008	2.5
4 nm	0.0417 ± 0.0060	0.0210 ± 0.0038	8.0

The reaction of two adjacent CO* molecules was discussed to proceed mainly on terrace atoms and the temperature increase of 10 K shifts the ratio of adsorbed CO towards more CO bound to low coordinated surface atoms. Hence, CO oxidation over Pt NPs being 2 nm in size proceeds mainly on edge and corner atoms, where mechanism C or D are discussed to be favoured. For Pt NPs with 3 nm and 4 nm a further temperature increase up to 250°C shows no significant differences of the reaction orders or apparent activation energies compared to the kinetic parameters at 200°C (see Table 5 and 7). Due to the high number of terrace atoms on large particles the kinetics are mainly determined by dissociative O_2 adsorption and the Boudouard reaction, even at higher reaction temperatures.

The micokinetic study with "surfactant-free" Pt NPs supported on Al_2O_3 indicates that the reaction mechanism of CO oxidation is rather complex and depends on the particle size as well as on the reaction temperature. Only for small particles (≤ 2 nm) a distinct kinetic regime (mechanism C or D) was identified at reaction temperature ≥ 200°C. With increasing particle size at least two different reaction mechanisms (mechanism A and B) are discussed to proceed in parallel.

In order to further tune the catalytic performance of heterogeneous catalysis the following three factors can be varied:

i) Particle size
ii) Metal support interactions
iii) Bimetallic NPs

The above discussed results indicate that the catalytic properties of CO oxidation can be tuned by controlling the particle size. The here applied synthesis route of colloidal NPs allows also to

investigate the influence of metal-support interactions and bimetallic NPs on the catalytic performance of CO oxidation. The same Pt NPs (1 - 4 nm) were deposited onto reducible support materials (Fe_3O_4 in this case), which may interact with the NPs and strong metal-support interactions (SMSI) can be studied depending on the particle size and be compared to CO oxidation on inert support materials under identic reaction conditions (reaction temperature, partial pressures etc.). Furthermore, bimetallic Fe-Pt NPs are used as catalysts in CO oxidation in order to investigate the influence of bimetallic NPs.

8. Strong metal-support interactions

The term strong metal-support interactions (SMSI) was first defined by Tauster in the year 1978.[166] It was found that the properties of H_2 and CO chemisorption decreased drastically when supported precious metal NPs on TiO_2 were reduced at high temperatures. The reason for the decreased chemisorption capacity is the formation of an oxide layer due to migration of TiO_x species at high temperature which cover the active metal component completely or partially.[166-169] Consequently, the number of active sites on the catalyst is decreased and the activity of the catalyst is affected. Later it was found that the catalytic activity can be increased due to a SMSI effect, which is related to special adsorption sites, which are generated due to the formation of the oxide layer on the NP.[170-172] SMSI effects are not limited to precious metal NPs on TiO_2, but are found for other reducible metal oxides (Fe_3O_4, CeO_2, Nb_2O_5 etc.).[173-175]

Especially Pt NPs supported on iron oxide have gained interest due to CO oxidation activity at low reaction temperature.[176-179] As discussed in chapter 7.1 CO oxidation on Pt surfaces below 170°C is nearly inactive because of the poisoning effects of CO, which prevents adsorption and dissociation of O_2. It was found that oxygen from the iron oxide can be activated and the reaction proceeds via a Mars van Krevelen mechanism.[180-182] However, before the influence of possible SMSI effects with supported Pt NPs on Fe_3O_4 are discussed regarding particle size and the influence of the kinetic performance for CO oxidation, the kinetic activity of pure Fe_3O_4 is discussed.

8.1 CO oxidation with pure Fe_3O_4

(Relevant paper III)

There are some indications in the literature that iron oxide might be catalytically active for CO oxidation.[183-187] Pure Fe_3O_4 was used as a catalyst at a reaction temperature of 200°C under strict kinetically controlled conditions and it was found that iron oxide is able to oxidize CO to CO_2. The catalytic performance of Fe_3O_4 was determined under oxygen rich conditions and after reductive pre-treatment with 5% H_2 at 200°C. Since Fe_3O_4 is a reducible metal oxide, the oxidation state of Fe was determined with X-ray photoelectron spectroscopy (XPS) after exposure to reaction conditions with and without reductive pre-treatment. It was found that Fe was mainly in the oxidation state +III (Fe_2O_3) under oxidative reaction conditions and after reduction and exposure to reaction conditions Fe was in the oxidation state +II (FeO). In the following, oxidized iron oxide will be referred to Fe_2O_3 and reduced iron oxide to FeO. For kinetic investigations the intrinsic activity was determined, normalizing the activity to the total number of Fe surface atoms and partial pressure dependences for O_2 and CO were performed (see Figure 40).

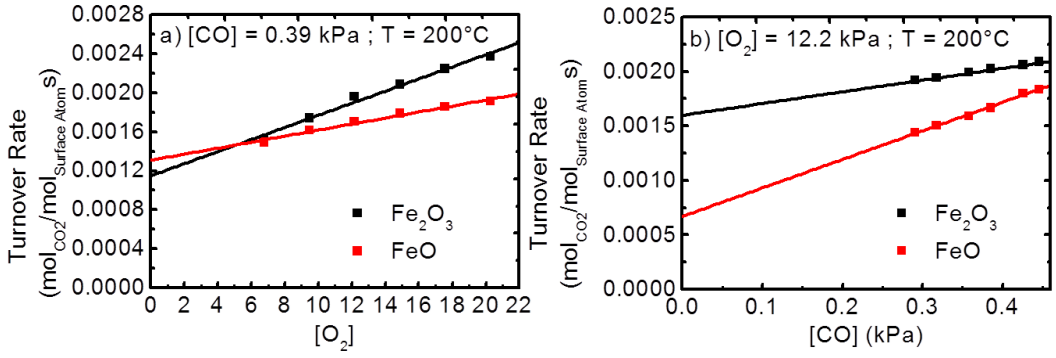

Figure 40: Partial pressure dependences for CO oxidation with Fe_3O_4 as catalyst with (FeO, red) and without (Fe_2O_3, black) reductive pre-treatment. For O_2 partial pressure dependences the partial pressure of O_2 was varied between 6.8 and 20 kPa with a constant CO partial pressure of 0.39 kPa (a). For the CO partial pressure dependence the CO partial pressure was varied in a range of 0.29 to 0.45 kPa and a constant O_2 partial pressure of 12.2 kPa (b). The reaction temperature was 200°C.

From the partial pressure dependences the reaction orders for O_2 and CO were determined and an Arrhenius plot was used to obtain apparent activation energies (see Table 9).

Table 9: Reaction orders for O_2 and CO determined from the partial pressure dependences and apparent activation energies obtained for Fe_3O_4 with and without reductive pre-treatment and a reaction temperature at 200°C.

	Measured Reaction order O_2	Measured Reaction order CO	Apparent activation energy (KJ/mol)
Fe_2O_3	0.40 ± 0.01	0.19 ± 0.03	46.7 ± 1.2
FeO	0.23 ± 0.01	0.59 ± 0.03	30.7 ± 3.2

The differences in the TOF values, the reaction orders, and apparent activations energies for reduced and oxidized iron oxide indicate that the reaction mechanism of Fe_2O_3 and FeO is not the same (see Figure 40 and Table 9). However, the uneven reaction orders for O_2 and CO demonstrate that not a single reaction mechanism is able to explain the kinetic properties of Fe_2O_3 or FeO. None of the typically reported reactions mechanism (Eley-Rideal mechanism, Mars van Krevelen mechanism, and a competitive Langmuir Hinshelwood mechanism) is in accordance with the observed reaction orders under the here applied oxygen rich reaction conditions.[142, 188]

In order to test for a possible reaction pathway with contribution of lattice oxygen (Mars van Krevelen mechanism) CO oxidation was performed in absence of oxygen and the catalyst was pre-treated with isotopic labelled $^{18}O_2$. Residues of $^{18}O_2$ were removed by flushing the catalyst with He before exposure to CO. It was found that Fe_2O_3 and FeO are active in the absence of oxygen and the formation of isotopic labelled CO_2 demonstrates the ability of iron oxide to store or exchange oxygen in the lattice (see Figure 41).

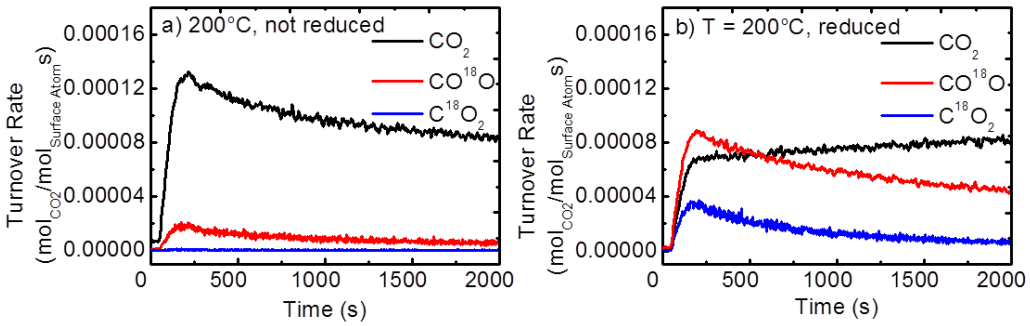

Figure 41: Turnover rates of CO oxidation with pure iron oxide as catalyst in absence of gaseous O_2. Before catalysis the catalyst was pre-treated with $^{18}O_2$. The reaction was performed at 200°C without (Fe_2O_3, a) and with (FeO, b) reductive pre-treatment.

Hence, one possible reaction pathway on iron oxide is a Mars van Krevelen mechanism with lattice oxygen as active component.

8.2 Kinetics of CO oxidation of Platinum nanoparticles supported on Fe_3O_4

(Relevant paper III)

8.2.1 Oxidative reaction conditions

"Surfactant-free" Pt NP dispersion with 1 nm, 2 nm, 3 nm, and 4 nm particle size were prepared and deposited onto Fe_3O_4. The supported NPs were characterized with TEM and it was shown that the NPs were dispersed over the support material and no agglomeration was found after heat treatment. The catalysts were used directly in CO oxidation without reductive pre-treatment and the TOF values were compared to the same particles on an inert support material (see Chapter 7.4.2).[189]

Table 10: TOF values of supported Pt NPs on Fe_3O_4 compared to the same particles supported on Al_2O_3 normalized to the number of Pt surface atoms. Furthermore, TOF values were calculated normalized to the number of Pt atoms at the interface between NP and support (Fe_3O_4 and Al_2O_3). CO oxidation was performed at 200°C and a partial pressure of 0.39 kPa CO and 12.2 kPa O_2.

Particle size	TOF Pt-Fe_2O_3 Total number of surface atoms [$mol_{CO2}/mol_{Surface\ Atom}$ s]	TOF Pt-Fe_2O_3 Atoms at the interface between NP and support [$mol_{CO2}/mol_{Interface\ Atom}$ s]	TOF Pt-Al_2O_3 Total number of surface atoms [$mol_{CO2}/mol_{Surface\ Atom}$ s][189]	TOF Pt-Al_2O_3 Atoms at the interface between NP and support [$mol_{CO2}/mol_{Interface\ Atom}$ s]
1 nm	0.15	0.76	0.36	1.84
2 nm	0.21	0.77	0.79	2.85
3 nm	0.07	0.82	0.34	3.64
4 nm	0.08	1.09	0.17	2.39

Compared to Pt NPs on Al_2O_3, the TOF of Pt NPs on Fe_2O_3 decreased significantly for all particle sizes (see Table 10). This indicates that the support material strongly alters the catalytic performance under given reaction conditions (see Table 10). In order to exclude that Fe_2O_3 is the sole active

species, the reaction rates were normalized to the total catalyst mass and it was found that the catalyst with the precious metal exhibits a up to 20 times higher reaction rates. This indicates that the precious metal increases the catalytic performance. For precious metal NPs on a reducible support material the presence of active sites is often observed, which are generated due to the formation of strong metal-support interactions at the interface of the NP and the support material.[188, 190] In order to test for the presence of these active sites for Pt-Fe_2O_3, reaction rates were normalized to the number of Pt atoms at the interface and it was found that for all small particle sizes (≤ 2nm) similar activities were obtained for Pt-Fe_2O_3, but not for Pt-Al_2O_3 (normalized to the number of Pt atoms at the interface, see Table 10). With increasing particle size (≥ 3 nm) the TOF increased compared to the small NPs. Consequently, the reaction may preferentially proceed at the interface between the NP and Fe_2O_3 for small NPs (1 nm and 2 nm) and with increasing particle size (3 nm and 4 nm) a different or an additional reaction pathway has to be taken into account.

In the next steps partial pressure dependencies for O_2 and CO were performed at a reaction temperature of 200°C. The reaction rates were normalized to the number of Pt atoms at the interface between particle and support (see Figure 42).

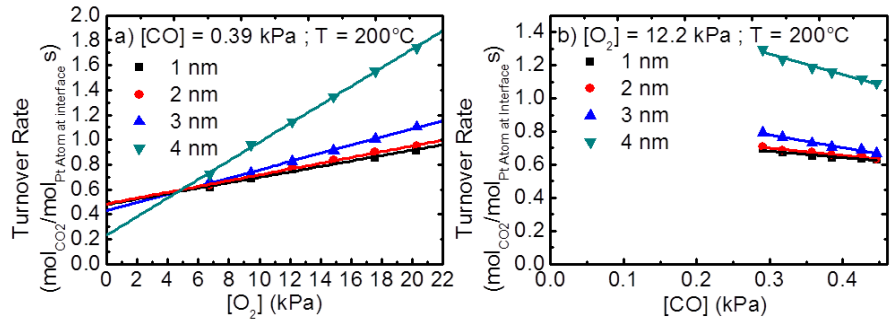

Figure 42: Partial pressure dependences for CO oxidation at 200°C for supported Pt NPs on Fe_2O_3 with 1 nm (black), 2 nm (red), 3 nm (blue), and 4 nm (green) particle size without reductive pre-treatment. For O_2 partial pressure dependences the partial pressure of O_2 was varied between 6.8 and 20 kPa with a constant CO partial pressure of 0.39 kPa (a). For the CO partial pressure dependence the CO partial pressure was varied in a range of 0.29 to 0.45 kPa and a constant O_2 partial pressure of 12.2 kPa (b).

The TOF values for catalysts (1 – 4 nm) are proportional to the O_2 partial pressure and inversely proportional to the CO partial pressure (see Figure 42). Particles with a size ≤ 2 nm exhibit similar TOF values over the entire partial pressure range for the O_2 as well as for the CO partial pressure dependency. However, large particles (≥ 3 nm nm) have higher TOF values (especially for Pt NP with 4 nm size) with increasing O_2 partial pressure. This indicates that a similar reaction mechanism takes place on Pt NPs ≤ 2 nm and the reaction seems to be favoured to proceed at the interface of NP and support. Whereas, this conclusion cannot be drawn for Pt NPs with ≥ 3 nm size. In order to

demonstrate a change of the kinetic regime reaction orders and apparent activation energies were determined (see Table 11).

Table 11: Reaction orders for O_2 and CO determined from the partial pressure dependences and apparent activation energies obtained for Pt NPs on Fe_2O_3 (1 – 4 nm) at 200°C without reductive pre-treatment.

Particle size	Reaction order O_2	Reaction order CO	Apparent activation energy (KJ/mol)
1 nm	0.36 ± 0.01	-0.21 ± 0.03	64.3 ± 1.9
2 nm	0.37 ± 0.01	-0.24 ± 0.02	64.2 ± 2.6
3 nm	0.45 ± 0.03	-0.38 ± 0.02	67.5 ± 5.9
4 nm	0.78 ± 0.02	-0.51 ± 0.02	84.2 ± 3.2

Small NPs ≤ 2 nm exhibit similar reaction orders for O_2 and CO and apparent activation energies, indicating that the reaction proceeds in the same kinetic regime. For Pt NP ≥ 3 nm in size the reaction order for O_2 and the activation energy increases and the reaction order for CO decreases (see Table 11). However, comparison of the reaction orders and activation energies obtained for Pt NPs on Fe_2O_3 with Pt NPs on Al_2O_3 demonstrates that the kinetic parameters vary significantly (see Table 5 and 11). For small Pt NPs on Al_2O_3 a Langmuir Hinshelwood mechanism with molecular O_2 adsorption was found to correctly reflect the kinetics (reaction orders of 1 for O_2 and -1 for CO).[189] Hence, neither mechanism C nor D can be the most relevant mechanism on Pt NPs on Fe_2O_3. The above discussed reaction pathway at the interface of NP and support suggest that the reaction may proceed via a Mars van Krevelen mechanism with lattice oxygen (see Figure 43).

$$
\begin{aligned}
&CO + * \xrightleftharpoons{K_{E1}} CO^* && (E1)\\
&CO^* + (O) \xrightarrow{k_{E2}} CO_2^* + (\,) && (E2)\\
&CO_2^* \xrightarrow{k_{E3}} * + CO_2 && (E3)\\
&\tfrac{1}{2}O_2 + (\,) \xrightarrow{k_{E4}} (O) && (E4)
\end{aligned}
$$

Figure 43: Sequence of elementary steps of CO oxidation of a Mars van Krevelen mechanism (mechanism E). (O) represents a lattice oxygen atom and ( ) an oxygen vacancy.

The adsorption of CO on the Pt surface is assumed to be quasi-equilibrated (E1). A chemisorbed CO* near the interface to Fe_2O_3 reacts with a lattice oxygen (O) to form CO_2* and an oxygen vacancy is generated (E2). Following CO_2* desorbs (E3) and the oxygen vacancy is regenerated with gaseous oxygen (E4). The deviation of the rate equation assuming quasi steady state leads to following rate equation for a Mars van Krevelen mechanism (30):

$$TOF_E = \frac{k_{E2} K_{E1} [CO]}{(1 + K_{E1}[CO])} \quad (30)$$

The rate equation predicts a reaction order of 0 for O_2, but for all particle sizes a reaction order for O_2 of > 0 was observed. Hence, another reaction mechanism is supposed to occur in parallel. For all particle sizes a slightly negative reaction order was obtained, indicating that CO is the MARI under reaction conditions, which leads to the assumption that a competitive Langmuir Hinshelwood mechanism with chemisorbed CO and O_2 might take place in parallel. With increasing particle size the reaction orders shift to the reaction orders expected from a Langmuir Hinshelwood mechanism (1 for O_2 and -1 for CO). This can be explained by the fact that the surface is proportional to d^2. Consequently, the relevance of the surface reaction on Pt of CO* with O_2* increases as the particle size increases.

This leads to the assumption that on the Pt surface a Langmuir Hinshelwood mechanism proceeds on the Pt surface and at the interface between NP and support a Mars van Krevelen mechanism. The relevance of both mechanisms was validated, fitting the partial pressure dependencies with the sum of the rate equation of a Langmuir Hinshelwood mechanism and the Mars van Krevelen mechanism and the assumption that CO is the MARI (see equation (31)).

$$TOF = k_{eff} \frac{[O_2]}{[CO]} + k_{E2} \quad (31)$$

From the data fits and the rate constants the contribution of each mechanism was determined. It can indeed be seen that with increasing particle size the contribution of a Langmuir Hinshelwood mechanism increased (see Table 12).

Table 12: Rate constants (k_{eff} and k_{E3}) and the percentage of the contribution of the Langmuir Hinshelwood mechanism and the Mars van Krevelen mechanism for CO oxidation with Pt NP on Fe_2O_3 at 200°C.

Particle size	k_{eff} ($mol_{CO2}/mol_{surface\ Atom}s$)	K_{E2} ($mol_{CO2}/mol_{surface\ Atom}s$)	Ratio of the Langmuir Hinshelwood mechanism (C or D)	Ratio of the Mars van Krevelen mechanism (E)
1 nm	0.0085 ± 0.0001	0.4800 ± 0.0072	35%	65%
2 nm	0.0091 ± 0.0001	0.4855 ± 0.0073	37%	63%
3 nm	0.0128 ± 0.0002	0.4294 ± 0.0067	48%	52%
4 nm	0.0271 ± 0.0004	0.2523 ± 0.0041	78%	22%

8.2.2 Reductive pre-treatment

The same kinetic investigations were performed after the catalysts were reduced for 16 h with 5% H_2 at 200°C (see Figure 44).

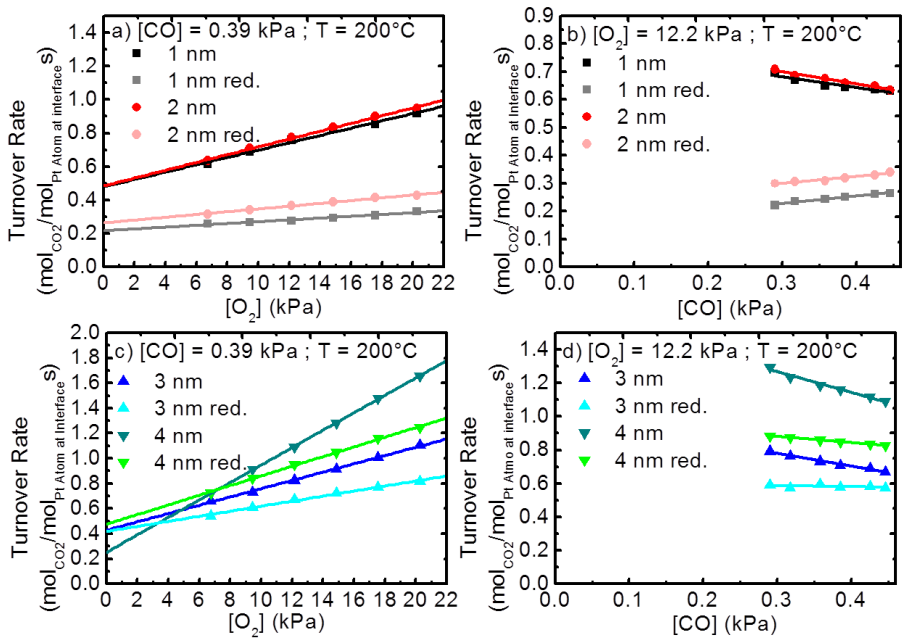

Figure 44: Partial pressure dependences for CO oxidation at 200°C for supported Pt NPs on FeO with 1 nm (black) and 2 nm (red) particle size (a, b) after reductive pre-treatment (1 nm (grey) and 2 nm (light red)) compared to catalysts without reductive pre-treatment. Pt NP on Fe_3O_4 with 3 nm (blue) and 4 nm (green) particle size (c,d) after reductive pre-treatment (3 nm (light blue) and 4 nm (light green) compared to catalysts without reductive pre-treatment under identical reaction conditions (200°C).

After reduction of the supported Pt NPs on FeO the catalytic activity decreases significantly for all particle sizes (see Figure 44). Reaction orders and activation energies were determined in order to discuss possible changes of the kinetic regime (see Table 13).

Table 13: Reaction orders for O_2 and CO determined from the partial pressure dependences and apparent activation energies obtained for Pt NPs on FeO (1 – 4 nm) at 200°C with reductive pre-treatment (5% H_2 for 16 h at 200°C).

Particle size	Reaction order O_2	Reaction order CO	Apparent activation energy (KJ/mol)
1 nm	0.23 ± 0.03	0.41 ± 0.02	27.7 ± 2.4
2 nm	0.28 ± 0.01	0.28 ± 0.04	33.0 ± 2.9
3 nm	0.37 ± 0.01	0.00 ± 0.02	48.5 ± 2.3
4 nm	0.50 ± 0.02	-0.16 ± 0.01	69.5 ± 3.7

The reaction orders for O_2 and the apparent activation energies decrease significantly for all particle sizes after reduction of the catalyst (see Table 13). The reaction order for CO increased and for 1 nm and 2 nm particles positive reaction orders were obtained. Negative reaction orders for CO are observed when the Pt surface is covered under reaction conditions with CO (CO is MARI).[125, 142] Hence, after reductive pre-treatment CO seems to be no MARI any more. From the data fits with the rate equation of the combination of the Langmuir Hinshelwood mechanism and the Mars van Krevelen mechanism the contribution of each mechanism was calculated (see Table 14) and it was

found that for all particle sizes the contribution of the Langmuir Hinshelwood mechanism decreased significantly (see Table 12 and 14).

Table 14: Rate constants (k_{eff} and k_{E3}) and the percentage of the contribution of the Langmuir Hinshelwood mechanism and the Mars van Krevelen mechanism for CO oxidation with Pt NP on FeO at 200°C after reductive pre-treatment (5% H_2 at 200°C for 16 h).

Particle size	k_{eff} ($mol_{CO2}/mol_{surface\ Atom}s$)	K_{E2} ($mol_{CO2}/mol_{surface\ Atom}s$)	Ratio of the Langmuir Hinshelwood mechanism (C or D)	Ratio of the Mars van Krevelen mechanism (E)
1 nm	0.0021 ± 0.0001	0.2160 ± 0.0124	24%	76%
2 nm	0.0032 ± 0.0001	0.2635 ± 0.0195	27%	73%
3 nm	0.0078 ± 0.0001	0.4181 ± 0.0167	36%	64%
4 nm	0.0150 ± 0.0002	0.4760 ± 0.0174	49%	51%

This is in accordance with the change of the reaction orders and the apparent activation energies (see Table 13). The decrease of the activity might be related further to a partial encapsulation of the NPs, since FeO is known to favour the formation of a FeO layer on precious NPs.[173, 180] The results indicate that the catalytic performance of Pt NPs supported on iron oxide depends on the formation of metal support interaction. Compared to Pt NPs on inert support material the reaction kinetics change drastically and it was found that on small NPs (≤ 2 nm) the kinetics are mainly determined by a Mars van Krevelen mechanism at the interface between NP and support. With increasing surface of the NPs a Langmuir Hinshelwood between CO* and O_2* is favoured.

After demonstration of the influence of the particle size and metal-support interaction on the kinetics of CO oxidation, finally the effect of bimetallic NPs is discussed.

8.3 Influence of bimetallic Fe-Pt nanoparticles

(Relevant paper III)

Bimetallic Fe-Pt NPs were used in order to explore, whether a similar effect on the nanoscale between Pt and FeO inside a particle might occur. These particles were supported onto inert Al_2O_3 to prevent a further interaction of the NPs with the support material. The size of the bimetallic NPs was determined to be between 3 and 4 nm.[191]

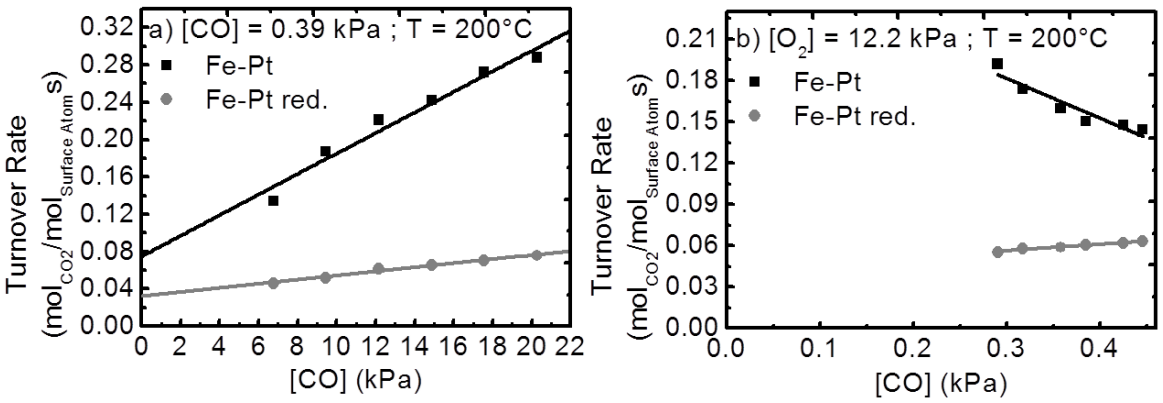

Figure 45: Partial pressure dependences for CO oxidation at 200°C for supported bimetallic $FePt_3$ NPs on Al_2O_3 with (grey) and without (black) reductive pre-treatment. The TOF values were calculated assuming that only Pt atoms are present at the surface. For O_2 partial pressure dependences the partial pressure of O_2 was varied between 6.8 and 20 kPa with a constant CO partial pressure of 0.39 kPa (a). For the CO partial pressure dependence the CO partial pressure was varied in a range of 0.29 to 0.45 kPa and a constant O_2 partial pressure of 12.2 kPa (b) at a reaction temperature of 200°C.

In order to determine the intrinsic activity, the TOF value was determined (see Figure 45). However, under reaction conditions the surface composition of the bimetallic NP is not known. In the literature it was found that under CO and/or O_2 rich conditions a Pt rich surface is generated.[192] Therefore, the TOF values were determined assuming that only Pt atoms are present on the particle surface. From the partial pressure dependencies the reaction orders and from an Arrhenius plot the apparent activation energies were calculated. It was found that the TOF values and the kinetic parameters are in good agreement with the monometallic Pt NPs on Al_2O_3 of similar particle size (see Figure 36 and Figure 45, see Table 5 and 15), indicating that the presence of Fe in the bimetallic NPs does not influence the reaction mechanism and the catalytic activity.

Table 15: Reaction orders for O_2 and CO determined from the partial pressure dependences and apparent activation energies obtained for bimetallic Fe-Pt NPs on Al_2O_3 at 200°C with reductive pre-treatment (5% H_2 for 16 h at 200°C) and without reductive pre-treatment.

	Measured Reaction order O_2	Measured Reaction order CO	Apparent activation energy (KJ/mol)
Fe-Pt Not reduced	0.70 ± 0.04	-0.67 ± 0.05	66.7 ± 5.2
Fe-Pt Reduced	0.45 ± 0.02	0.28 ± 0.03	35.7 ± 2.3

After reductive pre-treatment of the bimetallic NPs the TOF value (normalized to the number of Pt surface atoms) decreases as well as the reaction orders for O_2 and the activation energy (see Figure 45 and Table 15). The reaction order for CO changed from negative reaction orders (CO is MARI) to positive reaction orders. This indicates that the surface of the bimetallic NPs after reduction is no longer covered with CO, which was confirmed with diffuse reflectance infrared fourier transform

spectroscopy (DRIFTS). The kinetic parameters after reduction are similar to pure FeO, which implies that mainly Fe is located at the surface due to surface segregation. The presence of Fe under reaction condition can be explained with the strong Fe-O bond and with the lower surface energy of iron oxide.[193] As a result, a similar dentrimental SMSI effect on the nanoscale was observed for bimetallic Fe-Pt NPs compared to monometallic Pt NPs on iron oxide.

9. Conclusion

The three factors of NP catalyst, which can actively influence the catalytic performance of heterogeneously catalysed reactions are i) the particle size ii) metal support interactions and iii) bimetallic NPs. In the present work a synthesis approach was applied that allows independent control over particle size, support material, and composition. The synthesis of "surfactant-free" Pt NPs bears the advantages that no strong binding ligands or polymers are necessary to stabilize the colloidal NPs. In this study, the synthesis route was optimized with regard to tune the particle size. It was found that the presence of chloride from the metal precursor and from the precipitation step (HCl) favour dissolution of the NPs to Pt ions. The NPs were exposed to other anions and especially bromide was found to enhance the leaching of the NPs. A possible subsequent step after leaching and formation of soluble Pt ions is Ostwald ripening, which leads to particle growth. Using a reducing atmosphere in alkaline EG at a reaction temperature of 150°C the reduction of the soluble Pt ions is favoured, which leads to a particle size growth. Compared to chloride the presence of bromide enhances the formation of Pt ions and therefore the particle growth with bromide containing precursors is faster compared to chloride containing precursors. In combination with previously gained knowledge about the surface chemistry of "surfactant-free" Pt NPs and the influence of the Pt-OH^- ratio to determine the particle size, a concept was developed to tune the particle size by variation of the following three factors:

i) Variation of the OH^- concentration during the synthesis in EG
ii) The use of different Pt precursors (H_2PtCl_6, H_2PtBr_6, and $Pt(acac)_2$)
iii) Extending the reaction temperature (Ostwald ripening)

The synthesis concept leads to Pt NPs within a size range of 1 – 4 nm, which represents the range where the ratio of low to high coordinated surface atoms changes most strongly. These NPs were further supported onto Al_2O_3 and used as heterogeneous catalysts in CO oxidation as a model reaction. The structure sensitivity of CO oxidation is controversially discussed in the literature. Three different reaction regimes (170°C, 200°C, >210°C) were investigated under strict kinetic control and it was found that the catalytic performance (activity and reaction mechanism) depends strongly on the reaction temperature as well as on the particle size. A high number of edge atoms (2 nm particle size) were found to favour O_2 dissociation, which leads to the highest catalytic performance. At a reaction temperature of 170°C a reaction mechanism with dissociative O_2 adsorption and the Boudouard reaction of two adjacent CO* to C* and CO_2* was postulated to occur for all particle sizes, whereas with increasing reaction temperature (>200°C) the reaction mechanism changes for small Pt NPs (≤ 2 nm). Reaction orders of 1 for O_2 and -1 for CO indicate molecular O_2 adsorption and the reaction

of CO* and O_2* to CO_2* and O* was identified as the rate determining step. On large particles the number of terrace atoms determines the kinetic behaviour and dissociative O_2 adsorption and the Boudouard reaction was found to occur preferentially on terrace atoms.

In order to further improve the mechanistic understanding, the NPs were supported onto reducible iron oxide and it was found that the catalytic performance is strongly influenced when using transition metal oxides. Two different reaction pathways were identified to proceed on different active sites. A Mars van Krevelen mechanism between CO* adsorbed on Pt and lattice oxygen takes place at the interface between NP and support and on the Pt surface the Langmuir Hinshelwood mechanism between CO* and O_2* was discussed. With increasing particle size (and the related increase of the Pt surface) the contribution of the Langmuir Hinshelwood mechanism increases. After reductive pre-treatment of the catalysts the active Pt surface decreases due to partial encapsulation with FeO and the Mars van Krevelen mechanism becomes favoured after reduction. However, a similar effect is observed when using bimetallic Fe-Pt NPs on inert Al_2O_3. Hence, the here presented kinetic study of CO oxidation shows that the catalytic performance can be influenced by changing the particle size, the support material, and mixing the active component with another transition metal.

10. Outlook

The here presented work demonstrates that the synthesis concept of supported colloidal "surfactant-free" Pt NPs allows to investigate SMSI effects systematically. As a follow up, it would be interesting to investigate the catalytic behaviour and particle size effects in CO oxidation for Pt NPs supported on different reducible support material (e.g. TiO_2, CeO_2, SnO). For TiO_2 SMSI effects are widely discussed in the literature and therefore first kinetic experiments were performed for Pt NP (1 – 3 nm) supported on TiO_2 (see Figure 46).

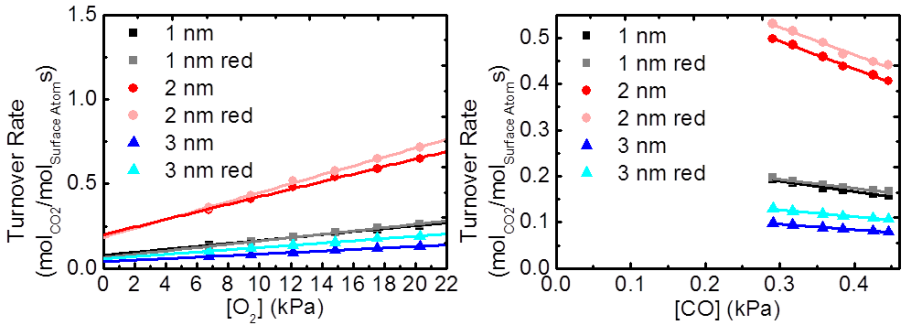

Figure 46: Partial pressure dependences for CO oxidation at 200°C for supported "surfactant-free" Pt NPs on TiO_2 with 1 nm, 2 nm, and 3 nm particle size with and without reductive pre-treatment. For O_2 partial pressure dependences the partial pressure of O_2 was varied between 6.8 and 20 kPa with a constant CO partial pressure of 0.39 kPa (a). For the CO partial pressure dependence the CO partial pressure was varied in a range of 0.29 to 0.45 kPa and a constant O_2 partial pressure of 12.2 kPa (b) at a reaction temperature of 200°C.

Compared to Pt-Fe_3O_4 for Pt-TiO_2 no significant changes of the catalytic activity after reduction with 5% H_2 for 16 h at 200°C was found and the kinetic parameters (200°C reaction temperature) for all particle sizes and independent of reductive pre-treatment are similar (see Table 16).

Table 16: Reaction orders for O_2 and CO determined from the partial pressure dependences and apparent activation energies obtained for Pt NPs on TiO_2 at 200°C with reductive pre-treatment (5% H_2 for 16 h at 200°C) and without reductive pre-treatment.

Particle size	Reaction order O_2	Reaction order CO	Apparent activation energy (KJ/mol)
1 nm	0.57 ± 0.05	-0.47 ± 0.05	84.4 ± 4.6
1 nm red	0.65 ± 0.05	-0.40 ± 0.05	86.9 ± 4.7
2 nm	0.58 ± 0.05	-0.48 ± 0.05	86.2 ± 3.2
2 nm red	0.63 ± 0.05	-0.44 ± 0.05	86.2 ± 4.5
3 nm	0.58 ± 0.05	-0.49 ± 0.05	83.1 ± 4.2
3 nm red	0.57 ± 0.05	-0.45 ± 0.05	81.2 ± 4.8

In order to further investigate the interesting behaviour of Pt-TiO_2 (1 – 3 nm particle size) detailed kinetic experiments are necessary in order to postulate reaction mechanism. Furthermore, the

kinetic performance of CO oxidation could be further tuned by using different bimetallic Pt NPs with different transition metals (Sn, Zn).

A catalyst for CO oxidation normally works at high reaction temperature, where the mobility of the NP increases and NP tend to accumulate. The decreases of the active surface leads to a decrease of the catalytic performance. Hence, an interesting question for industrial application is whether SMSI effects can be used in order to diminish sintering of NPs on the support. The systematic study of SMSI effects in this work can be used to investigate whether support materials can be found, which stabilized the NPs from sintering at high temperature. Investigations with IL-TEM before and after heat-treatment can be used to characterize the stability again sintering.

Another reaction, which is interesting for industrial applications, is the preferential oxidation of CO (CO PROX) for the removal of poisoning CO in H_2 streams for fuel cell applications.[194] The reaction requires a catalyst, which offers high selectivity and activity toward oxidation of CO. The reaction mechanism of supported Pt NPs might be influenced due to the reducing atmosphere during the reaction. The study of support effects and bimetallic NPs in CO PROX reactions can be used to optimize the selectivity and activity.

11. References

[1] B. Leach, *Applied industrial catalysis*, Elsevier, **2012**.
[2] F. Zaera, *The Chemical Record* **2005**, *5*, 133-144.
[3] J. Hagen, *Industrial catalysis: a practical approach*, John Wiley & Sons, **2015**.
[4] W. Ostwald, *Physikal. Z* **1902**, *3*, 313.
[5] S. T. Oyama, G. A. Somorjai, *J. Chem. Educ.* **1988**, *65*, 765.
[6] J. M. Thomas, *Angewandte Chemie International Edition in English* **1994**, *33*, 913-937.
[7] I. Lee, F. Delbecq, R. Morales, M. A. Albiter, F. Zaera, *Nature materials* **2009**, *8*, 132.
[8] V. Ponec, *Catalysis Reviews Science and Engineering* **1975**, *11*, 41-70.
[9] A. Ault, *J. Chem. Educ.* **2002**, *79*, 572.
[10] C. P. Casey, *J. Chem. Educ.* **2006**, *83*, 192.
[11] G. Ertl, *Angew. Chem.* **2008**, *120*, 3578-3590.
[12] D. Astruc, *Analytical and bioanalytical chemistry* **2011**, *399*, 1811-1814.
[13] A. Behr, P. Neubert, *Applied homogeneous catalysis*, John Wiley & Sons, **2012**.
[14] C. A. Tolman, *Chem. Rev.* **1977**, *77*, 313-348.
[15] D. J. Gorin, B. D. Sherry, F. D. Toste, *Chem. Rev.* **2008**, *108*, 3351-3378.
[16] B. Cornils, W. A. Herrmann, *J. Catal.* **2003**, *216*, 23-31.
[17] W. S. Knowles, *Adv. Synth. Catal.* **2003**, *345*, 3-13.
[18] A. Börner, *Eur. J. Inorg. Chem.* **2001**, *2001*, 327-337.
[19] M. Sawamura, Y. Ito, *Chem. Rev.* **1992**, *92*, 857-871.
[20] D. J. Cole-Hamilton, *Science* **2003**, *299*, 1702-1706.
[21] N. Mizuno, M. Misono, *Chem. Rev.* **1998**, *98*, 199-218.
[22] G. C. Bond, **1987**.
[23] J. J. Bravo-Suárez, R. V. Chaudhari, B. Subramaniam, in *Novel materials for catalysis and fuels processing*, ACS Publications, **2013**, pp. 3-68.
[24] D. F. Emerich, C. G. Thanos, *Expert opinion on biological therapy* **2003**, *3*, 655-663.
[25] C. M. Lieber, *MRS Bull.* **2011**, *36*, 1052-1063.
[26] R. Jin, *Nanotechnology Reviews* **2012**, *1*, 31-56.
[27] G. C. Bond, *Surf. Sci.* **1985**, *156*, 966-981.
[28] M. Boudart, *J. Mol. Catal.* **1985**, *30*, 27-38.
[29] R. J. White, R. Luque, V. L. Budarin, J. H. Clark, D. J. Macquarrie, *Chem. Soc. Rev.* **2009**, *38*, 481-494.
[30] R. Rioux, H. Song, J. Hoefelmeyer, P. Yang, G. Somorjai, *The Journal of Physical Chemistry B* **2005**, *109*, 2192-2202.
[31] Q.-L. Zhu, Q. Xu, *Chem* **2016**, *1*, 220-245.
[32] G. G. Wildgoose, C. E. Banks, R. G. Compton, *Small* **2006**, *2*, 182-193.
[33] K. An, G. A. Somorjai, *ChemCatChem* **2012**, *4*, 1512-1524.
[34] A. T. Bell, *Science* **2003**, *299*, 1688-1691.
[35] P. Saravanan, R. Gopalan, V. Chandrasekaran, *Defence Science Journal* **2008**, *58*, 504-516.
[36] J. Park, J. Joo, S. G. Kwon, Y. Jang, T. Hyeon, *Angew. Chem. Int. Ed.* **2007**, *46*, 4630-4660.
[37] H. Bönnemann, R. M. Richards, *Eur. J. Inorg. Chem.* **2001**, *2001*, 2455-2480.
[38] M. Niederberger, *Acc. Chem. Res.* **2007**, *40*, 793-800.
[39] H. Hayashi, Y. Hakuta, *Materials* **2010**, *3*, 3794-3817.
[40] N. Toshima, M. Kuriyama, Y. Yamada, H. Hirai, *Chem. Lett.* **1981**, *10*, 793-796.
[41] L. Mulfinger, S. D. Solomon, M. Bahadory, A. V. Jeyarajasingam, S. A. Rutkowsky, C. Boritz, *J. Chem. Educ.* **2007**, *84*, 322.
[42] Y. Qin, X. Ji, J. Jing, H. Liu, H. Wu, W. Yang, *Colloids and Surfaces A: Physicochemical and Engineering Aspects* **2010**, *372*, 172-176.
[43] J. Polte, *CrystEngComm* **2015**, *17*, 6809-6830.
[44] N. T. Thanh, N. Maclean, S. Mahiddine, *Chem. Rev.* **2014**, *114*, 7610-7630.
[45] V. K. LaMer, R. H. Dinegar, *J. Am. Chem. Soc.* **1950**, *72*, 4847-4854.

[46] J. Boita, L. Nicolao, M. C. Alves, J. Morais, *New J. Chem.* **2017**, *41*, 14478-14485.
[47] H. Reiss, *The Journal of Chemical Physics* **1951**, *19*, 482-487.
[48] P. W. Voorhees, *Journal of Statistical Physics* **1985**, *38*, 231-252.
[49] H. Zheng, R. K. Smith, Y.-w. Jun, C. Kisielowski, U. Dahmen, A. P. Alivisatos, *Science* **2009**, *324*, 1309-1312.
[50] X. Peng, L. Manna, W. Yang, J. Wickham, E. Scher, A. Kadavanich, A. P. Alivisatos, *Nature* **2000**, *404*, 59.
[51] B. v. Derjaguin, L. Landau, *Prog. Surf. Sci.* **1993**, *43*, 30-59.
[52] E. J. W. Verwey, J. T. G. Overbeek, K. Van Nes, *Theory of the stability of lyophobic colloids: the interaction of sol particles having an electric double layer*, Elsevier Publishing Company, **1948**.
[53] C. Amiens, D. de Caro, B. Chaudret, J. S. Bradley, R. Mazel, C. Roucau, *J. Am. Chem. Soc.* **1993**, *115*, 11638-11639.
[54] T. Teranishi, R. Kurita, M. Miyake, *J. Inorg. Organomet. Polym.* **2000**, *10*, 145-156.
[55] T. Teranishi, M. Hosoe, T. Tanaka, M. Miyake, *The Journal of Physical Chemistry B* **1999**, *103*, 3818-3827.
[56] S. G. Dixit, A. R. Mahadeshwar, S. K. Haram, *Colloids and Surfaces A: Physicochemical and Engineering Aspects* **1998**, *133*, 69-75.
[57] J. Chen, Y. Xiong, Y. Yin, Y. Xia, *Small* **2006**, *2*, 1340-1343.
[58] M. Zhao, R. M. Crooks, *Angew. Chem. Int. Ed.* **1999**, *38*, 364-366.
[59] M.-L. Wu, D.-H. Chen, T.-C. Huang, *Langmuir* **2001**, *17*, 3877-3883.
[60] M. Boudart, G. Djéga-Mariadassou, *Kinetics of heterogeneous catalytic reactions*, Princeton University Press, **2014**.
[61] M. Boudart, *Chem. Rev.* **1995**, *95*, 661-666.
[62] J. Muscat, D. Newns, *Prog. Surf. Sci.* **1978**, *9*, 1-43.
[63] F. Maillard, S. Schreier, M. Hanzlik, E. Savinova, S. Weinkauf, U. Stimming, *PCCP* **2005**, *7*, 385-393.
[64] S. Schauermann, J. Hoffmann, V. Johánek, J. Hartmann, J. Libuda, H. J. Freund, *Angew. Chem. Int. Ed.* **2002**, *41*, 2532-2535.
[65] J. Oudar, *Deactivation and poisoning of catalysts, Vol. 20*, CRC Press, **1985**.
[66] P. Strizhak, *Theor. Exp. Chem.* **2004**, *40*, 203-208.
[67] C. Perego, S. Peratello, *Catal. Today* **1999**, *52*, 133-145.
[68] J. A. Dumesic, G. W. Huber, M. Boudart, *Handbook of Heterogeneous Catalysis: Online* **2008**, 1445-1462.
[69] I. Chorkendorff, J. W. Niemantsverdriet, *Concepts of modern catalysis and kinetics*, John Wiley & Sons, **2017**.
[70] P. Mars, D. W. Van Krevelen, *Chem. Eng. Sci.* **1954**, *3*, 41-59.
[71] B. Hammer, J. K. Nørskov, in *Advances in catalysis, Vol. 45*, Elsevier, **2000**, pp. 71-129.
[72] M. Mavrikakis, B. Hammer, J. K. Nørskov, *Phys. Rev. Lett.* **1998**, *81*, 2819.
[73] J. R. Kitchin, J. K. Nørskov, M. A. Barteau, J. Chen, *Phys. Rev. Lett.* **2004**, *93*, 156801.
[74] G. C. Bond, *Platinum Met. Rev.* **1975**, *19*, 126-134.
[75] R. Van Hardeveld, F. Hartog, *Surf. Sci.* **1969**, *15*, 189-230.
[76] G. Wang, M. A. Van Hove, P. N. Ross, M. Baskes, *The Journal of chemical physics* **2005**, *122*, 024706.
[77] D. J. Wales, A. I. Kirkland, D. A. Jefferson, *The Journal of chemical physics* **1989**, *91*, 603-611.
[78] C. Schoenbaum, **2014**.
[79] J. Quinson, S. Neumann, T. Wannmacher, L. Kacenauskaite, M. Inaba, J. Bucher, F. Bizzotto, S. B. Simonsen, L. Theil Kuhn, D. Bujak, *Angew. Chem.* **2018**, *130*, 12518-12521.
[80] W. Spieker, J. Regalbuto, *Chem. Eng. Sci.* **2001**, *56*, 3491-3504.
[81] M. Palmer Jr, M. Vannice, *J. Chem. Technol. Biotechnol.* **1980**, *30*, 205-216.
[82] F. Pinna, *Catal. Today* **1998**, *41*, 129-137.
[83] E. Merlen, P. Beccat, J. Bertolini, P. Delichere, N. Zanier, B. Didillon, *J. Catal.* **1996**, *159*, 178-188.

[84] P. Sonström, M. Bäumer, *PCCP* **2011**, *13*, 19270-19284.
[85] C.-J. Jia, F. Schüth, *PCCP* **2011**, *13*, 2457-2487.
[86] N. N. Kariuki, X. Wang, J. R. Mawdsley, M. S. Ferrandon, S. G. Niyogi, J. T. Vaughey, D. J. Myers, *Chem. Mater.* **2010**, *22*, 4144-4152.
[87] A. Miyazaki, I. Balint, K.-i. Aika, Y. Nakano, *J. Catal.* **2001**, *204*, 364-371.
[88] Z. Kaidanovych, Y. Kalishyn, P. Strizhak, *Advances in Nanoparticles* **2013**, *2*, 32.
[89] P. S. Fernández, D. S. Ferreira, C. A. Martins, H. E. Troiani, G. A. Camara, M. E. Martins, *Electrochim. Acta* **2013**, *98*, 25-31.
[90] L. Altmann, S. Kunz, M. Bäumer, *The Journal of Physical Chemistry C* **2014**, *118*, 8925-8932.
[91] M. Chen, Y.-G. Feng, X. Wang, T.-C. Li, J.-Y. Zhang, D.-J. Qian, *Langmuir* **2007**, *23*, 5296-5304.
[92] K. M. Koczkur, S. Mourdikoudis, L. Polavarapu, S. E. Skrabalak, *Dalton Transactions* **2015**, *44*, 17883-17905.
[93] I. Schrader, J. Warneke, J. Backenköhler, S. Kunz, *J. Am. Chem. Soc.* **2015**, *137*, 905-912.
[94] I. Schrader, S. Neumann, R. Himstedt, A. Zana, J. Warneke, S. Kunz, *Chem. Commun.* **2015**, *51*, 16221-16224.
[95] I. Schrader, S. Neumann, A. Šulce, F. Schmidt, V. Azov, S. Kunz, *ACS Catalysis* **2017**, *7*, 3979-3987.
[96] G. A. Somorjai, F. Tao, J. Y. Park, *Top. Catal.* **2008**, *47*, 1-14.
[97] J. C. Meier, C. Galeano, I. Katsounaros, A. A. Topalov, A. Kostka, F. Schüth, K. J. Mayrhofer, *Acs Catalysis* **2012**, *2*, 832-843.
[98] L. D. Menard, F. Xu, R. G. Nuzzo, J. C. Yang, *J. Catal.* **2006**, *243*, 64-73.
[99] S. Kunz, E. Iglesia, *The Journal of Physical Chemistry C* **2014**, *118*, 7468-7479.
[100] Y. Wang, J. Ren, K. Deng, L. Gui, Y. Tang, *Chem. Mater.* **2000**, *12*, 1622-1627.
[101] I. Schrader, J. Warneke, S. Neumann, S. Grotheer, A. A. Swane, J. J. Kirkensgaard, M. Arenz, S. Kunz, *The Journal of Physical Chemistry C* **2015**, *119*, 17655-17661.
[102] Q. Chen, N. V. Richardson, *Prog. Surf. Sci.* **2003**, *73*, 59-77.
[103] B. Sexton, K. Rendulic, A. Huges, *Surf. Sci.* **1982**, *121*, 181-198.
[104] A. F. Lee, D. E. Gawthrope, N. J. Hart, K. Wilson, *Surf. Sci.* **2004**, *548*, 200-208.
[105] F. M. Hoffmann, *Surf. Sci. Rep.* **1983**, *3*, 107-192.
[106] S. Kunz, M. M. Maturi, I. Schrader, J. Backenköhler, M. Tschurl, U. Heiz, *J. Colloid Interface Sci.* **2014**, *426*, 264-269.
[107] S. Neumann, S. Grotheer, J. Tielke, I. Schrader, J. Quinson, A. Zana, M. Oezaslan, M. Arenz, S. Kunz, *Journal of Materials Chemistry A* **2017**, *5*, 6140-6145.
[108] J. Speder, L. Altmann, M. Roefzaad, M. Bäumer, J. J. Kirkensgaard, K. Mortensen, M. Arenz, *PCCP* **2013**, *15*, 3602-3608.
[109] J. Quinson, M. Inaba, S. Neumann, A. A. Swane, J. Bucher, S. B. Simonsen, L. Theil Kuhn, J. J. Kirkensgaard, K. M. Jensen, M. Oezaslan, *ACS Catalysis* **2018**, *8*, 6627-6635.
[110] H. Song, R. M. Rioux, J. D. Hoefelmeyer, R. Komor, K. Niesz, M. Grass, P. Yang, G. A. Somorjai, *J. Am. Chem. Soc.* **2006**, *128*, 3027-3037.
[111] N. Aoun, A. Schlange, A. R. dos Santos, U. Kunz, T. Turek, *Electrocatalysis* **2016**, *7*, 13-21.
[112] N. Steinfeldt, *Langmuir* **2012**, *28*, 13072-13079.
[113] A. Cao, R. Lu, G. Veser, *PCCP* **2010**, *12*, 13499-13510.
[114] S. R. Challa, A. T. Delariva, T. W. Hansen, S. Helveg, J. Sehested, P. L. Hansen, F. Garzon, A. K. Datye, *J. Am. Chem. Soc.* **2011**, *133*, 20672-20675.
[115] J. Bett, K. Kinoshita, P. Stonehart, *J. Catal.* **1974**, *35*, 307-316.
[116] P. Migowski, J. Dupont, *Chemistry–A European Journal* **2007**, *13*, 32-39.
[117] M. Hasani, A. Khodadadi, S. Koleini, A. Saeedi, A. Meléndez, in *Journal of Physics: Conference Series, Vol. 786*, IOP Publishing, **2017**, p. 012042.
[118] P. Ferreira, Y. Shao-Horn, D. Morgan, R. Makharia, S. Kocha, H. Gasteiger, *J. Electrochem. Soc.* **2005**, *152*, A2256-A2271.
[119] T. W. Hansen, A. T. DeLaRiva, S. R. Challa, A. K. Datye, *Acc. Chem. Res.* **2013**, *46*, 1720-1730.
[120] F. Hasché, M. Oezaslan, P. Strasser, *PCCP* **2010**, *12*, 15251-15258.

[121] A. Pavlišič, P. Jovanovič, V. Šelih, M. Šala, N. Hodnik, S. Hočevar, M. Gaberšček, *Chem. Commun.* **2014**, *50*, 3732-3734.
[122] A. Yadav, A. Nishikata, T. Tsuru, *Electrochim. Acta* **2007**, *52*, 7444-7452.
[123] C. Cullis, B. Willatt, *J. Catal.* **1984**, *86*, 187-200.
[124] D. O. Simone, T. Kennelly, R. J. Farrauto, *Applied catalysis* **1991**, *70*, 87-100.
[125] A. D. Allian, K. Takanabe, K. L. Fujdala, X. Hao, T. J. Truex, J. Cai, C. Buda, M. Neurock, E. Iglesia, *J. Am. Chem. Soc.* **2011**, *133*, 4498-4517.
[126] F. Bonet, V. Delmas, S. Grugeon, R. H. Urbina, P. Silvert, K. Tekaia-Elhsissen, *Nanostruct. Mater.* **1999**, *11*, 1277-1284.
[127] J. J. Whalen, J. D. Weiland, P. C. Searson, *J. Electrochem. Soc.* **2005**, *152*, C738-C743.
[128] J.-S. Chen, A. N. Vasiliev, A. P. Panarello, J. G. Khinast, *Applied Catalysis A: General* **2007**, *325*, 76-86.
[129] Z. Niu, Q. Peng, Z. Zhuang, W. He, Y. Li, *Chemistry–A European Journal* **2012**, *18*, 9813-9817.
[130] V. Klimavicius, S. Neumann, S. Kunz, T. Gutmann, G. Buntkowsky, *Catalysis Science & Technology* **2019**.
[131] A. Ernst, J. D. Zibrak, *New England journal of medicine* **1998**, *339*, 1603-1608.
[132] J. Greenberg, P. Zimmerman, L. Heidt, W. Pollock, *Journal of Geophysical Research: Atmospheres* **1984**, *89*, 1350-1354.
[133] E. Coleman, C. Thomas, *Journal of applied chemistry* **1954**, *4*, 379-383.
[134] Y. Mergler, A. Van Aalst, J. Van Delft, B. Nieuwenhuys, *J. Catal.* **1996**, *161*, 310-318.
[135] I. Langmuir, *Transactions of the Faraday Society* **1922**, *17*, 621-654.
[136] E. D. Park, D. Lee, H. C. Lee, *Catal. Today* **2009**, *139*, 280-290.
[137] J. Ayastuy, M. Gonzalez-Marcos, J. Gonzalez-Velasco, M. Gutiérrez-Ortiz, *Applied Catalysis B: Environmental* **2007**, *70*, 532-541.
[138] S. Alayoglu, A. U. Nilekar, M. Mavrikakis, B. Eichhorn, *Nature materials* **2008**, *7*, 333.
[139] H. Dhar, L. Christner, A. Kush, *J. Electrochem. Soc.* **1987**, *134*, 3021-3026.
[140] M. Rinnemo, D. Kulginov, S. Johansson, K. Wong, V. P. Zhdanov, B. Kasemo, *Surf. Sci.* **1997**, *376*, 297-309.
[141] M. Chen, Y. Cai, Z. Yan, K. Gath, S. Axnanda, D. W. Goodman, *Surf. Sci.* **2007**, *601*, 5326-5331.
[142] P. J. Berlowitz, C. H. Peden, D. W. Goodman, *The Journal of Physical Chemistry* **1988**, *92*, 5213-5221.
[143] M. García-Diéguez, E. Iglesia, *J. Catal.* **2013**, *301*, 198-209.
[144] G. Zafiris, R. Gorte, *J. Catal.* **1993**, *140*, 418-423.
[145] B. Atalik, D. Uner, *J. Catal.* **2006**, *241*, 268-275.
[146] H. Bonzel, R. Ku, *Surf. Sci.* **1972**, *33*, 91-106.
[147] T. Matsushima, *Surf. Sci.* **1979**, *79*, 63-75.
[148] C. Campbell, G. Ertl, H. Kuipers, J. Segner, *The Journal of Chemical Physics* **1980**, *73*, 5862-5873.
[149] G. Blyholder, *The Journal of Physical Chemistry* **1964**, *68*, 2772-2777.
[150] Y.-W. Huang, S.-L. Lee, *Chem. Phys. Lett.* **2010**, *492*, 98-102.
[151] B. Hammer, O. H. Nielsen, J. Nrskov, *Catal. Lett.* **1997**, *46*, 31-35.
[152] D. Collins, W. Spicer, *Surf. Sci.* **1977**, *69*, 85-113.
[153] A. Luntz, M. Williams, D. Bethune, *The Journal of chemical physics* **1988**, *89*, 4381-4395.
[154] P. Gambardella, Ž. Šljivančanin, B. Hammer, M. Blanc, K. Kuhnke, K. Kern, *Phys. Rev. Lett.* **2001**, *87*, 056103.
[155] T. Panczyk, *PCCP* **2006**, *8*, 3782-3795.
[156] R. Imbihl, G. Ertl, *Chem. Rev.* **1995**, *95*, 697-733.
[157] G. Ertl, P. Norton, J. Rüstig, *Phys. Rev. Lett.* **1982**, *49*, 177.
[158] J. Moulijn, A. Tarfaoui, F. Kapteijn, *Catal. Today* **1991**, *11*, 1-12.
[159] R. J. Madon, M. Boudart, *Industrial & Engineering Chemistry Fundamentals* **1982**, *21*, 438-447.

[160] A. Boubnov, S. Dahl, E. Johnson, A. P. Molina, S. B. Simonsen, F. M. Cano, S. Helveg, L. J. Lemus-Yegres, J.-D. Grunwaldt, *Applied Catalysis B: Environmental* **2012**, *126*, 315-325.
[161] J. Bitter, K. Seshan, J. Lercher, *J. Catal.* **1999**, *183*, 336-343.
[162] D. W. Flaherty, W.-Y. Yu, Z. D. Pozun, G. Henkelman, C. B. Mullins, *J. Catal.* **2011**, *282*, 278-288.
[163] J.-W. Snoeck, G. Froment, M. Fowles, *Industrial & engineering chemistry research* **2002**, *41*, 4252-4265.
[164] Y. Morikawa, J. J. Mortensen, B. Hammer, J. K. Nørskov, *Surf. Sci.* **1997**, *386*, 67-72.
[165] P. J. Berlowitz, C. H. Peden, D. W. Goodman, *J. Phys. Chem* **1988**, *92*, 5213-5221.
[166] S. Tauster, S. Fung, R. L. Garten, *J. Am. Chem. Soc.* **1978**, *100*, 170-175.
[167] S. Tauster, *Acc. Chem. Res.* **1987**, *20*, 389-394.
[168] O. Dulub, W. Hebenstreit, U. Diebold, *Phys. Rev. Lett.* **2000**, *84*, 3646.
[169] S. Bonanni, K. Aït-Mansour, H. Brune, W. Harbich, *Acs Catalysis* **2011**, *1*, 385-389.
[170] O. S. Alexeev, S. Y. Chin, M. H. Engelhard, L. Ortiz-Soto, M. D. Amiridis, *The Journal of Physical Chemistry B* **2005**, *109*, 23430-23443.
[171] Y.-N. Sun, Z.-H. Qin, M. Lewandowski, S. Kaya, S. Shaikhutdinov, H.-J. Freund, *Catal. Lett.* **2008**, *126*, 31-35.
[172] Y.-N. Sun, Z.-H. Qin, M. Lewandowski, E. Carrasco, M. Sterrer, S. Shaikhutdinov, H.-J. Freund, *J. Catal.* **2009**, *266*, 359-368.
[173] Z.-H. Qin, M. Lewandowski, Y.-N. Sun, S. Shaikhutdinov, H.-J. Freund, *The Journal of Physical Chemistry C* **2008**, *112*, 10209-10213.
[174] M. Abid, V. Paul-Boncour, R. Touroude, *Applied Catalysis A: General* **2006**, *297*, 48-59.
[175] F. B. Passos, D. A. Aranda, R. R. Soares, M. Schmal, *Catal. Today* **1998**, *43*, 3-9.
[176] L. Liu, F. Zhou, L. Wang, X. Qi, F. Shi, Y. Deng, *J. Catal.* **2010**, *274*, 1-10.
[177] L. Li, A. Wang, B. Qiao, J. Lin, Y. Huang, X. Wang, T. Zhang, *J. Catal.* **2013**, *299*, 90-100.
[178] L. Liu, B. Qiao, Y. He, F. Zhou, B. Yang, Y. Deng, *J. Catal.* **2012**, *294*, 29-36.
[179] M. Haruta, S. Tsubota, T. Kobayashi, H. Kageyama, M. J. Genet, B. Delmon, *J. Catal.* **1993**, *144*, 175-192.
[180] M. Lewandowski, Y.-N. Sun, Z.-H. Qin, S. Shaikhutdinov, H.-J. Freund, *Applied Catalysis A: General* **2011**, *391*, 407-410.
[181] M. Lewandowski, I. Groot, S. Shaikhutdinov, H.-J. Freund, *Catal. Today* **2012**, *181*, 52-55.
[182] R. Bliem, J. van der Hoeven, A. Zavodny, O. Gamba, J. Pavelec, P. E. de Jongh, M. Schmid, U. Diebold, G. S. Parkinson, *Angew. Chem. Int. Ed.* **2015**, *54*, 13999-14002.
[183] C. Lemire, R. Meyer, V. E. Henrich, S. Shaikhutdinov, H.-J. Freund, *Surf. Sci.* **2004**, *572*, 103-114.
[184] K. A. Halim, M. Khedr, M. Nasr, A. El-Mansy, *Mater. Res. Bull.* **2007**, *42*, 731-741.
[185] P. Li, D. E. Miser, S. Rabiei, R. T. Yadav, M. R. Hajaligol, *Applied Catalysis B: Environmental* **2003**, *43*, 151-162.
[186] M. Khedr, K. A. Halim, M. Nasr, A. El-Mansy, *Materials Science and Engineering: A* **2006**, *430*, 40-45.
[187] S. Wagloehner, D. Reichert, D. Leon-Sorzano, P. Balle, B. Geiger, S. Kureti, *J. Catal.* **2008**, *260*, 305-314.
[188] N. Li, Q.-Y. Chen, L.-F. Luo, W.-X. Huang, M.-F. Luo, G.-S. Hu, J.-Q. Lu, *Applied Catalysis B: Environmental* **2013**, *142*, 523-532.
[189] S. Neumann, T. Gutmann, G. Buntkowsky, S. Paul, G. Thiele, H. Sievers, M. Bäumer, S. Kunz, *J. Catal.* **2019**, *377*, 662-672.
[190] H.-H. Liu, Y. Wang, A.-P. Jia, S.-Y. Wang, M.-F. Luo, J.-Q. Lu, *Appl. Surf. Sci.* **2014**, *314*, 725-734.
[191] S. Sun, C. B. Murray, D. Weller, L. Folks, A. Moser, *science* **2000**, *287*, 1989-1992.
[192] T. Ma, Q. Fu, H. Y. Su, H. Y. Liu, Y. Cui, Z. Wang, R. T. Mu, W. X. Li, X. H. Bao, *ChemPhysChem* **2009**, *10*, 1013-1016.
[193] S. Zafeiratos, S. Piccinin, D. Teschner, *Catalysis Science & Technology* **2012**, *2*, 1787-1801.

[194] M. Kahlich, H. Gasteiger, R. Behm, *J. Catal.* **1997**, *171*, 93-105.

Declaration on the contribution to the multi-author publications which are included in the doctoral thesis

Publication I:

Contribution in % of the total work load (up to 100% for each of the following categories):

Experimental concept and design:	ca. 60%
Experimental work and/or acquisition of (experimental) data:	ca. 60%
Data analysis and interpretation:	ca. 70%
Preparation of Figures and Tables:	ca. 80%
Drafting of the manuscript:	ca. 70%

Publication II:

Contribution in % of the total work load (up to 100% for each of the following categories):

Experimental concept and design:	ca. 80%
Experimental work and/or acquisition of (experimental) data:	ca. 80%
Data analysis and interpretation:	ca. 70%
Preparation of Figures and Tables:	ca. 100%
Drafting of the manuscript:	ca. 80%

Publication III:

Contribution in % of the total work load (up to 100% for each of the following categories):

Experimental concept and design:	ca. 80%
Experimental work and/or acquisition of (experimental) data:	ca. 70%
Data analysis and interpretation:	ca. 70%
Preparation of Figures and Tables:	ca. 80%
Drafting of the manuscript:	ca. 80%

Date:

Signature:

Curriculum Vitae

Persönliche Daten

Name:	Sarah Neumann
Geburtsdatum:	26.10.1989 in Verden
Kontakt:	Weserstraße 3
	28832 Achim
	0173/8517373
	sarah.neumann@uni-bremen.de

Berufliche Laufbahn

02/2016 – 05/2019	Wissenschaftliche Mitarbeiterin Institut für Angewandte und Physikalische Chemie, Universität Bremen
04/2013 – 05/2016	Nachhilfelehrerin bei der Schülerhilfe
10/2012 – 10/2013	Studentische Hilfskraft: Betreuung des Allgemeinen Chemie Praktikums und Praktikum für Spurenanalytik

Akademische Laufbahn

02/2016 - laufend	Promotionsstudium Institut für Institut für Angewandte und Physikalische Chemie, AG Bäumer, Universität Bremen *„Catalysis with supported Nanoparticles: Size effects and Metal-Support Interactions“*
10/2013 – 10/2015	Masterstudium Masterarbeit am Institut für Institut für Angewandte und Physikalische Chemie, AG Bäumer, Universität Bremen *„Modifizierung von Prolin-Derivaten und deren Anwendung als Liganden zur Funktionalisierung katalytischer NPs“*
10/2010 – 10/2013	Bachelorstudium

	Bachelorarbeit am Centre for Biomolecular Interactions, AG Dringen, Universität Bremen *„Einfluss von Arsenat auf den Glucose-Stoffwechsel von Astrozyten“*
08/2002 – 04/2009	Cato-Bontjes van Beek-Gymnasium, Achim

Auslandserfahrungen

09/2009 – 03/2010	Akademisches Sprachsemester in Barcelona, Spanien
08/2007 – 09/2007	Sprachaufenthalt in Eastbourne, England

Teilnahme an wissenschaftlichen Veranstaltungen

03/2018	51. Jahrestreffen Deutscher Katalytiker, Weimar Auszeichnung mit Posterpreis
06/2018	Vortag, UFT Flashlights, Bremen
12/2018	Vortrag, Doktorandenkolloquium der GdCH, Bremen

Kenntnisse

Sprachen	Deutsch: Muttersprache Englisch: Erweiterte Kenntnisse Spanisch: Erweiterte Kenntnisse Latein: Großes Latinum Französisch: Grundkenntnisse
EDV	MS Office, Origin, ImageJ, Endnote
Weiteres	Umfassende Sachkunde nach §5 der Chemikalien-Verbotsverordnung Früherschein der Klasse B

Vollständige Publikationsliste

1. **Neumann, S.;** Doebler, H.H; Keil, S.; Erdt, A.; Borchert, H.; Kolny-Olesiak, J.; Parisi, J.; Bäumer, M.; Kunz, S., Effects of Particle Size on Strong Metal Support Interactions using colloidal „Surfactant-free“ Pt NP supported on Fe_3O_4, *submitted,* **2019**

2. **Neumann, S.**; Gutmann, T.; Buntkowsky, G.; Paul, S.; Thiele, G.; Sievers, H.; Bäumer, M.; Kunz, S., Insights into the Reaction Mechanism and Particle Size Effects of CO Oxidation over Supported Pt Nanoparticles Catalysts, *Journal of Catalysis,* **2019,** 377, 662-672

3. Klimavicius, V.; **Neumann, S**.; Kunz, S.; Gutmann, T.; Buntkowsky, G., Room temperature CO oxidation catalysed by supported Pt nanoparticles revealed by solid-state NMR and DNP spectroscopy. *Catal. Sci. Technol*., **2019**, 9, 3743-3752

4. **Neumann, S.**; Schröder, J.; Bizzotto, F.; Arenz, M.; Dworzak, A.; Özaslan, M.; Bäumer, M.; Kunz, S., Halide-Induced Leaching of Pt Nanoparticles – Manipulation of Particle Size by Controlled Ostwald Ripening, *ChemNanoMat*, **2019**, 5, 4, 462-471

5. Quinson, J.; Inaba, M**.; Neumann, S.**; Swane, A.A.; Bucher, J.; Simonsen, S.; Kuhn, L.T.; Kirkensgaard, J. J. K.; Jensen, K.M.; Özaslan, M.; Kunz, S.; Arenz, M., Investigating Particle Size Effects in Catalysis by Applying a Size- Controlled and Surfactant-Free Synthesis of Colloidal Nanoparticles in Alkaline Ethylene Glycol: Case Study of the Oxygen Reduction Reaction on Pt, *ACS Catalysis*, **2018**, 8, 7, 6627-6635.

6. Quinson, J.; **Neumann, S.**; Wannmacher, T.; Kacenauskaite, L.; Inaba, M.; Bucher, J.; Bizzotto, F.; Simonsen, S.; Kuhn, L.T.; Bujak, D.; Zana, A.; Arenz, M.; Kunz, S., Colloids for Catalysts: A Concept for the Preparation of Superior Catalysts of Industrial Relevance, *Angewandte Chemie*, **2018**, 130, 12518-12521.

7. **Neumann, S.**; Grotheer, S.; Tielke, J.; Schrader, I.; Quinson, J.; Zana, A.; Oezaslan, M.; Arenz, M.; Kunz, S., Nanoparticles in a Box: A Concept to Isolate, Store and Re-Use Colloidal Surfactant-Free Precious Metal Nanoparticles, *Journal of Materials Chemistry A*, **2017**, 5, 6140-6145.

8. Schrader, I.; **Neumann, S.**; Sulce, A; Schmidt, F.; Azov, V.; Kunz, S., Asymmetric Heterogeneous Catalysis –Transfer of Molecular Principles to Nanoparticles by Ligand Functionalization, *ACS Catalysis*, **2017**, 7, 3979-3987.

9. Schubert, M.; Wilhelm, M.; Bragulla, S.; Sun, C.; **Neumann, S.**; Gesing, T.M.; Pfeifer, P.; Rezwan, K.; Bäumer, M., The Influence of the Pyrolysis Temperature on the Material Properties of Cobalt and Nickel Containing Precursor Derived Ceramics and their Catalytic Use for CO_2 Methanation and Fischer-Tropsch Synthesis, *Catalysis Letters*, **2017**, 147, 472-482.

10. Dringen, R.; Spiller, S.; **Neumann, S.**; Koehler, Y., Uptake, Metabolic Effects and Toxicity of Arsenate and Arsenite in Astrocytes, *Neurochemical Research*, **2016**, 41, 465-475.

11. Schrader, I.; **Neumann, S.**; Himstedt, S.; Zana, A.; Warneke, J.; Kunz, S., The Effect of Particle Size and Ligand Configuration on the Asymmetric Catalytic Properties of Proline-functionalized Pt-Nanoparticles, *Chemical Communications*, **2015**, 51, 16221-16224.

12. Schrader, I.; Warneke, J.; **Neumann, S.**; Grotheer, S.; Swane, A. A.; Kirkensgaard, J. J. K.; Arenz, M.; Kunz, S., The Surface Chemistry of "Unprotected" Nanoparticles –A Spectroscopic Investigation on Colloidal Particles, *Journal of Physical Chemistry C*, **2015**, 19, 17655-17661.

Publications

Paper I:

Halide-Induced Leaching of Pt Nanoparticles – Manipulation of Particle Size by Controlled Ostwald Ripening

S. Neumann, J. Schröder, F. Bizzotto, M. Arenz, A. Dworzak, M. Oezaslan, M. Bäumer, S. Kunz

ChemNanoMat, **2019**, 5, 4, 462-471

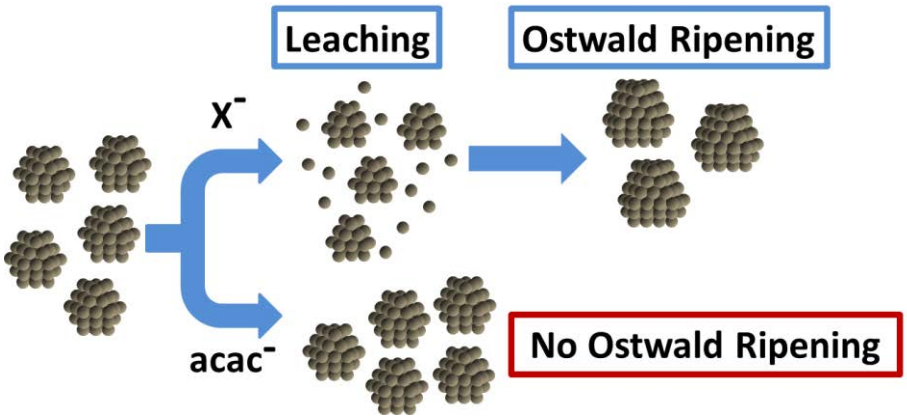

Paper II:

Insights into the reaction mechanism and particle size effects of CO oxidation over supported Pt nanoparticle catalysts

S. Neumann, T. Gutmann, G. Buntkowsky, S. Paul, G. Thiele, H. Sievers, M. Bäumer, S. Kunz

Journal of Catalysis, **2019**, 377, 662-672

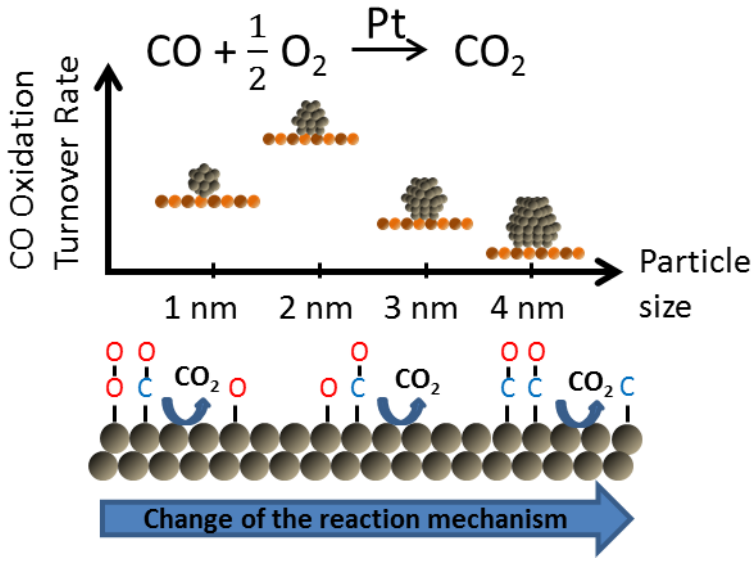

Paper III:

Effects of Particle Size on Strong Metal-Support Interactions using colloidal "Surfactant-free" Pt NP supported on Fe_3O_4

S. Neumann, H-H. Doebler, S. Keil, A.J. Erdt, C. Gutsche, H. Borchert, J. Kolny-Olesiak, J. Parisi, M. Bäumer, S. Kunz

Submitted